Carbon-Based Magnetic Nanomaterials

Valeria Zagaynova

Abstract

Magnetism of carbon-based materials is a challenging area for both fundamental research and possible applications.

We present studies of low-dimensional carbon-based magnetic systems (fullerene-diluted molecular magnets, carbon nanotubes, graphite fluoride, and nanoporous carbon) by means of SQUID magnetometer, X-ray diffraction and vibrational spectroscopy, the latter techniques used as complementary instruments to find a correlation between the magnetic behaviour and the structure of the samples.

In the first part of the thesis, characteristic features of the magnetization process in aligned films of carbon nanotubes with low concentration of iron are discussed. It is shown that the magnetism of such structures is influenced by quantum effects, and the anisotropy behaviour is opposite to what is observed in heavily doped nanotubes.

In the second part, Mn_{12}-based single molecular magnets with various carboxylic ligands and their 1:1 fullerene-diluted complexes are studied. We prove that magnetic properties of such systems strongly depend on the environment, and, in principle, it is possible to design a magnet with desirable properties. One of the studied compounds demonstrated a record blocking temperature for a single molecular magnet. Both fullerene-diluted complexes demonstrated "magnetization training" effect in alternating magnetic fields and the ability to preserve magnetic moment.

The third and the fourth parts of the thesis are dedicated to the analysis of various contributions to the magnetic susceptibility of metal-free carbon-based systems – intercalated compounds of graphite fluorides and nanoporous oxygen-eroded graphite. The magnetic properties of these systems are strongly dependent on structure, and can be delicately tuned by altering the π-electron system of graphite, i. e. by degree of fluorination of intercalated compounds and by introduction of boron impurity to the host matrix of nanoporous graphite.

Sammanfattning

Magnetism av kolbaserade material är ett utmanande område för både grundforskning och möjliga tillämpningar.

Vi presenterar studier med låg-dimensionella kolbaserade magnetiska system (fulleren-utspädda molekylära magneter, kolnanorör, grafit fluorid och nanoporösa kol) med hjälp av SQUID magnetometer, röntgendiffraktion och vibrerande spektroskopi, de senare tekniker som används som komplement instrument för att finna sambandet mellan den magnetiska uppträdande och strukturen hos proven.

I den första delen av avhandlingen är egenheter från magnetisering processen i linje filmer av kolnanorör med låg koncentration av järn diskuteras. Det visas att magnetism av sådana strukturer påverkas av kvantmekaniska effekter och anisotropin beteende är motsatsen till vad som observerats i kraftigt dopade nanorör.

I den tvåa delen är Mn_{12}-baserade enda-molekyl magneter med olika karboxylsyror ligander och deras 1:1 fulleren-utspädda komplex studeras. Vi visar att magnetiska egenskaperna hos sådana system beror i hög grad på miljön, och i princip är det möjligt att utforma en magnet med önskvärda egenskaper. En av de studerade föreningarna visade en post blockeringstemperaturen för en enda molekylär magnet. Både fulleren-utspädda komplex visade "magnetisering utbildning" effekt i alternerande magnetfält och möjligheten att bevara magnetiskt moment.

Den tredje och fjärde delarna av avhandlingen är avsedda för inneboende magnetism av analys av olika bidrag till magnetisk susceptibilitet av metall-fritt kol-baserade system - inskjutna föreningar grafit fluorider och nanoporösa O_2-eroderade grafit. Magnetiska egenskaperna hos dessa system är starkt beroende av strukturen, och kan fint avstämmas genom att man ändrar π-elektronsystem av grafit, i. e. med graden av fluorering av inskjutna föreningar och genom införandet av bor föroreningar till värd matris av nanoporösa grafit.

Included papers

This thesis is based on the following publications, which are attached at the end of this thesis:

I. **"Magnetic properties of carbon nanotubes with low content of Fe"**
V. S. Zagainova, T. L. Makarova, A.V. Okotrub, A.G. Kurenya, S. V. Komogortsev, and L.G. Bulusheva
Fullerenes, Nanotubes, and Carbon Nanostructures, 18: 569-573 (2010).

II. **"Synthesis and magnetic properties of Mn$_{12}$-based single molecular magnets with benzene and pentafluorobenzene carboxylate ligands"**
V. S. Zagainova, T. L. Makarova, N. G. Spitsina, and D. W. Boukhvalov
Journal of Superconductivity and Novel Magnetism, 24: 855-859 (2011).

III. **"Preparation and magnetic properties of Mn$_{12}$ clusters with 4-cyanobenzenecarboxylate ligand, [Mn$_{12}$O$_{12}$(O$_2$CC$_6$H$_4$-p-CN)$_{16}$(H$_2$O)$_4$] and its tetraphenylphosphonium salts"**
V. A. Sasnovskaya, L. A. Kushch, E. B. Yagubskii, I. V. Sulimenkov, V. I. Kozlovskiy, V. S. Zagaynova, and T. L. Makarova
Journal of Magnetism and Magnetic Materials, (2012), in press.

IV. **"Fullerene-induced magnetization training effect in single molecular magnet"**
T. L. Makarova, V. S. Zagaynova, and N. G. Spitsina
Physica Status Solidi B, 247: 3018-3021 (2010).

V. **"The magnetic memory effect in fullerene-containing single molecular magnets"**
V. S. Zagainova, T. L. Makarova, and N. G. Spitsina
Bulletin of the Russian Academy of Sciences: Physics, 74: 1426-1428 (2010).

VI. **"Structural Evolution and Magnetic Properties of Underfluorinated C$_2$F"**
T. L. Makarova, V. S. Zagaynova, G. Inan, A. V. Okotrub, G. N. Chekhova, D. V. Pinakov, and L. G. Bulusheva
Journal of Superconductivity and Novel Magnetism, 25: 79-83 (2012).

VII. **"The influence of boron doping on magnetic properties of oxygen-eroded graphite"**

V. S. Zagaynova, T. L. Makarova, L. Bergstrom, P. Vasiliev, F. M. Araújo-Moreira, H. Pardo, R. Faccio, and A. W. Mombrú

Submitted

Contents

List of abbreviations

AFM	–	atomic force microscopy
CNT	–	carbon nanotube
CVD	–	chemical vapour deposition
CW	–	Curie-Weiss (paramagnetism)
D	–	dimensional
DC	–	direct current
FC	–	field-cooled
FWHM	–	full width at half-maximum
HOPG	–	highly oriented pyrolitic graphite
ICGF	–	intercalation compounds of graphite fluorides
IR	–	infra-red
MFM	–	magnetic force microscopy
MPMS	–	magnetic property measurement system
NPC	–	nanoporous carbon
PIXE	–	particle induced X-ray emission
PMS	–	periodic minimal surface
RBM	–	radial breathing mode
SEM	–	scanning electron microscopy
SMM	–	single-molecule magnet
SQUID	–	superconducting quantum interference device
TEM	–	tunnelling electron microscopy
T_B	–	blocking temperature
XRD	–	X-ray diffraction
ZFC	–	zero-field-cooled

x

1. Introduction

The well-known Moore's law tells us that the density of electronic components (transistors) per integrated circuit increases exponentially in time. Studies on mobility of charge carriers in silicon brought worrying results: at a length scale below 10 nm the mobility degrades substantially, and it means that the age of silicon electronics is nearing its end. The most promising candidate to replace silicon is carbon, which has been proved to have many outstanding properties. The first transistors based on carbon nanotubes have already been developed [1-3], and there are predictions that carbon will be as important material for the 21st century, as silicon was in the 20th.

The term "nanomaterials" describes structures with typical size of 1 – 100 nm. Such materials often exhibit unique properties, among other, in magnetism, and, being single-domain particles, combine superparamagnetic behaviour with a variety of quantum effects.

Nanomaterials can be classified into several classes depending on dimensionality. Functionalization with carbon can influence the magnetic properties of nanomaterials in a number of ways, from nanotubes, which prevent encapsulated metallic nanoparticles from wear and oxidation, to fullerenes being the lever to control complex magnetic systems. Besides, there has been much speculation recently on carbon's intrinsic magnetism triggered by topological defects or modification of the lattice. Magnetism of pure carbon is an exciting research area, which can result in a breakthrough in spintronics and give unique biocompatible materials for biology and medicine. The advantage of carbon nanomaterials over classical semiconductors and metals comes from the combination of large electron velocity with long spin life time due to the small spin-orbit coupling of carbon.

Carbon-templated magnetic materials have been intensively investigated during the last decade, although there are still some "white spots" in experimental studies as well as in theory.

There's a great number of nanoscale carbon allotropes with exceptional properties.

This thesis is based on studies of magnetic properties of zero-dimensional (Mn-based magnets diluted with fullerenes), one-dimensional (films of vertically aligned Fe-filled carbon nanotubes), quasi-two-dimensional (fluorinated graphite), and three-dimensional (nanoporous carbon) magnetic carbon-based systems.

Carbon nanotubes (CNTs) have attracted great attention because of their extraordinary electrical, chemical, thermal, and mechanical properties. The filling of CNTs with different

metals is a well-known process, which protects the metal from the environment and safely separates wires from each other, providing more future applications: in medicine, as magnetic reinforced composites, spintronics and magnetic data storage devices [4-7].

A single-molecule magnet is another interesting object of nanoscale magnetism. Single molecule magnets (SMMs) – identical, bistable, combining magnetism with interesting optical and electrical properties (e. g. photosensitivity) – are, in fact, natural qubits. There is a huge library of ligand modifications, and it was demonstrated that magnetic properties of SMMs are strongly dependent on the magnetic core environment that makes it possible to produce magnets with desirable properties. SMMs are credited for molecular spin transistors, spin-valves, break-junction devices (a 3-terminal SMM device), and molecular multidot devices [8-11]. For this, to raise the blocking (working) temperature of SMMs is a serious challenge that needs to be solved. Addition of fullerenes to SMMs is predicted to result in orientation-controlled magnetism, similar to fullerene salts' magnetic behavior [12-13], since there is a strong correlation between the relative orientation of neighboring C_{60} molecules and intermolecular magnetic exchange interactions.

Fluorinated carbon materials are a no less attractive object from the magnetic point of view. Their properties can be altered both by the degree of fluorination and by synthesis conditions. Semi-fluorinated graphite is a system that contains arrays of fluorinated carbon atoms along with graphitic islands, and therefore, is a link between carbon-based magnetism and magnetically ordered molecule-based materials.

Nanoporous carbon (NPC) is a bulk, easy-to-produce all-carbon magnetic material with tunable porosity. Due to its highly defective structure, it can become a room-temperature ferromagnet [14], which would have great potential in medicine and biology as biocompatible magnetic material.

2

2. Materials

2.1. Iron-filled Carbon Nanotubes

Carbon nanotubes (CNTs) can be considered as rolled graphene sheets with lengths of several μm, whose ends are closed with fullerene-like caps. Their unique mechanical and electrical properties make them a promising object for applications in spintronics, medicine, composite materials and data storage devices. CNTs are chemically stable and can be filled with different materials such as metals, semiconductors, or organic materials either during synthesis or after, through the opening of nanotubes.

A special consideration are CNTs filled with ferromagnetic metals (Fe, Co, Ni). Carbon shell protects metallic nanowires from oxidation and safely separates them from each other. Nanotubes with different structural parameters, such as diameter, wall width, packaging of graphene layers, etc, differ much in physical properties. Magnetic properties of metal-filled CNTs are dependent on tubes characteristics, as well as the distribution of metal, the ratio between the tube and inner metallic nanowire diameters, and the filling rate.

2.1.1. Synthesis of carbon nanotubes

Among general methods of CNTs synthesis are laser ablation [15], arc discharge [16], plasma evaporation [17] and chemical vapor deposition (CVD) [18-19]. Varying of growth parameters allows one to obtain single-walled, multi-walled (which are, basically, several single-walled CNTs with different diameters inserted into each other) or filled nanotubes, aligned or disordered.
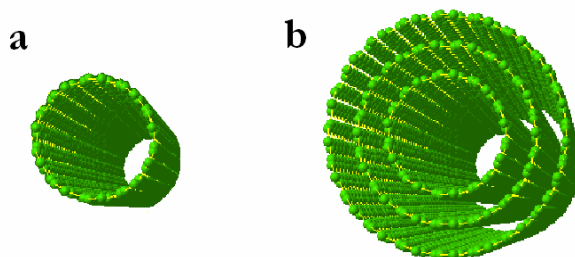

Fig. 1. Single-walled (a) and multi-walled (b) CNTs [20].

The CVD is a convenient method for the synthesis of arrays of aligned CNTs. Empty and filled carbon nanotubes are synthesized in similar ways. In both processes hydrocarbon precursor compounds are used to deliver the carbon for the formation of the CNT walls. In

addition, since it is a catalytic process, a catalyst (commonly ferrocene, cobaltocene or nickelocene Me-$(C_5H_5)_2$ particles) is involved to control the kinetics of reactions such as the decomposition of the precursor. The catalyst can be placed on a substrate or delivered via the gas phase. While for empty CNTs an additional source of hydrocarbon is often used, CNTs with high filling rates are synthesized from metal-organic compounds only.

The morphology and the structure of nanotubes depend on the growth parameters (especially, the temperature), catalysts, precursors, and the substrate. The interior of CNTs can contain trapped metallic catalyst particles and therefore, these CNTs can be considered as filled with an extremely low content of metal.

2.1.2. Magnetic properties of filled carbon nanotubes

The most investigated metal-filled CNTs are those filled with iron, though mainly heavily doped structures have been studied so far. In principle, iron inside nanotubes can be in three phases: paramagnetic γ-iron (which, to increase magnetic moment, normally is transformed to an α-iron+Fe_3C combination by annealing), ferromagnetic α-iron and ferromagnetic metastable iron carbide Fe_3C.
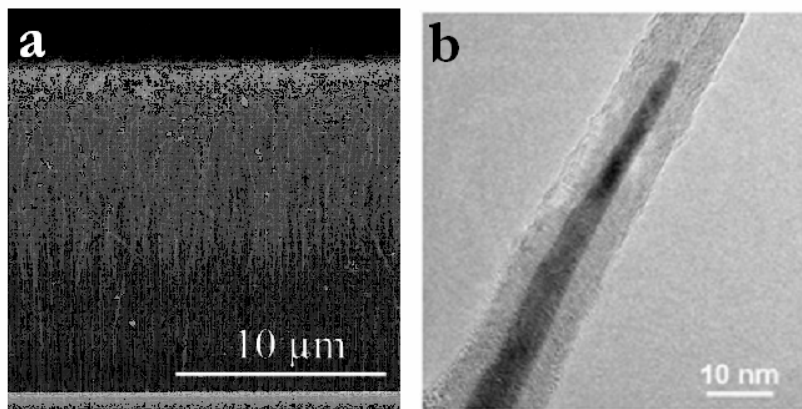
Fig. 2. A scanning electrom microscopy (SEM) image of iron-filled CNTs (a); a tunneling electrom microscopy (TEM) image of a partially filled CNT (b). Modified from [21].

In order to obtain information about the structure, X-ray diffraction or Mössbauer spectroscopy methods can be used. Also, the dominant phase can be recognized by the Curie temperature estimate from dc magnetic measurements. For example, the Curie point for α-iron is 1043 K, and for Fe_3C is ~493 K. XRD and Mössbauer spectroscopy together with SEM and TEM imaging are the typical methods for the structural characterization of filled carbon nanotubes.

The bulk magnetization measurements of Fe-filled CNTs reveal anisotropic behavior due to strong shape anisotropy with easy axis parallel to CNT walls (**Fig. 3**). However, CNT filled with Fe_3C demonstrate an easy axis of magnetization perpendicular to the CNT axis that can be explained in terms of strong magnetocrystalline anisotropy.
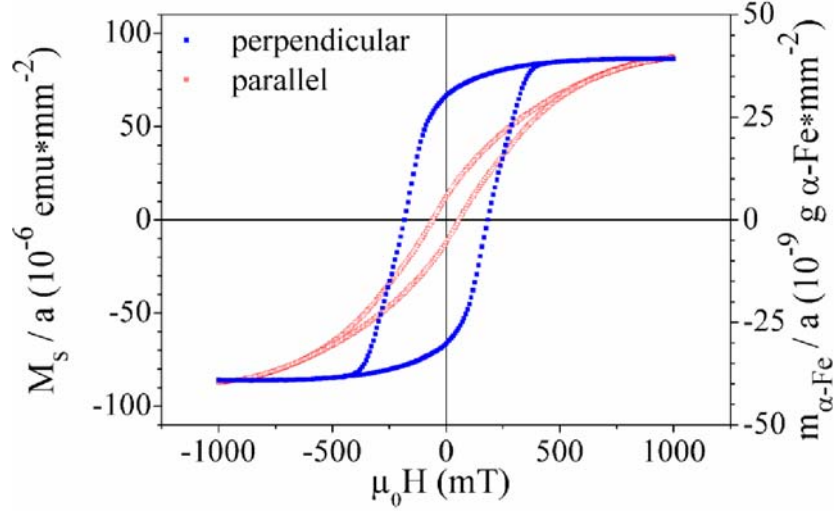

Fig. 3. A typical hysteresis loop for iron-filled CNTs with a filling rate ~45 wt.% [22].

The bulk saturation magnetization M_s and saturation moment m_s allow one to estimate the total volume V or mass M of the ferromagnetic material involved [22]: $V = m_s/M_s$.

The maximum energy of macroscopic magnetic anisotropy in a system of aligned nanotubes filled with α-iron can be estimated as πM_s^2, but the nonideality of alignment and CNT structure leads to a strong decrease. The studies of magnetization curves at saturation approach have shown that $\Delta M/M_s \sim H^{-3/2}$ [23]. Magnetization values of the CNTs containing Fe nanowires are reported to be close to the material's bulk magnetization [24-26]. Although magnetostatic parameters decrease at higher temperatures, the blocking temperature of ferromagnetic nanoparticles inside CNTs can be high enough to observe magnetism at room temperature [27].

CNTs not only serve as a protection coating for the metal, but can also act as part of the magnetic system. It has been shown that magnetic properties of transition metal nanowires encapsulated in single-walled CNTs are strongly influenced by the electronic properties of the nanotubes [28].

Individual metal-filled CNTs are studied by magnetic force microscopy [29] and electron holography [30]. These methods are used to measure stray field gradients and magnetic fluxes generated by filled CNTs, as well as their magnetic moments and anisotropy fields.

2.2. Mn$_{12}$-based Single Molecular Magnets

A single-molecule magnet (SMM) is a magnet on the nanoscale: a bulk permanent magnet contains 10^{20} individual spins, while a SMM has around 100. Usually it is an organic molecule with a metal core which contains one or several metal ions with unpaired spins (Mn, Co, Ni, Fe), surrounded by ligands. SMM crystals can be considered as complexes of single-domain almost independent units (as SMM crystal bonds are van der Waals). The stability of Mn$_{12}$-based crystals was studied in [31]. It was shown that they easily lose integrity under radiation and in humid atmosphere. Possible future applications of SMMs include new types of magnetic memory, wireless communications, biological applications, quantum computers. As it was discussed in [32], SMMs are of interest for molecular spintronics.

SMMs have several serious advantages over other magnetic nanoparticles: they are identical, and their structure and magnetic properties can be designed, moreover, magnetism in SMMs can be combined with interesting optical and electrical properties (e.g. photosensitive magnets).

The most important property of SMMs is magnetic bistability: it is possible for a spin to be switched between two antiparallel states that are provided by splitting the ground state of the molecule spin and inducing a double-well potential. In the simplest case, in a molecule with orbital-nondegenerate ground spin states the splitting is described by a square law DM_s^2, where D is an axial magnetic anisotropy parameter and M_s is the projected molecule spin, i.e. SMM has two quantum states $\pm S$. When the temperatures are low, the switching between $M_s = \pm S$ in zero magnetic field is due to thermally activated quantum tunneling transitions. The rate of quantum transitions grows with temperature making the magnetization relax quickly, and when the temperature reaches blocking, magnetization cannot be preserved efficiently anymore. At room temperature SMM behaves as a paramagnet.

For applications, the blocking temperature (T$_B$) of SMMs, which typically is around 3 K, should be significantly increased. It can be realized by increasing either the molecular spin S (by varying ions, enlargement of molecule size, etc.) or the magnetic anisotropy parameter D. The former way has serious restrictions. With an increase in spin, the magnetic dipole-dipole interaction between molecules also increases, which results in magnetic ordering of the SMM crystal, and a single molecule ceases to be magnetically independent. It is much more difficult to increase the parameter D. Quantitatively, further

studies of this parameter are still required. Furthermore, it was shown that high spin and high magnetic anisotropy cannot coexist [33].

Quantum tunneling (and relaxation of magnetization) increases greatly for excited spin levels: for example, for Mn_{12}-acetate relaxation at the first excited level $M_s = \pm S$ is $\sim 10^8$ times faster than at the ground spin level. It means that it is not only important to have a high energy barrier, but also the energy gap between the ground and the first excited states should be as large as possible. What makes the problem more difficult, there are no correlations between energy barrier parameters, ground spin state and cluster size.

For molecules with orbital-degenerate ground spin states, spin is no longer a good quantum number, and exchanges are anisotropic. There, the spin spectrum is far different from a square law, and the potential energy barrier can be much greater. Promising candidates for a new generation of SMMs are rare-earth 4f ions (lanthanides, for example, [34-35]) and orbital-degenerate 3d (Co^{2+}, $[Fe^{III}(CN)_6]^{3-}$), 4d and 5d ($[Re^{IV}(CN)_7]^{3-}$, $[Os^{III}(CN)_6]^{3-}$) ions and complexes. There's been much effort recently to synthesize mixed transition metal and lanthanide SMMs [36-37].

2.2.1. Mn-based single molecular magnet family

The first SMM of formula $[Mn_{12}O_{12}(CH_3COO)_{16}(H_2O)_4]\cdot 2CH_3COOH\cdot 4H_2O$ (Mn_{12}-acetate) was discovered in 1980 [38], although its unusual magnetic properties were discovered ten years later. Since that time, the family of Mn-based molecular magnets has been enlarged with a great number of derivatives; much effort has been made to increase 1) the cluster size, 2) the spin value in the ground state, and 3) the blocking temperature. While the first two goals have been achieved, the highest T_B remains to be around ~ 4.5 K for Mn_6 complex [39], although in [40] $T_B = \sim 9.6$ K was observed for specially treated Mn_{12}-acetate.

Many Mn-based SMMs have higher spin multiplicity of the ground state than S=10 of initial Mn_{12} sample. For instance, S=12 was observed for a Mn_{10} complex with the general formula $[Mn_{10}O_4(biphen)_4Br_{12}]^{4-}$ in [41]. Mn_{25}-based SMM shows a ground-state spin of 51/2 [42]. The highest reported spin was observed in Mn_{19} complex [43] S=83/2, but the blocking temperature of that complex was very low. The largest Mn-based SMM so far is a Mn_{84} cluster [44], which is 4.2 nm in diameter and is half-way between a quantum and a classical world object. Surely, for practical purposes the spin of SMM should be increased, but studies of molecular magnets with low ground spin states can also provide interesting

results: the Mn_4 cluster investigated in [45] shows an anisotropy energy barrier of 11.8 K despite the ground spin state S=9/2.
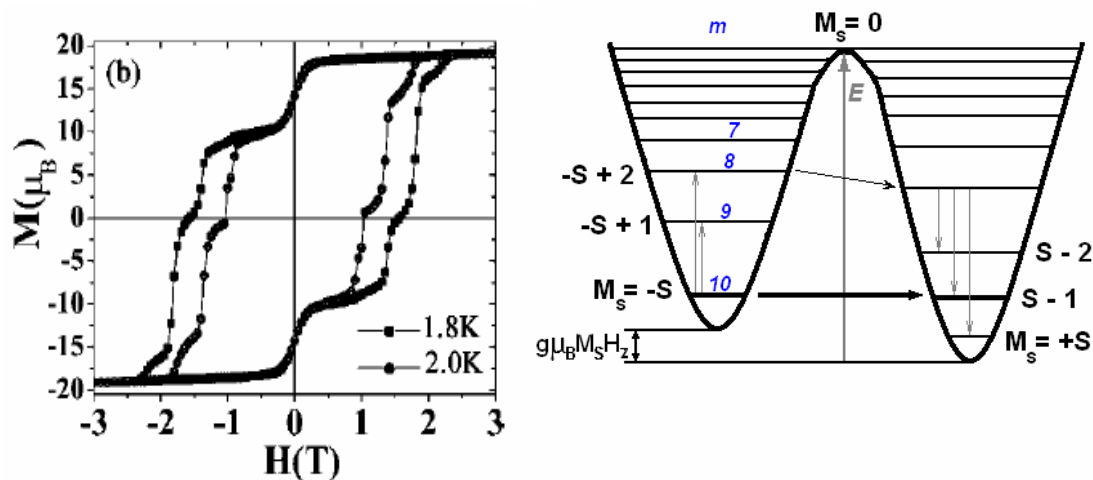

Fig. 4. Hysteresis loops for oriented $Mn_{12}Piv_{16}$ microcrystals [46] (left). Splitting of the ground spin state S and moving of spin levels under magnetic field (right).

At temperatures below T_B in zero magnetic field ground spin states are most populated. The switching between $M_s = +S$ and $M_s = -S$ is provided mainly by thermally activated quantum tunneling. When the field is increased, states $\pm S$ move against each other and the rate of quantum tunneling decreases until levels match again. On hysteresis curve this process is reflected as magnetization growth in noticeable steps.

Fig. 4 presents the typical field dependence for Mn-based SMMs, though the evidence of behavioral features of SMMs hysteresis curves happens to be dependent on the number of Mn atoms, i. e. on the size of SMM complex. The hysteresis curves of large molecules, for example, Mn_{25} [42], Mn_{30} [47], or Mn_{84} [44] show no clear steps coming from resonant quantum transitions that are typical for hysteresis curves of smaller molecules, such as Mn_4 [48] or Mn_{12} [46]. The step broadening in large SMM complexes can be due to massive disordered ligands, or larger amounts of crystallization solvent in larger voids between molecules, or low-lying excited states, usual for high nuclearity complexes.

2.2.2. Mn_{12}-based single molecular magnets

Mn_{12}-based molecular magnets have been intensively investigated during the last decade and remain to be the best known family of SMMs. They have a chemical formula $[Mn_{12}O_{12}-(O_2CR)_{16}(H_2O)_4]\cdot nSolv$, where R = CH_3, CH_5, etc, and *Solv* is crystallized solvent. There is a huge library of ligand modifications, and it was demonstrated that the magnetic

properties of SMMs are strongly dependent on the type of ligands that makes it possible to produce magnets with tailor-made properties. The synthesis of Mn_{12} acetate is rather simple. The molecule is soluble and perfectly stable in organic solvents such as DMF and acetonitrile. Another attractive feature is the huge uniaxial magnetic anisotropy. In the first approximation, it can be calculated through the spin Hamiltonian $H = DM_s^2$, where D/k_B is ~ -0.7 K, and $M_s = \pm 10$ that results in an energy barrier ~70 K. All this makes the Mn_{12}-based magnet a good model for studying SMM quantum effects.

A table of investigated Mn_{12} derivatives taken from [49] is presented below.

Table 1. Mn12 derivatives with reported structures [49].

Compound	R	x	Space group	Solvent molecules	H_2O coordination
1	Me	4	$I\bar{4}$	2 CH_3COOH, 4 H_2O	1:1:1:1
2	Et	3	$P1m$	4 H_2O	
3	Et	3	$P2_1/c$		
4	Me, Et	4	$I4m$	2 H_2O, 4 C_2H_5COOH	1:1:1:1
5	tBuCH$_2$	4	$P1m$	CH_2Cl_2, CH_3NO_2	1:2:1:0
6	Ph	4	$P1m$		2:2:0:0
7	Ph	4	$Fdd2$	2 C_6H_5COOH	2:2:0:0
8	p-Me-C$_6$H$_4$	4	$C2/c$	p-Me-C$_6$H$_4$COOH	1:2:1:0
9	p-Me-C$_6$H$_4$	4	$I2/a$	3 H_2O	1:1:2:0
10	p-Cl-C$_6$H$_4$	4	$C2/c$	8 CH_2Cl_2	2:2:0:0
11	m-Cl-C$_6$H$_4$	3	$P1m$	m-Cl-C$_6$H$_4$COOH	?
12	o-Cl-C$_6$H$_4$	4	$Pnn2$	CH_2Cl_2, 5 H_2O	1:1:2:0
13	PhCH$_2$	4	$P1m$		1:2:1:0

The Mn_{12} molecule core contains four central Mn^{4+} ions with S = 3/2 and eight peripheral Mn^{3+} ions with S = 2, connected with oxygen bridges (see **Fig. 5**). The core stays almost undisturbed when varying the ligands; the distances and angles between ions change insignificantly, but the electronic structure of the molecule depends strongly on ligands, defining its magnetic properties.

It was discovered that the ground spin state of Mn_{12}-based SMMs is controllable; Mn_{12} derivatives can be prepared in one-electron to four-electron reduced versions by adding reducing agents, such as iodide salts to solutions of Mn_{12} clusters. The inner core of the SMM in all modifications remains essentially the same.
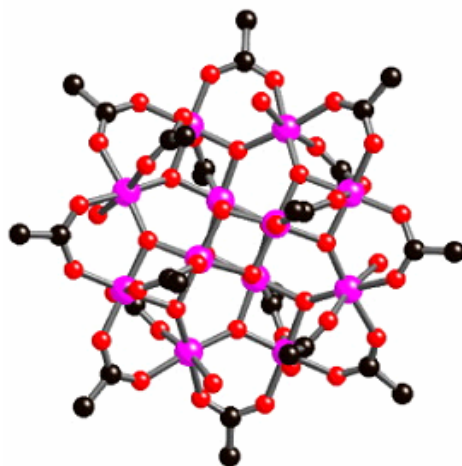
Fig. 5. Schematic view of the magnetic core of Mn_{12}-based SMM. Pink symbols stand for Mn atoms, red for O atoms, and black for C atoms.

The half-integer spin samples, $PPh_4[Mn_{12}O_{12}(O_2(CEt)_{16}(H_2O)_3]$ (r-Mn_{12}Bz), were obtained in [50]. The cluster had a ground spin state S=19/2 and energy barrier $\Delta E/k_B$ ~58.4 K (cf. for Mn_{12}Bz the energy barrier was 70.3 K). As was shown in [50], the integrity of the ground spin state influences also the form of the hysteresis curve. The spin-reduced samples did not present well-resolved steps around 4 and 8 kOe, which suggests thermally activated quantum tunneling to be less efficient in half-integer spin system. This effect is explained by a spin parity effect. The effect predicts that quantum tunneling will be suppressed at zero applied magnetic field for half-integer spin systems, but is allowed in integer-spin systems, by Kramers theorem [51].
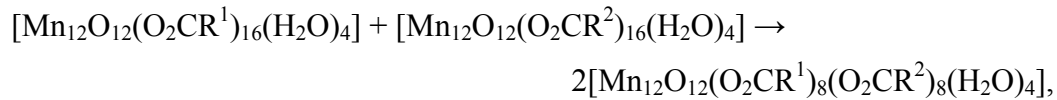
2.2.3. Synthesis of Mn_{12}-based single molecular magnets

The chemical methods of the synthesis of Mn_{12}-based SMMs are based on molecular recognition, host-guest interactions and self-assembly principles, although the structural and electronic requirements for SMM behavior are so demanding that still there are no general synthesis routes.

The prototype SMM Mn_{12}-acetate was synthesized by a one-pot reaction of $Mn(O_2CCH_3)_2 \cdot 4H_2O$ and $KMnO_4$ in CH_3CO_2H/H_2O [38]. Since then, many Mn_{12} derivatives (including Mn_{12}-benzoate studied in this thesis) have been prepared by a similar scheme.

10

Another popular method is ligand substitution applied to Mn_{12}-acetate, when Mn_{12}-acetate and an excess of a carboxylic acid $R-CO_2H$ are stirred in a solvent resulting in an exchange reaction between CH^3CO^{2-} and $R-CO^{2-}$.

In comparison to homocarboxylates, the preparation of mixed-ligand complexes is considerably more challenging. They can be synthesized by ligand redistribution:

$$[Mn_{12}O_{12}(O_2CR^1)_{16}(H_2O)_4] + [Mn_{12}O_{12}(O_2CR^2)_{16}(H_2O)_4] \rightarrow$$

$$2[Mn_{12}O_{12}(O_2CR^1)_8(O_2CR^2)_8(H_2O)_4],$$

but the most successful way to obtain mixed-ligand Mn_{12} complexes is to add a stoichiometric amount of the required incoming ligand to homocarboxylate.

It is important to mention that, although the basic structure of the Mn_{12} core is preserved upon ligand replacement, the arrangement of axial water and carboxylate ligands may differ from that observed in Mn_{12}-acetate. The different ligands are usually arranged at specific sites depending on the strength of the ligand-to-metal interaction, i.e. the exchange reaction is site- selective [52].

2.2.4. Theory of single molecular magnets

Let us take a closer look on the quantum tunneling process in integer-spin system. The possibility of observing tunneling depends on how much the wavefunctions of the two states overlap. The overlapping splits degenerate levels in both wells; one of the split levels is higher and the other one is lower on the energy scale than the degenerate level. Thus, the possibility of tunneling is defined by the relative energies of the tunnel splitting and of the barrier. In assumption, the interaction between the wavefunctions is described by Equation 1 [52]:

$$H = H_0 + H_1 + H_2, \qquad (1)$$

where H_0 is an unperturbed Hamiltonian that describes interaction between two equivalent wells and also the effects of an external magnetic field parallel to the system axis and its splitting as a result of crystal-field interaction (Zeeman effect), H_1 is a perturbation that removes degeneration of the states, H_2 is a part that describes interaction with the environment.

Let us assume that a magnetic field is applied in the z direction, which corresponds to the magnetic anisotropy axis of the molecule. Then the unperturbed second-order Hamiltonian can be written as follows:

$$H_0 = D(S_z^2 - S(S + 1)/3) + \mu_B g M_s H_z. \qquad (2)$$

When D<0, a double-well potential is formed, which is a key factor to create a magnetic memory effect. The $|D|S^2$ barrier blocks spin reorientation transitions between $M_s=-S$ and $M_s=+S$ states and keeps the magnetization fixed along the z axis at low temperatures.

As for Mn_{12} system $S = 10$, the corresponding energies of the spin levels are given by Equation 3:

$$E(M_s) = D(M_s^2 - 110/3) + \mu_B g M_s H_z. \qquad (3)$$

When the magnetic field is absent, all states, except for $M_s = 0$, are degenerate and wells are equally populated. The separation between M_s and M_{s+1} levels is equal to $|D|(2|M_{s+1}| - 1)$. When a large magnetic field is applied, at low temperatures only the $M_s = -10$ state will be populated. After the field is removed, the relaxation of the magnetization process can be expressed as a function of time:

$$M(t) = M(0)\exp(-t/\tau), \qquad (4)$$

where τ is the relaxation time. The relaxation process can happen due to the interaction between the system and the environment. Villain et al. obtained the equation for the relaxation time in the limit of $\Delta E \gg k_B T$ and weak magnetic field [53]:

$$\tau = \tau_0 \exp(\Delta E/ k_B T), \quad \text{where } \tau_0 = \frac{2\pi\hbar^2 \rho c^5}{3|V_{10}|} \cdot \left(\frac{S^2}{\Delta E}\right)^3. \qquad (5)$$

Here V_{10} is a matrix element for spin-phonon coupling, ρ and c are the speed of sound in the material and vacuum, respectively. The relaxation process follows the Arrhenius law, and this behaviour is similar to that of superparamagnets.

The relaxation time quickly decreases with increasing temperature. Thus, for Mn_{12}-acetate $\tau \sim 50$ years at 1.5 K and is less than a second already at 6 K. Fast magnetization relaxation occurs due to the thermal populating of low-spin levels – the tunneling rate for the next-to-smallest level $M_s=9$ is $\sim 10^8$ times bigger, that is why the actual T_B is much lower than $|D|S^2$, in fact, it is determined by the energy gap between the ground and the lowest excited spin states.

Now let us consider a zero field case. As long as the Hamiltonian H_0 is valid, all states are orthogonal to each other and the tunneling is absent. If we want tunneling to be possible, we must include magnetic anisotropy effects into consideration, i.e. H_1 perturbation:

$$H_1 = E(S_x^2 - S_y^2), \qquad (6)$$

where E is a transverse anisotropy parameter. The wavefunctions are partially delocalized, and the eigenstates are described by a mix of $|M_s\rangle$ states, where only those, which differ by ±2, couple directly. For example, $M_s = 10$ will be coupled with $M_s = 8$, $M_s = 8$ with $M_s = 6$, $M_s = -10$ with $M_s = -8$, but for $M_s = 10$ and $M_s = -10$ interaction will be very low: in the tenth order of perturbation theory. For higher energy levels the situation is different, and interaction between $M_s = 2$ and $M_s = -2$ exists in the second order of perturbation theory. It is clear that the larger M_s is the smaller the splitting will be. Tunneling may occur not only between the ground states $M_s = ±10$, but also between pairs of excited states. Such tunneling is called thermally activated, or phonon-assisted, and it becomes very important with rising temperature.

If we apply a magnetic field, the energies of M_s levels will change rapidly with a slope equal to $\mu_B g M_s$, and $±M_s$ pairs will no longer be degenerate. However, as the field increases, the energy of $M_s = 10$ increases and the energy of $M_s = (-10 + N)$ decreases, and at some magnitude of magnetic field they meet, restoring the conditions for tunneling. The field at which this happens is defined by Equation 7:

$$H_z(N) = ND/\mu_B g, \text{ where } N = 0, 1, 2\ldots \qquad (7)$$

The splitting energy gap Δ oscillates with a period given by Equation 8:

$$\Delta \cdot H_z = \frac{2k_B}{\mu_B g}\sqrt{2E(E+D)} \qquad (8)$$

The oscillations are explained by constructive or destructive interference of quantum spin phases (so-called Berry phases). They are repeated 10 times, and beyond field $H_z = 21\sqrt{E(E+D)}/\mu_B g$ are quenched.

Experimentally, some of the tunneling parameters can be estimated from dc magnetic measurements [54]. For example, the dc magnetic susceptibility data (χ_M) give the g-factor and spin ground state, as the effective barrier height scales as

$$\mu_{eff} = (8\chi T)^{1/2} = g(S(S+1))^{1/2}. \qquad (9)$$

The order of magnitude for the D value can be found from the first derivatives of hysteresis loops:

$$D = -\Delta H \cdot g / 2, \qquad (10)$$

where ΔH is the mean value of the step between quantum transitions. This gives us the energy barrier height $\Delta E / k_B = S^2 |D|$ for SMM with integer ground spin state and $\Delta E / k_B = (S^2 - \frac{1}{4})|D|$ for SMM with half-integer ground spin state.

2.3. Nanoporous carbon

Nanoporous carbon (NPC) is a bulk carbon material, which has porosity on the nanometer scale. The porous structure of NPC is very complex, and its actual geometry depends on the synthesis process [55]. Roughly, it can be described as intermediate between amorphous carbon and perfectly crystalline graphite. NPC is formed by pyrolysis of carbon-containing materials (polymers, graphite, metal carbides, etc.) in an inert atmosphere. During this process, gas atoms escape from the initial product, which results in a complex pore-ridden structure of mostly sp^2 carbon with a high specific surface area and controllable pore size. These highly porous materials have a variety of existing and possible applications: from traditional catalysis [56] and purification [57-58] to CH_4 and H_2 storage [59-61], supercapacitors [62-64], cryogels [65] and certain medical treatments [66], and may provide a starting point for producing more highly structured nanomaterials.

2.3.1. Synthesis of nanoporous carbon

Nanoporous carbon materials can be produced by pyrolysis [67-70], arc discharge [71], laser ablation [72] or supersonic cluster beam deposition [73]. The most common method to synthesize NPC is pyrolysis of carbon-containing materials, such as hydrocarbons [67-68] or carbides [69-70].
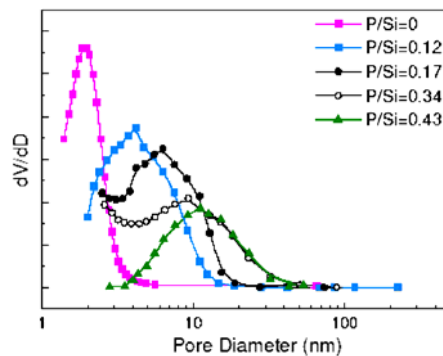

Fig. 7. Tunable pore size distribution of NPC synthesized in [74].

During pyrolysis of hydrocarbons, the primary material is heated to 400-1200^{0}C in an inert atmosphere in several steps, and the resulting NPC material comes from two competing processes, carbonization and graphitization.

Selective extraction of metal atoms from the carbide lattice was historically the first method to produce NPC. When exposing hot carbide to dry halogen-containing gas, the formation of NPC follows the chemical reaction equation:

$$\mu MeC + 0.5\ \nu Ha_2\ (gas) \rightarrow \nu MeHa\ (gas) + \mu C \qquad (1)$$
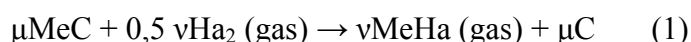
where Me is a carbide former (Si, Ti, Zr), Ha is a gaseous halogen-containing etchant (Cl_2, F_2, HCl), and μ, ν are stoichiometric coefficients. Halogene "eats away" atoms of the carbide former, leaving the carbon atoms and the voids.

It is possible to calculate the total weight-based theoretical pore volume V_{tot} using Equation 2:

$$V_{tot} = 1/\ N_{carbon} \cdot \rho_{carbide} - 1/\rho_{carbon} \qquad (2)$$

where N_{carbon} is a weight fraction of carbon in the initial carbide material, ρ_{carbon} and $\rho_{carbide}$ are the density of carbon and carbide, correspondingly.

Alternative relatively inexpensive feedstock to prepare NPC is anthracite [75-76]. These methods produce disordered NPC even though the pore size distribution is quite narrow. In order to improve the structural order of the material, the pyrolysis is performed in the presence of a template with ordered porosity (such as zeolite) [77].

2.3.2. Defect-induced magnetism of carbon

Pristine carbon materials are strongly diamagnetic. However, since the early 2000s, the existence of ferro- (antiferro-) magnetic ordering in these materials has become a widely discussed problem. The topic used to be controversial, and experimental observations of magnetism often have been attributed to parasitic signal from transition metal impurities [78]. Gradually, magnetism of carbon allotropes has been getting recognition, though the nature of magnetic ordering in all-carbon materials, such as fullerenes [79], highly oriented pyrolitic graphite (HOPG) [80], or carbon nanofoams [81], is still not completely clear. Among possible explanations are edge states localized at zigzag edges [82], topological

defects [80], unsaturated dangling bonds [83], mixture of sp^2- and sp^3-hybridized bonds [84], etc. One thing so far seems evident: for the rise of the unconventional magnetism of carbon, irregularities of the carbon lattice are crucial.

Numerous theoretical studies of graphene have revealed that single carbon atom defects, e. g. vacancies and hydrogen chemisorption [85], induce magnetic moments depending on the defect concentration. Furthermore, the presence of a foreign atom, such as nitrogen [86] or boron [87], nearby a vacancy defect can enhance the magnetic response of the system as compared to a standalone carbon vacancy.

Finite graphene fragments of certain shapes, triangular or hexagonal nanoislands [88], graphene nanoribbons [89], or variable-shaped graphene nanoflakes [90], as well as some "Star of David"-like fractal structures [91] possess a high-spin ground state and behave as artificial ferrimagnetic atoms. In these materials, the role of edges becomes very important. The non-bonding states have a large local density of states in the zigzag edge region, with localized π-spins populated around the zigzag edge region. Edge state magnetism has been studied on realistic edges of graphene, and it was shown that only the elimination of zigzag parts with n>3 will suppress local edge magnetism of graphene [92]. The authors of [93] have suggested that the edge irregularities and defects of the bounding edges of graphene nanostructures do not destroy the edge state magnetism.

The first direct experimental observations of a room-temperature ferromagnetic signal coming from point defects in graphite were done in MFM measurements performed by Červenka et al [94]. Ferromagnetism depending on the irradiation dose has been reported for graphite irradiated with protons [95], helium [96], and carbon ions [97].

Overall, the area of intrinsic magnetism of carbon structures is still at the early stage of research, and much effort is needed for a better understanding of the mechanisms of magnetic ordering.

2.3.3. Magnetic properties of nanoporous carbon

There are two different approaches to the modeling of the NPC structure. The "defect approach" views the pores as voids in the graphite lattice, which come from multiple-atom vacancies giving pore sizes in the range 0.5–1 Å, and the NPC structures are viewed as crumbled graphene sheets that contain both pentagons and heptagons (**Fig. 6a**). The other perception is that the NPC can be described by a periodic minimal surface (PMS) called schwarzite (**Fig. 6b**). The simplest example of a PMS is an infinite cylinder (repetition of a

cylindrical segment). Complex PMS structures are characterized by a number of channels, which, in various ways, connect the neighboring volumes into a porous network.
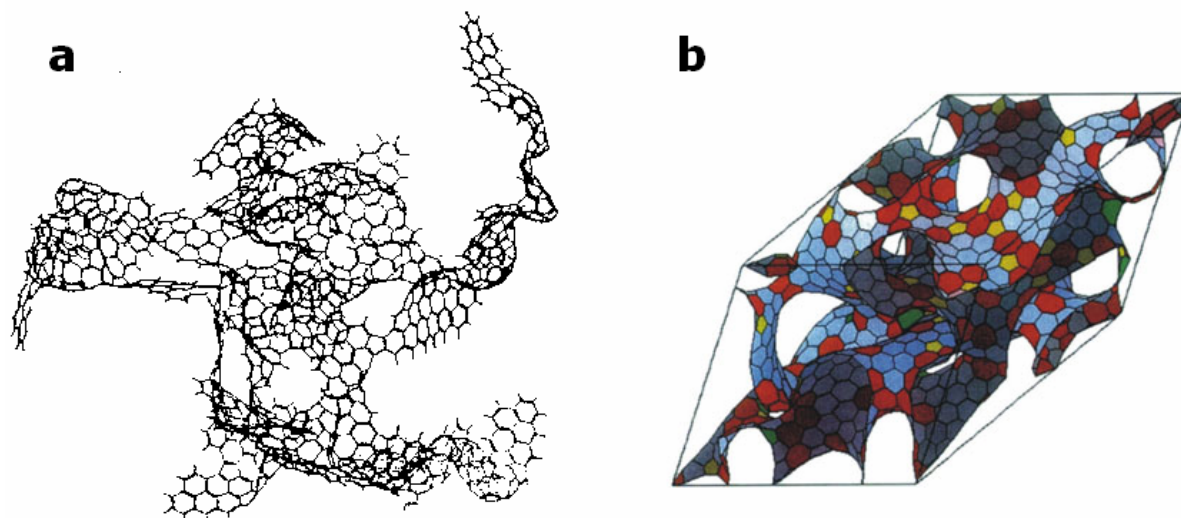

Fig. 6. a – structure of NPC generated by randomly assembling random graphene flakes [98], b – structure of a random Schwarzite [99].

In the case of the defect model, the magnetic moment in NPC is believed to appear from perturbation of the π-bands in the electronic structure of the graphite lattice, which originates from structural disorder [82, 100-101].

The schwarzite model is more widely used to describe the properties of carbon materials with ordered porosity, such as zeolite-templated carbon with the regularly aligned array of nanopores investigated in [102], although random schwarzites with an irregular pore structure give a good representation for disordered NPC as well [84]. The origin of magnetic moment in this model is attributed to unpaired spins, which are localized in hyperbolic saddle-like regions of schwarzite with negative Gaussian curvature.

Experimental studies have revealed that NPC, being a pure carbon material, can show spin-glasslike [101] or ferromagneticlike [84, 100, 103] behaviour and preserve notable values of magnetization up to room temperature.

2.4 Intercalation compounds of graphite fluorides

Intercalation compounds of graphite fluorides (ICGF) are quasi-two-dimensional layered structures, which were systematically investigated during 70 – 80^s of the 20th century. ICGF are synthesized by reaction of graphite with fluorine gas under specific conditions. The chemical composition of fluorinated carbons depends on both the structure of the

starting material and on the fluorination conditions [104]. ICGF have commonly been used as solid lubricants [105] and electrodes in batteries [106]. Nowadays, fluorine-induced localized spins [83, 107-109] make fluorinated carbons a subject of interest for possible magnetic applications.

2.4.1. Graphite intercalation compounds

The term intercalation, in chemistry, describes a reversible insertion of foreign species, such as atoms, ions or molecules into a lamellar host structure, while the general structural features of the host are preserved. Graphite has a layered structure, and the graphite layers can be separated to accommodate the guest in the so-called van der Waals gap. As a result, the interlayer spaces increase considerably and can reach ~1 nm [110] (from 0,335 nm for pristine graphite). Intercalation compounds have a high variation of composition, as the percentage of the intercalated material changes by regular steps. Intercalation reactions follow several steps: (1) initial interaction of the guest with the host lattice to separate the layers, (2) initial penetration of the guest into the host, (3) diffusion of the guest species in the layers, and (4) continued entry of the guest until equilibrium is achieved.
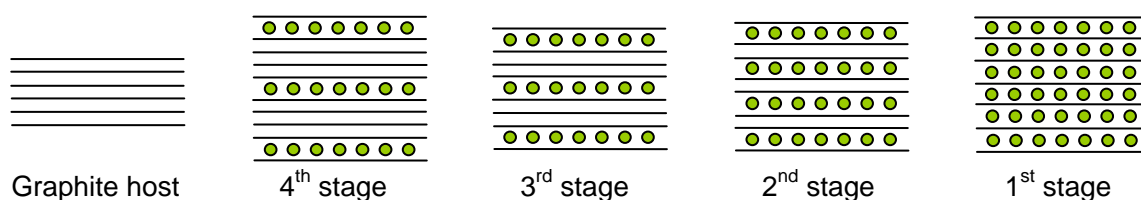

Fig. 8. The stages of graphite intercalation compounds. Addition of guest species goes through n = 4..1.

The number of graphene layers between adjacent intercalate layers is denoted as stage index n, as is illustrated in **Fig. 8**. Interestingly, the lowest stage of the intercalated compounds depends on the intercalant nature. For example, for Br_2 intercalation, the lowest stage that has been reported is a stage 2 compound [110]. In the first stage, intercalation reaches a maximum, and the material, known as a first-stage compound, is considered stoichiometric.

2.4.2. Structure of intercalation compounds of graphite fluorides

Traditional agents for the fluorination of graphite are molecular F_2 (at elevated temperature) or other gaseous fluorine-containing compounds (BrF_3, IF_7, XeF_2, etc). Structural properties

and composition of the obtained compounds depend on the methods of synthesis, as well as the structure of the starting carbon material [104].

Introduction of fluorine drives the carbon network from a π-electron/sp^2 system into a sp^2/sp^3 mixed system, where sp^3 bonding appears at carbon sites, with which fluorine reacts. A layer of fully fluorinated CF consists of trans-linked cyclohexane chairs, in which all carbon atoms are sp^3-hybridized and covalently bonded to fluorine atoms [111].

A chemical peculiarity of ICGF C_2F_x is that the common approach - the introduction of intercalants into the pristine host matrix – is not possible. First, graphite is intercalated with "primary" intercalants, which have to be replaced by fluorine-containing species by methods of substitution. The residual agents are then washed out with organic solvents. Therefore, we always speak of inclusion compounds: a C_2F_x matrix with intercalated guest organic molecules [112].
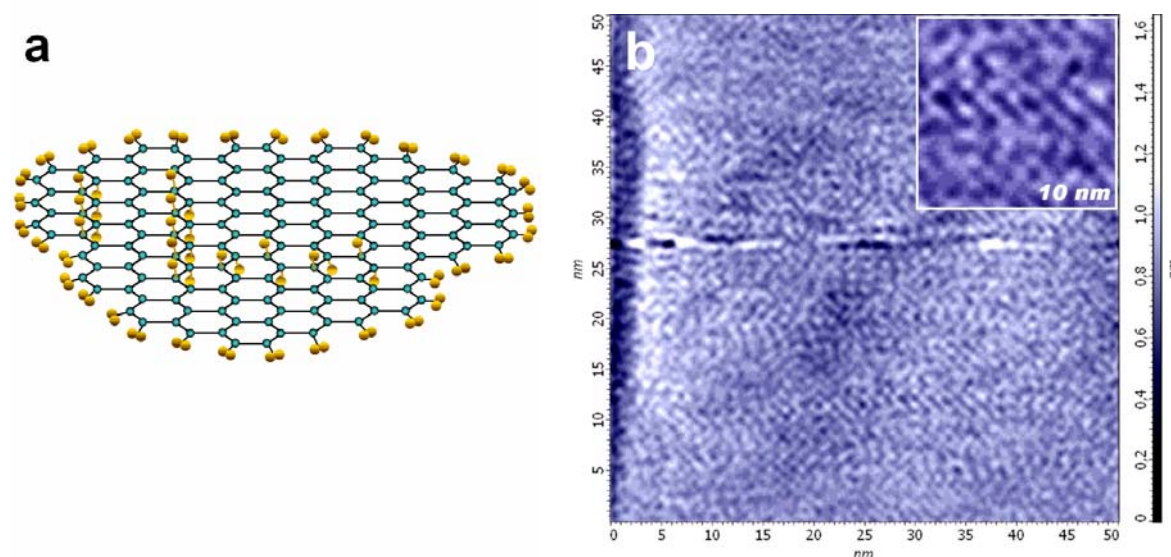

Fig. 9. a – structure of semi-fluorinated graphite C_2F (blue – C atoms, yellow – F atoms); b – AFM image of the fluorinated HOPG sample [113]. Light regions correspond to fluorinated carbon atoms, and dark regions correspond to unfluorinated carbon atoms

In semi-fluorinated graphite C_2F, every second carbon atom is bound to a fluorine atom. As was shown by Okotrub et al. [113], fluorine atoms are self-assembling into a parquet-like structure on graphitic layers. Fluorine forms both zigzag and armchair chains with the stoichiometry CF-CF-CF-CF alternating with chains of non-fluorinated C-C-C-C (see **Fig. 9a**). In the atomic force microscopy (AFM) image (**Fig. 9b**), the structure of graphite fluoride is represented as regular light and dark bands with characteristic length of several nm.

It can be proposed that light regions correspond to fluorinated carbon atoms, while dark regions correspond to unfluorinated areas.

2.4.2. Magnetic properties of modified graphite

In addition to magnetism triggered by the localized states coming from topological defects, which is discussed in Chapter 2.3.2, there is another possible mechanism of magnetic ordering in graphite. Localized spins can be created due to the presence of σ-dangling bonds, when the flat sp^2/π hexagon network of a graphene sheet is locally destroyed by bonding a foreign atom, such as hydrogen or fluorine to a carbon atom in the interior of a graphene sheet.

Graphane is a theoretically predicted graphene derivative, where each carbon atom is bonded to a hydrogen atom. Without defects fully hydrogenated graphane should be a non-magnetic semiconductor. But graphane with H-vacancies is predicted to be magnetic and can even become a room-temperature ferromagnet [114-115]. Modification of the carbon lattice by hydrogen chemisorption is shown to be a more effective mechanism to induce ferromagnetic ordering compared to vacancy defects [116].

A more complex structure of graphene functionalized with oxygen on the upper side and hydrogen from the bottom is found to be a ferromagnetic metal, while graphene functionalized with fluorine is an antiferromagnetic semiconductor [117]. Antiferromagnetic ordering is also predicted for partially fluorinated graphene nanoribbons [118].

However, despite promising theoretical predictions, there's a lack of experimental confirmation of magnetism in modified carbon structures. Fluorinated carbon nanofibers studied in [107] exhibit a Curie-Weiss (CW) temperature dependence of the magnetic susceptibility, which is assigned to localized moments produced at the carbon sites neighboring to the carbon sites, to which fluorine atoms are bonded. When the ratio of fluorination is 0.4<F/C<0.8, the spin concentration reaches a maximum and quickly decreases above this ratio. Fully fluorinated perfect CF is a nonmagnetic insulator. In a recent paper by Nair et al. [78], it was shown that fluorine adatoms in fluorinated graphene CF_x, with x = 0.1..0.9, similarly to irradiation defects, carry magnetic moments with spin 1/2. Fluorination of graphene introduced strong CW paramagnetism, but no sign of magnetic ordering was found down to 2 K. The disagreement between theory and experiment is attributed to the cancellation of magnetic moment due to the exchange interactions between neighboring fluorine vacancies in the fluorinated carbon sheet [119].

However, larger unfluorinated domains in CF_x structures can possess stable magnetic moments.

3. Experimental techniques

3.1. Vibrational spectroscopy

3.1.1. Basic principles

In Raman spectroscopy, the sample is irradiated with monochromatic light (the source is usually a laser). Most part of the scattered light will have the same frequency as the incident light – this process is known as Rayleigh scattering. Nevertheless, a certain amount of light scattered by the sample, approximately one photon in a million (0.0001%), will have a frequency offset relative to the frequency of the laser source. As shown in the diagram below, the electric field of the laser raises the energy of the system to an unstable state, inducing the polarization of the chemical groups. The polarized state is not a true energy state and is called a "virtual state". Relaxation from the virtual state occurs almost immediately, and generally the system relaxates back to the ground state (Rayleigh scattering); relaxation to the first excited vibrational state is called Stokes-Raman shift. Most systems have some initially excited molecules. If these molecules relaxate from excited vibrational state to the ground state, this type of scattering is called anti-Stokes Raman scattering.
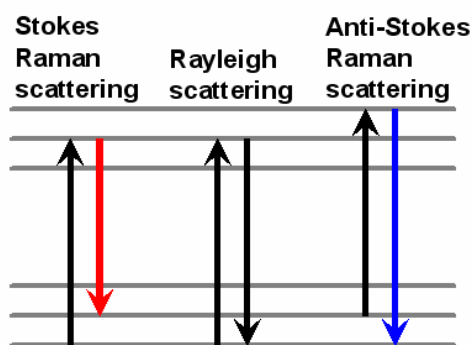

Fig. 1. Scattering diagram.

The Raman scattering transition moment is defined as $R = <X_i \mid P \mid X_j>$. Here X_i and X_j are the initial and final states, respectively, and P is the polarizability of the molecule which shows how tightly the electrons are bound to the nuclei. To observe vibrations in the Raman spectrum, the polarizability of the molecule should change, and the intensity of Raman lines are proportional to the square of the change in polarizability.

The mechanism of Raman scattering is different from that of infrared (IR) absorption. The transition moment for infrared absorption is defined as $R = <X_i \mid U \mid X_j>$ where X_i and X_j

are the initial and final states, respectively, and U is the electric dipole moment operator. To observe vibrations in the IR absorbtion spectrum, it is necessary that the dipole moment of the molecule is changed during vibrations (this does not mean that the molecule must have a permanent dipole moment). The intensity of the observed line in spectrum is proportional to the square of the change in dipole moment.

To conclude, the vibrations of polar groups of atoms, in the general case, can be seen in the IR spectrum, while the vibrations of the nonpolar groups can be seen in the Raman spectrum, and the combination of IR and Raman spectroscopy allows to investigate the entire set of the sample's vibrations, i. e. these methods are complementary.

The Raman spectra were recorded using a Raman spectrometer Renishaw 100 at the wavelength 514 nm. The FT-IR spectra were recorded at room temperature on a Perkin Elmer-1720X spectrometer.

3.1.2. Raman spectrum of graphite

The first order Raman spectrum of graphite classically presents three bands: the G band at 1582 cm^{-1} (graphitic), the D band at about 1350 cm^{-1}, and the D'-band at about 1620 cm^{-1} (for laser excitation wavelength 514.5 nm).
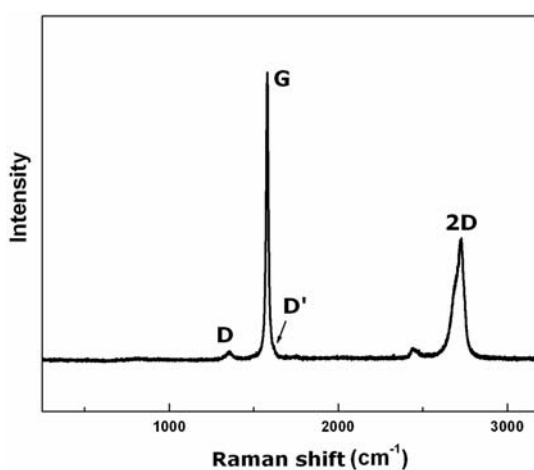

Fig. 2. Raman spectrum of graphite.

The G band is a doubly degenerate (iTO and LO) phonon mode (E$_{2g}$ symmetry) at the Brillouin zone center. In perfect graphite, the E$_{2g}$ vibration mode of the carbon atoms at ~1580 cm^{-1} [120-121] indicates that the sample contains sp^2 carbon networks. The D and D' bands are defect induced and these bands cannot be seen for a highly crystalline graphite.

Tuinstra & Koenig [122] showed that the intensity of the D band compared with the Raman-allowed E_{2g} mode depends on the size of the graphite microcrystals in the sample. The D/G ratio gives us an important characteristic of graphite: L_a, or coherence length. This parameter determines the dimension of graphitic domains. One can easily guess that fluorination will progressively decrease the graphitic islands, and L_a will be decreased. The size reduction of the graphitic domains can be evaluated from the relative intensities of the D and G Raman bands by using the empirical formula:

$$L_a \text{ (nm)} = \frac{560}{E_{laser}^{\ 4}} \cdot (\frac{ID}{IG})^{-1} \quad (1),$$

where E_{laser} is the excitation laser energy (in eV) used in the Raman experiment. For λ=514 nm, the coefficient is equal to 4.4.

The D mode also appears in the second order spectrum (2D mode at about 2700 cm^{-1}) and has a double peak structure. For ideal graphite, the difference between the peak positions in the second order spectrum is 42 cm^{-1}. The shape and position of the 2D peak is a very good tool for analyzing the stacking sequence of graphite: when the ABAB sequence is damaged, the peak becomes smeared. In turbostratic graphite there is no stacking order between adjacent layers, and 2D band is composed by a single peak, indicating that the interaction between the graphitic planes is weak enough so that the splitting in the π-electrons dispersion energies does not occur [123].

When one deals with single- or multilayer graphenes, the difference between the peak positions in the second order spectrum provides a possibility to calculate how many graphene layers are in the stacking sequence, from 1 to 6 layers can be distinguished [124].

3.1.3. Raman spectrum of fullerenes

The vibrational spectrum of a prototype fullerene, C_{60}, has all characteristics common for molecules. Since the symmetry of C_{60} is I_h – the highest possible, the Raman spectrum is fairly simple. The molecule has 46 vibrational modes distributed over the 174 degrees of freedom. A typical spectrum of a C_{60} single crystal is presented below on **Fig. 3**.

It is now accepted that the position of the $A_g(2)$ mode is 1469 cm^{-1}; this mode broadens and softens from 1469 cm^{-1} to 1458 cm^{-1} under the influence of daylight due to phototransformation processes.
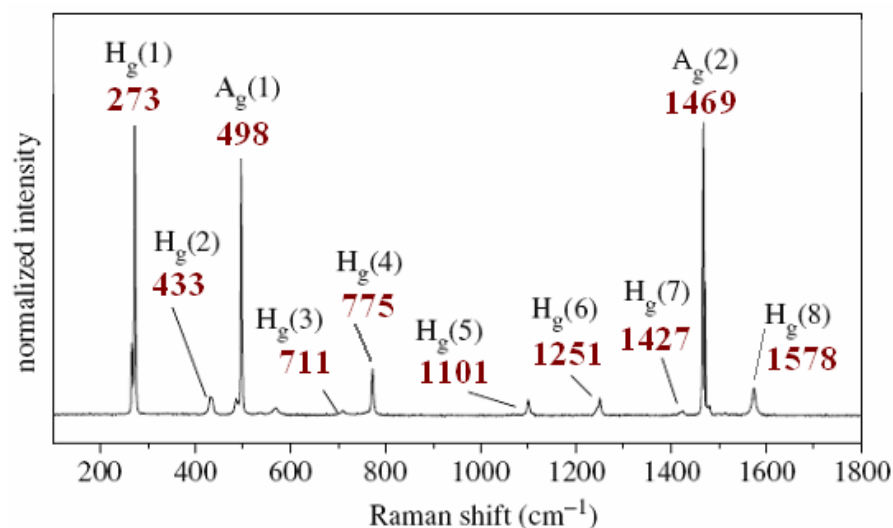
Fig. 3. Raman spectrum for C_{60} single crystal (modified from [125]).

Fullerenes have high electronegativity and therefore can be good electron acceptors. In the presence of strong donor atoms (for example, alkali metals) they tend to fill up their highest unoccupied levels. It strongly influences the structure of fullerite and its vibrational spectrum, causing C_{60} modes to shift.
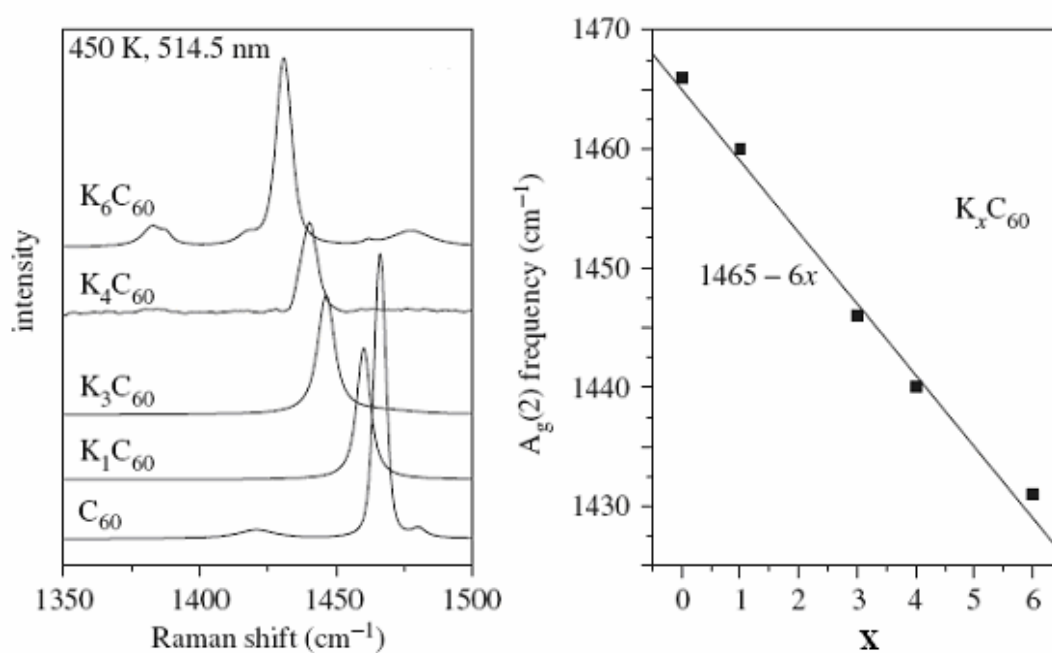

Fig. 4. Shift of $A_g(2)$ frequency of C_{60} with increased charge transfer [125].

Fig. 4 shows the shift of the most prominent pentagonal pinch mode, $A_g(2)$ for various K_xC_{60} compounds. The shift of the selected mode can be used to determine the amount of charge transfer. The $A_g(2)$ mode shifts by about 6 cm^{-1} downwards per elementary charge.

3.1.4. Raman spectra of carbon nanotubes

The first-order Raman spectrum of single-walled carbon nanotubes always contains three strong bands: the radial breathing mode (RBM) associated with a symmetric movement of all carbon atoms in the radial direction, the D mode and the G mode (see **Fig. 5**).
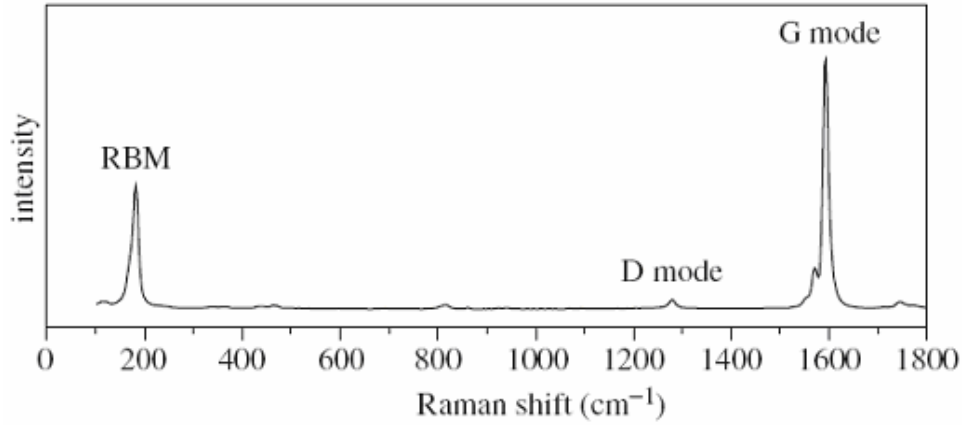

Fig. 5. Raman spectra of SWCNTs with mean diameter 1.35 nm [126].

Here, the three most important modes are RBM at around 180 cm^{-1}, the defect mode (D) at around 1350 cm^{-1} and the tangential mode derived from E_{2g} graphite mode (graphitic, G) at around 1580 cm^{-1}.

It was shown that the RBM frequencies can be used for estimating the diameters of the tubes. For isolated nanotubes we get:

$$\upsilon_{RBM} = C_1/d, \qquad (2)$$

where C_1 is a constant equal to ca. 233 cm^{-1}. For nanotubes in bundles we should take into account the van der Waals interaction between them, and Equation 2 transforms into:

$$\upsilon_{RBM} = C_1/d + C_2, \qquad (3)$$

where the value of constant C_2 is about 10 cm^{-1}. In fact, the procedure of determining the tube diameter is more complicated, as we always have a distribution of diameters, which is described by a Gaussian function. If the diameters of nanotubes are estimated from Equations 2 or 3, information about excitation levels and electrical properties of the nanotubes can be obtained from the Kataura plot. In the multi-walled carbon nanotube Raman spectrum the RBM mode is absent.

The D (defect) mode has a linear dependence on the laser excitation energy. This band is activated in the first-order scattering process of sp^2 carbon atoms by the presence of defects and by finite-size effects, which decrease the crystal symmetry, and that is why the intensity of the D band is proportional to the phonon density of states.

The G (graphitic) mode has two components, the lower frequency component associated with vibrations along the circumferential direction, G^-, and the higher frequency component, G^+, attributed to vibrations along the direction of the nanotube axis. The most important aspect of the G mode is the characteristic Raman lineshape which depends on the electrical properties of the nanotube, which allows distinguishing between metallic and semiconducting ones.

In **Fig. 6** one can see spectra of iron-filled nanotubes with a low filling of iron produced using different iron sources.
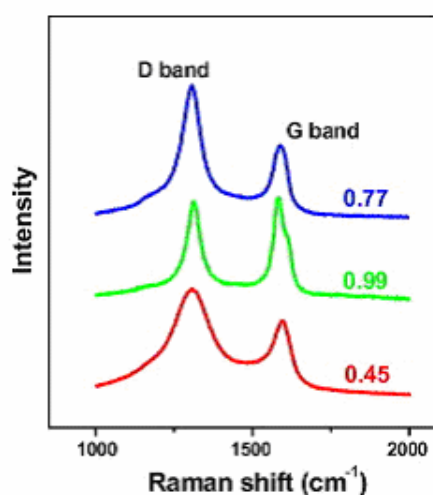

Fig. 6. Raman spectra of multi-walled carbon nanotubes with low filling: ferrocene (blue), acethylferrocene (green), iron (II) nitrate (red) [127].

Only the D- and G-modes were active in the sample and no RBM signal was detected. The estimate of the sample purity is based on the ratio of the intensities of the graphitic mode and the defect mode.

3.2. X-ray diffraction

3.2.1. Basic principles

X-rays are electromagnetic radiation with a high energy and a very short wavelength. They are produced when electrically charged particles of sufficient energy are decelerated. In an X-ray tube, the high voltage maintained across the electrodes drives electrons toward a

metal target (the anode). This tube has two metal electrodes that are placed in a vacuum chamber [128]. When an X-ray beam falls on a crystal lattice, scattering will be observed. X-ray diffraction (XRD) is a widely used method to determine the crystal structure of a material. Each crystalline material has a unique characteristic atomic structure thus it will exhibit a characteristic diffraction pattern. When an x-ray beam reaches a plane of atoms, they serve as a mirror and scatter the incoming radiation by a specific phase. Waves scattered from atoms in parallel planes have a phase difference of multiple integer numbers of wavelengths. These waves interfere constructively, and a peak appears in the diffraction pattern. This condition is called Bragg diffraction [129] and formulated as:

$$n\lambda = 2d_{hkl}\sin\theta \qquad (1)$$

where n is the order of reflection which is an integer number, λ is the wavelength of the incident x-ray beam, d is the interplanar spacing between crystal planes, and θ is the angle between the incident ray and the plane it scattered from. The formula tells that if one knows the angles where the peaks appear then it possible to determine the interplanar distance between the planar crystal planes, d_{hkl}, where *(hkl)* are integer numbers and are called the Miller indices.

Miller indices define the orientation of the crystal plane in a lattice, in other words sites where the crystal planes intersect the lattice.
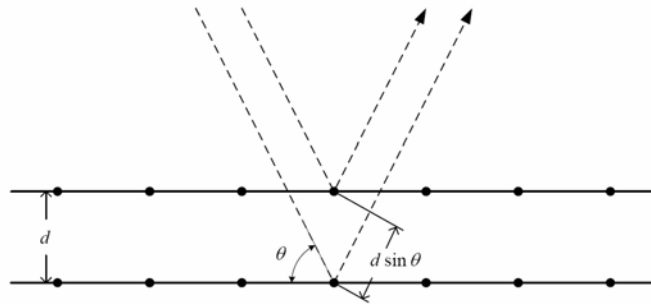

Fig. 7. Scheme of X-ray diffraction from atomic planes.

Equivalent and parallel planes are defined by the same Miller indices. They can be described by reciprocal basis vectors [130] which are defined as follows:

$$\vec{a}^* = 2\pi \frac{\vec{b} \times \vec{c}}{\vec{a} \cdot (\vec{b} \times \vec{c})} \ , \ \vec{b}^* = 2\pi \frac{\vec{c} \times \vec{a}}{\vec{b} \cdot (\vec{c} \times \vec{a})} \ , \ \vec{c}^* = 2\pi \frac{\vec{a} \times \vec{b}}{\vec{c} \cdot (\vec{a} \times \vec{b})} \qquad (2),$$

28

where $\vec{a} \cdot (\vec{b} \times \vec{c})$ is the volume of the unit cell. Then the reciprocal lattice vector can be defined as:

$$\vec{G}_{hkl} = h \cdot \vec{a}* + k \cdot \vec{b}* + l \cdot \vec{c}* \quad (3).$$

The *(hkl)* crystal plane intercepts crystal axes and it relates to Miller indices as *(hkl)* ~ (1/x, 1/y, 1/z). The G_{hkl} vector is perpendicular to the parallel crystal planes, and it is related to interplanar distance d_{hkl}:

$$d_{hkl} = \frac{2\pi}{G_{hkl}} \quad (4).$$

It is possible to derive a general formula to determine the interplanar distance for graphite, which has a hexagonal atomic structure. It is defined as the following [131]:

$$d_{hkl} = \frac{1}{\sqrt{\frac{4}{3}(h^2 + k^2 + hk) + \frac{l^2}{c^2}}} \quad (5),$$

where c is the lattice constant.

3.2.2. The setup

XRD studies were performed at a Siemens/Bruker D5000 diffractometer in *θ - 2θ* geometry. The radiation is generated by an X-ray tube with a Cu anode, and then filtered, and the two Cu K_α lines, 1.5405 and 1.5443 Å, are used for the measurements. The resulting spectra are calculated using a mean value for K_α.
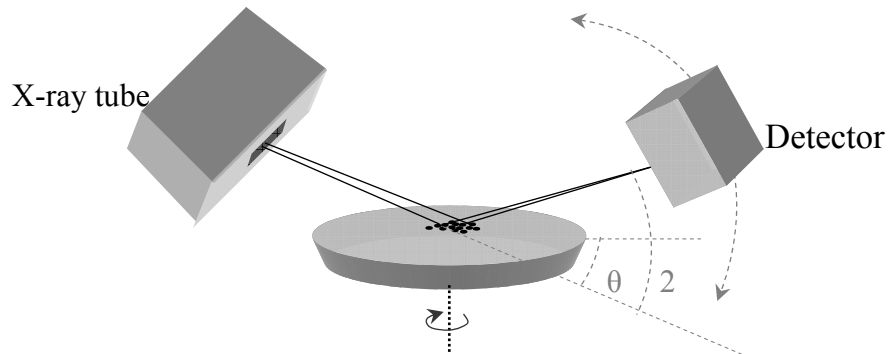

Fig. 8. X-ray diffraction setup.

During the measurement, a beam of X-rays hits a rotating sample (15 rotations per minute) at an angle *θ*. The beam exiting the X-ray tube is slightly expanded in order to reach most

of the sample material. The diffracted radiation is focused and collected by a scintillation counter at an angle 2θ with respect to the incident radiation.

To obtain diffraction data over a range of angles, the positions of both sample holder and detector are continuously adjusted with a goniometer to follow the θ - 2θ geometry. In our experiments, the detector scanning speed was 0.02 deg/min.

3.3. SQUID magnetic measurements

3.3.1. Design and components of the setup

A Quantum Design Magnetic Property Measurement System (MPMS) magnetometer combined with a Superconducting Quantum Interference Device (SQUID) MPMS-XL-1 allows for two types of measurements in the -1 Tesla to 1 Tesla range of magnetic fields and 1.75 – 400 K temperature range:

1. Measurements of the magnetic moment M of the sample as a function of magnetic field H at a given temperature T, i.e. measuring the $M(H)|_{T=const}$.
2. Measurements of the magnetic moment of the sample as a function of temperature at a given magnetic field H, i.e. measuring the $M(T)|_{H=const}$.

The experimental data obtained from these measurements allow, using well-known methods, to determine a range of magnetic properties of the substance, for example, magnetic characteristics of para-, dia- and feromagnetic materials, temperatures of magnetic phase transitions (T_{Curie}, T_{Neel}, etc).

The key components of the setup are shown on **Fig. 9.** The first block – reverse cryostat or "warm" insert – consists of 9 positions (1 - 9). The second block – Dewar (cryostat) (11) is set in a wooden enclosure (10). The third block is the system management unit (positions 12 - 20). The purpose of each component (position) can be understood from the figure caption.
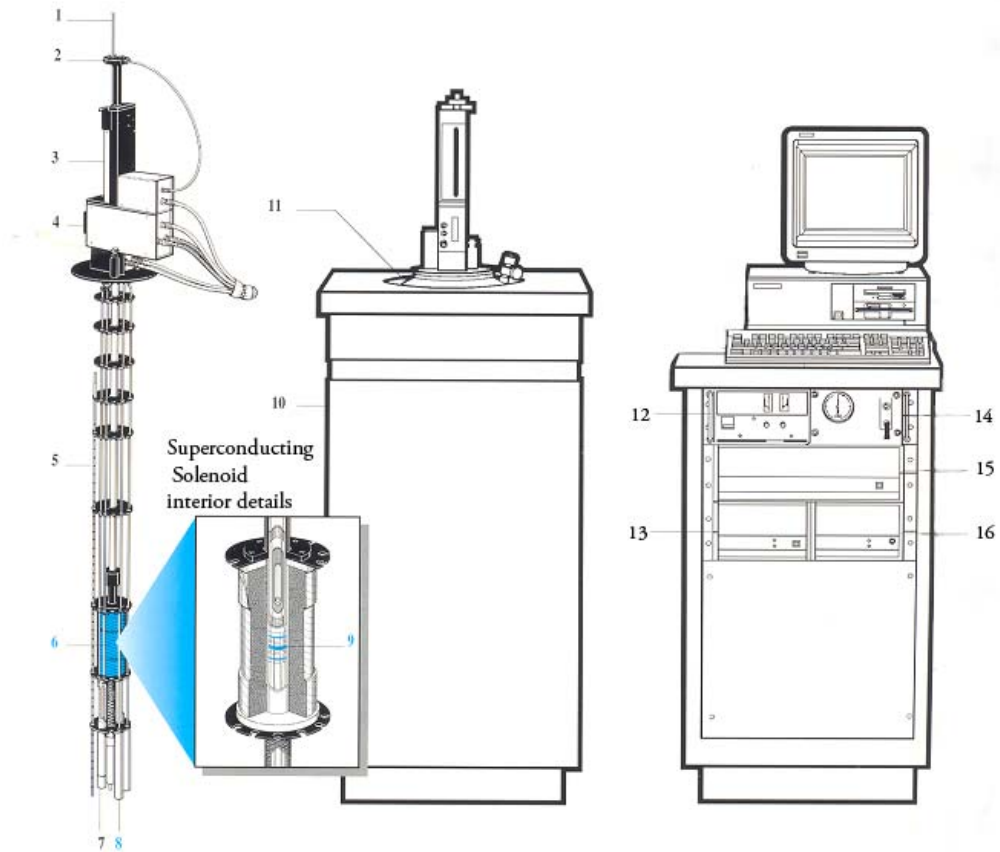
Fig. 9. The main components of MPMS-XL-1 [132].

1. Sample holder tube.

2. System of rotation of the sample.

3. Engine providing vertical movement of the sample.

4. Block of communications.

5. Transmitter determining the level of liquid helium in the cryostat.

6. Superconducting solenoid.

7. Flow controller of helium in the temperature regulation system.

8. Capsule with a SQUID transducer in a magnetic screen.

9. Superconducting detection coil.

10. Wooden enclosure for the Dewar.

11. Dewar.

12. Power supply for superconducting solenoid.

13. Temperature controller.

14. Gas flow controller.

15. Main controller.

16. Distribution node.

3.3.2. The principle of the magnetic moment measurement

The basis of measuring the magnetic moment M is a method of discharge. When the magnetic flux going through the loop changes, an electromotive force is created in the loop. Using signal integration it is easy to determine the numerical value of the magnetic flux produced by the magnetization of the sample that is removed or inserted into the loop. In dipolar approximation, the measured value is proportional to the numerical value of the projective normal of magnetic moment of the sample to the plane of the loop. In the setup, the loop consists of three cylindrical coils (**Fig. 10**) spaced at a distance of 1.5 cm and rigidly mounted on the outer tube of the reverse cryostat (**Fig. 9**, pos. 9). A superconducting wire reels up on the coils. The upper and lower coils have the same number of turns and the same direction of the contour, while the central coil that is positioned in the center of a superconducting solenoid (**Fig. 9**, pos. 6), has a double number of turns.

This scheme provides, on one hand, the suppression of the noise signal which arises when the uniform magnetic flux changes, and on another hand, is the best option for the receiver. When moving the sample along the axis of H, the resultant voltage signal in the circuit is recorded by SQUID converter (**Fig. 9**, pos. 8). The waveform of the output signal, which is proportional to the magnetic flux change, is shown in **Fig. 10b**. The sample moves upward from a point, which is chosen deliberately below the bottom of the lower coil. As the sample approaches to the coil, the magnetic flux increases and changes sign twice in the gap between the lower and middle coil. The experimental voltage curve is analyzed and compared with the ideal function in the dipolar approximation.
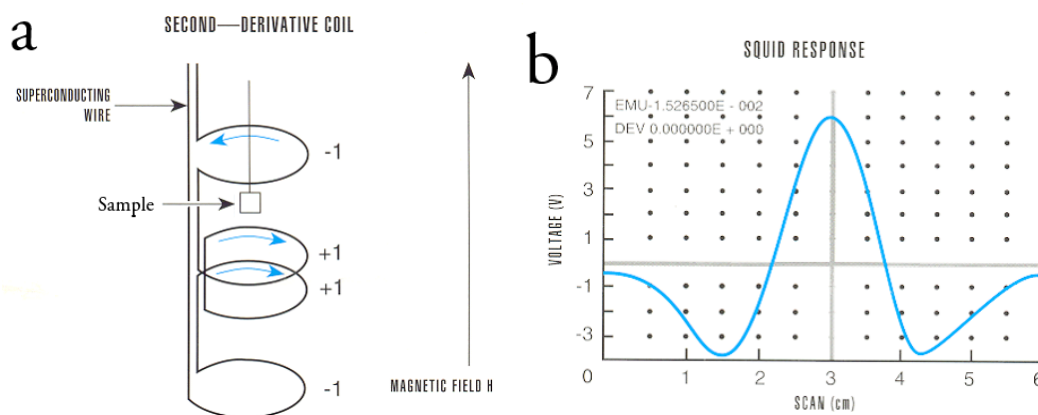

Fig. 10. The scheme of the loop (a), the output signal (b) [132].

As a result, the value of magnetic moment is computed, as well as other metrological characteristics.The CGS unit system is used. For more precise measurements, the sample goes through the coils along the specific scan length several times, and the collected data are averaged.

3.3.3. The handling of the sample

To avoid vibrations, the samples should be attached rigidly to the mounting rods. Commonly they are placed into plastic straws with a diameter of ~5 mm (**Fig. 11a**). Bulk samples of suitable size, for example, CNT film on a substrate (**Fig. 11b**), can be placed without additional fixation, but one should be aware of the straw diameter change at high and low temperatures that can cause the sample to slip. Powder microcrystalline samples, such as Mn_{12}–based SMMs, C_2F_x or nanoporous carbon, should be safely enclosed in capsules (**Fig. 11c**) to avoid spilling. It is important that the sample is immobile, so non-magnetic Kapton tape (which, in fact, gives a weak diamagnetic background) can be used for fixation if necessary.

The sample should be uniformly magnetized and small enough to determine its position accurately during scanning and centering, but not too thin, because in this case the current in the detection coil changes as the sample moves, and causes different amounts of flux in each loop of the detection coil. To ensure proper exhausting of air from the straw, we make four holes, equally spaced above and below the sample.
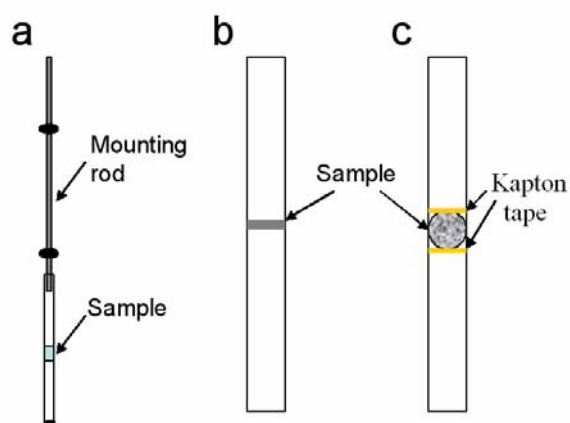

Fig.11. The sample mounted on the rod (a), bulk sample configuration (b), powder sample configuration (c)

Quite often the measured samples have low spontaneous magnetization values. Holders and fixtures should be chosen in such a way, that they do not contribute much to the signal. For this reason, gelatin capsules, which we used for molecular magnet samples at the beginning, later were rejected. Instead, we started to use thin polyethylene "bags".
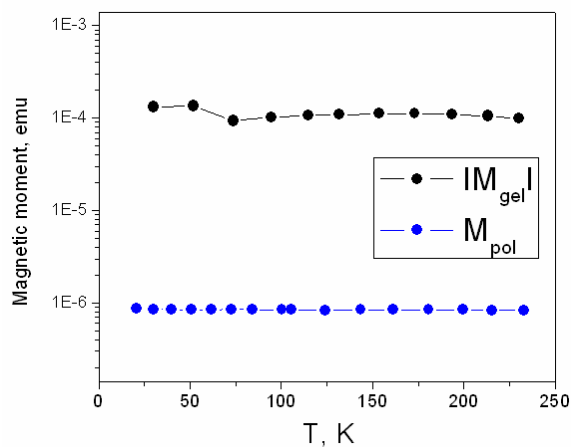
Fig. 12. The background magnetization given by a gelatin capsule, 1.11 g (black), and polyethylene "bag", 4.4 mg (blue).

The comparative study of magnetic backgrounds given by gelatin capsules and polyethylene, is shown on **Fig. 12**. Although magnetization values of both background curves were acceptably low for our samples, a gelatin capsule gives a diamagnetic signal ~100 times higher than paramagnetic background from polyethylene film.

4. Results and discussion

4.1. Iron-filled carbon nanotubes

Arrays of aligned iron-filled multi-walled CNTs were grown by A. Okotrub's group as part of a collaboration project. Investigated samples and parameters of synthesis are presented in Table 1.

Table 1. Studied samples of iron-filled CNTs.

Sample	Synth. from	Content of Fe(C$_5$H$_5$)$_2$	Technology	Weight	Weight of CNTs, est.
1	C$_7$H$_{16}$	0.5%	800^{0}C, N$_2$	23.6 mg	0.079 mg
2	C$_7$H$_{16}$	1.0%	800^{0}C, N$_2$	12.2 mg	0.054 mg
3	C$_7$H$_{16}$	1.5%	800^{0}C, N$_2$	46.1 mg	0.053 mg
4	C$_7$H$_{16}$	2.0%	800^{0}C, N$_2$	16.0 mg	0.028 mg
5	C$_7$H$_{16}$	2.5%	700^{0}C, N$_2$	19.8 mg	0.087 mg
6	C$_7$H$_{16}$	5.0%	800^{0}C, N$_2$	53.8 mg	0.242 mg

The characterization of the samples was performed by Raman spectroscopy, scanning electron microscopy (SEM) and atomic force microscopy (AFM) microscopy techniques.
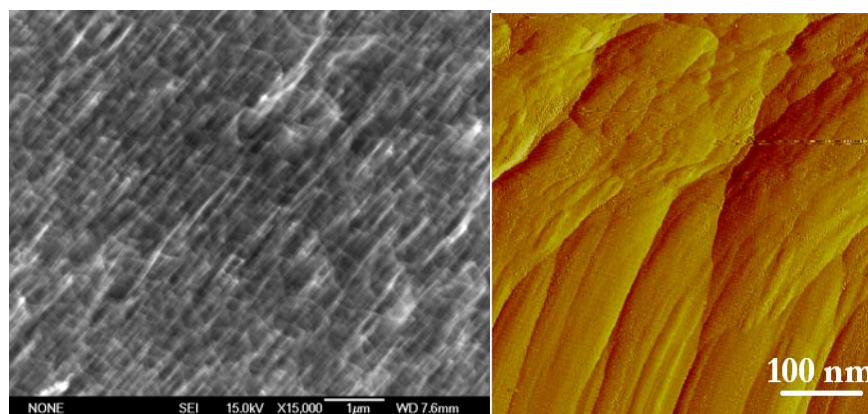

Fig. 1. SEM (left) and AFM (right) images of sample **3**.

The SEM image of sample **3** demonstrates that nanotubes grow in well-aligned tubular structures perpendicular to the substrate (**Fig. 1**). The length of the CNTs is ~10 mm. The AFM image of the same sample allows estimating the thickness of the bundles, which appeared to be in the 12–16 nm range for all samples except **6**, which showed bundles of ca. 40 nm.

Raman spectra of all samples (**Fig. 2**) show characteristic CNT peaks around 1354, 1585 and 2705 cm^{-1} corresponding to D, G and D* graphite modes, respectively, a strong peak at 520 cm^{-1} which comes from the silicon substrate, and a band around 977 cm^{-1} associated with the SiC LO mode. Furthermore, a weak band centered at ~300 cm^{-1} was observed in the spectra of samples **1** and **2**, produced from the reaction mixture with low ferrocene concentration. These low-frequency vibrations correspond to the radial breathing modes of single-walled CNTs. According to the Kataura plot, these single-walled CNTs are semiconducting with diameters ranged from 1.62 to 1.74 nm. The content of single-walled CNTs in the samples is estimated to be a few percent, the most part of the samples contain multiwall CNTs with average diameter 20 nm.
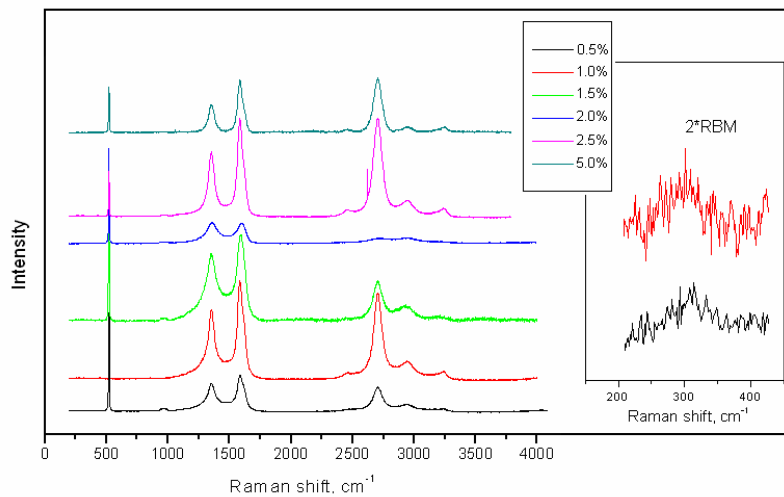
Fig. 2. Raman spectra of iron-filled CNTs.

Fig. 3 shows the dependence of the coercive force and the squareness (the ratio of remnant and saturation magnetization) of hysteresis loops on iron filling for two temperatures. The samples demonstrate magnetic anisotropy. At high ferrocene content the easy axis of magnetization is parallel to the nanotubes, as was observed previously for CNTs heavily doped with iron [22, 133], while for the sample with the lowest ferrocene content (x = 0.5%) it is parallel to the substrate. Such in-plane anisotropy is rather surprising. As an explanation we suggest that the magnetostatic interaction between iron grains on the tips of nanotubes with low ferrocene content collect them in a plate which results in the observed magnetization pattern. When the content of ferrocene is increased, magnetic wires are formed inside the nanotubes and thus, the easy axis becomes perpendicular to the substrate plane.
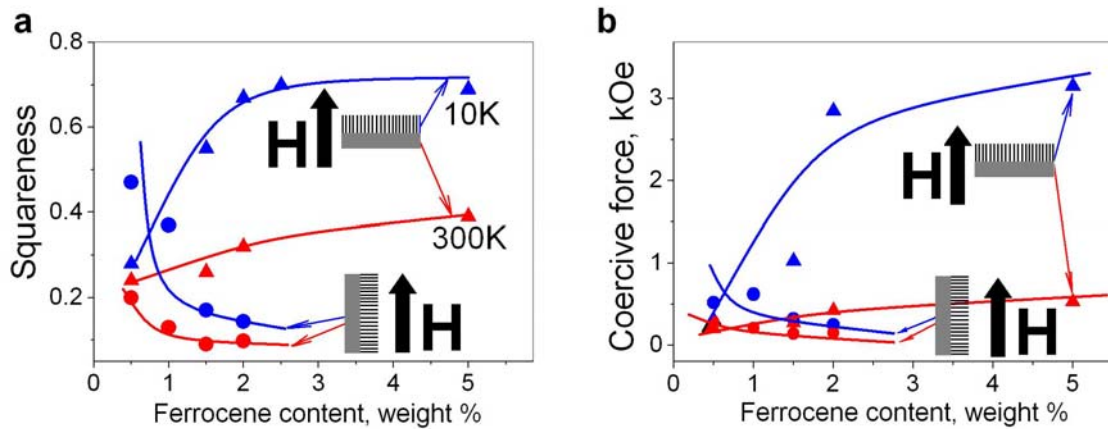
Fig. 3. Dependence of magnetostatic parameters on ferrocene content: squareness (a) and coercive force (b)

The anisotropy in magnetic behaviour shows up not only in the values of magnetostatic parameters (**Fig. 4a**), but also in the temperature dependence of the magnetization below T_c (**Fig. 4b**). We have observed a difference between T_c values for H ∥ CNT and H II substrate. Curie temperatures lie in the range 500 K (H ∥ CNT) – 700 K (H ∥ substrate), the lower value corresponding to iron carbide, Fe_3C, and the difference is slightly growing with the percentage of iron, which can be explained by formation of stronger-interacting and more magnetically stable structures inside the nanotubes.
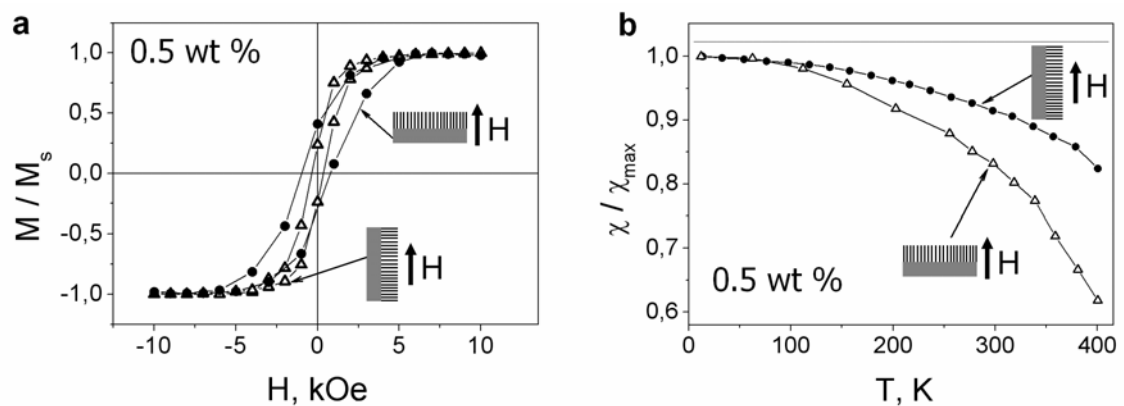

Fig. 4. The anisotropy of normalized hysteresis loops (a) and normalized magnetic susceptibilities (b) for sample **1**.

Fig. 5 demonstrates the temperature behaviour of the hysteresis curves for samples **1** and **6**. At high temperatures hysteresis loops for both samples are similar: both coercive force and squareness are small. It may be due to the influence of thermal fluctuations in small iron particles and the magnetostatic nature of the magnetic hysteresis loop – small changes in the magnetization value result in small changes in the loop shape. At low temperatures

ferrocene concentration becomes a decisive factor of magnetization, and the difference between coercive forces for the two samples increases five times. The strong temperature dependence of the magnetization curves shape in sample **6**, assumingly, results from an increase in magnetocrystalline anisotropy vs temperature in iron [134] and from an increase of thermal fluctuations with increasing temperature. The temperature dependence of the magnetostatic parameters for the samples with increasing iron content is discussed in detail below.
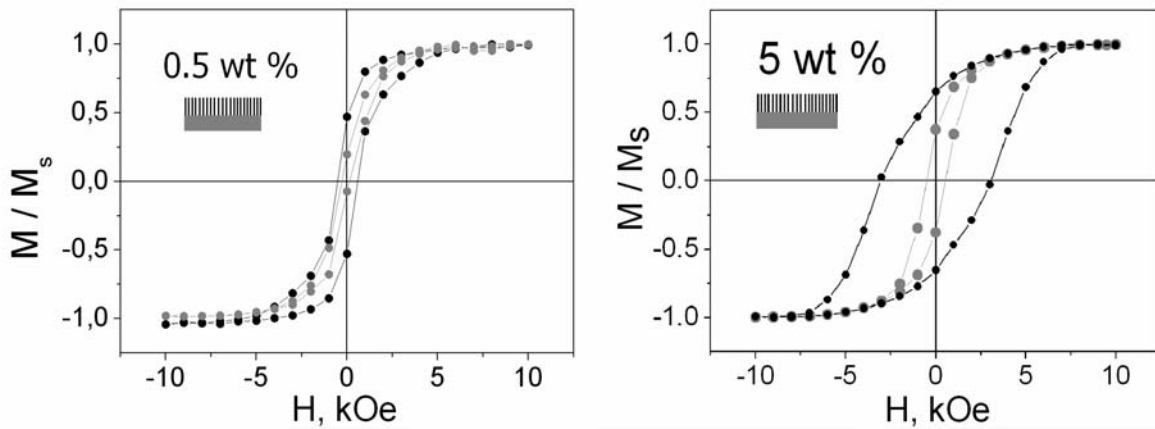
Fig. 5. Normalized hysteresis loops of samples **1** and **6** at 10 K (black symbols) and 300 K (grey symbols).

Fig. 6 shows the temperature dependence of the normalized magnetization taken at 0.1 T field applied along the nanotube axis. In agreement with the data shown in **Fig. 3**, Chapter 2.1.2, the higher the ferrocene content, the stronger the temperature gradient of the magnetostatic parameters.

Usually in smaller particles, assuming the particle size decreases with a decrease in the content of iron, magnetism is easier destroyed by thermal fluctuations. Here the situation is different, and the temperature gradient is higher in samples with a higher concentration of ferrocene. This result can be explained by the finite size effect, as the spin-wave spectrum of clusters differs from that of bulk material; it is found to have cluster size-dependent energy gaps, resulting in slower relaxation of magnetization at temperatures when only a few lower states are populated and ΔE is important [135]. Related effects have been observed experimentally in Fe_3C nanoparticles inside carbon nanotubes [136].
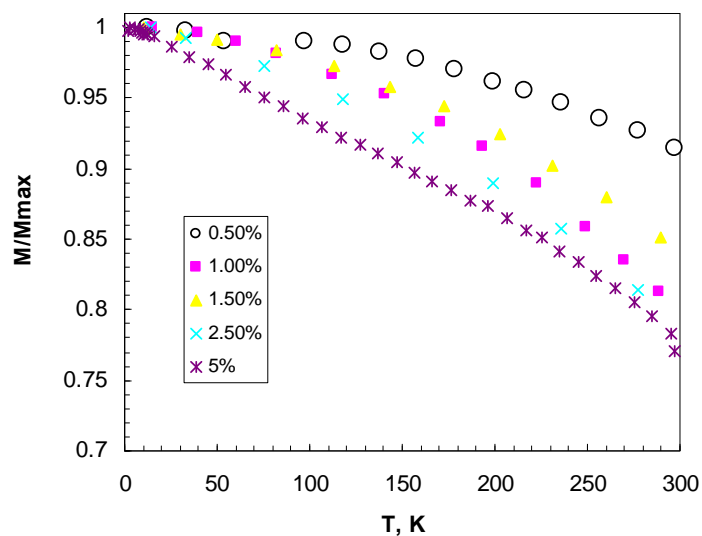
Fig. 6. Normalized magnetization plotted vs. T for samples with different ferrocene content. Data were taken at 0.1 T magnetic field.

To conclude, the magnetic behaviour of CNTs with low filling of iron was measured, and influence factors were studied. It was shown that the magnetization process in weakly doped CNTs differs from what is typical for heavily doped CNTs because it is more affected by quantum effects.

4.2. Mn$_{12}$-based single molecular magnets

4.2.1. Mn$_{12}$-based single molecular magnets with benzene, pentafluorobenzene, and 4-cyanobenzene carboxylate ligands

Samples of Mn$_{12}$-based SMMs with various oxocarboxylate ligands were synthesized by the group of E. Yagubskii as part of a collaboration project. All manipulations were carried out under aerobic conditions at room temperature using commercial grade chemicals and solvents. The reaction products (Table 2) were characterized by elemental analysis and Raman spectroscopy.

In **Fig. 7** spectra of samples **1-3** are shown in comparison. In the spectrum of sample **1** modes at 530 cm^{-1}, 597 cm^{-1}, 650 cm^{-1}, 692 cm^{-1} assigned to Mn-O vibrations [137], and the broad peak around 1420 cm^{-1} assigned to Mn-acetate stretching mode are well resolved, while in samples **2** and **3** modes which are associated with vibrations of the magnetic core of the molecule are supressed.

Table 2. Studied Mn_{12}-based SMMs

Sample	Formula	Solvent	
1	$[Mn_{12}O_{12}(C_6F_5COO)_{16}(H_2O)_4]$	$C_6H_5CH_3/$ C_6H_{14}	
2	$[Mn_{12}O_{12}(O_2CC_6H_4\text{-}p\text{-}CN)_{16}(H_2O)_4]$	$CH_2Cl_2/$ $(C_2H_5)_2O$	
3	$[Mn_{12}O_{12}(C_6H_5COO)_{16}(H_2O)_4]$	$CH_2Cl_2/$ C_6H_{14}	
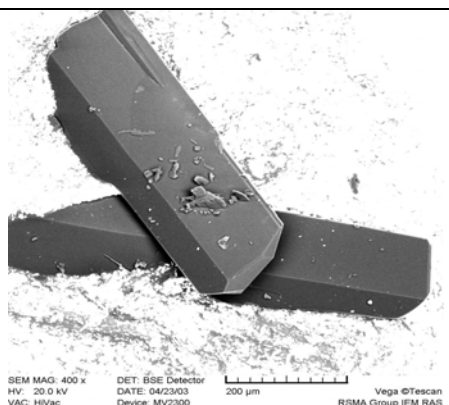
Instead, these samples demonstrate enhanced modes of carboxyl ligands: the bands around 1606 cm^{-1}, 2228 cm^{-1} and 3075 cm^{-1} are assigned to the vibrations of carboxylate $(OCO)_{asym}$, $C\equiv N$ and OH (coordinated H_2O) groups [138-139], respectively, which points out the different arrangements of bound H_2O and carboxylic ligands for these structures, and allows to suppose different magnetic properties.
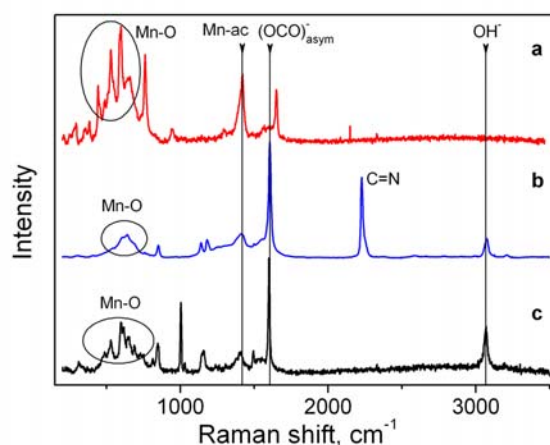

Fig. 7. The Raman spectra of samples **1** (a), **2** (b), **3** (c).

Fig. 8 presents a comparison of magnetization data for complexes **1-3**. Zero-field-cooled (ZFC) and subsequent field-cooled (FC) measurements were performed at the same applied field of 0.01 T. The sample was first cooled under zero magnetic field, and the field was applied at the lowest temperature (1.75 K), then ZFC magnetic moment shown by open symbols was measured with increasing temperature up to 300 K. After this the FC magnetic moment shown by red symbols was measured under the same conditions with decreasing temperature. We note that the FC and ZFC curves of sample **1** show magnetic behavior typical for Mn_{12}-based SMM complexes, and the blocking temperature T_B is ~3K.
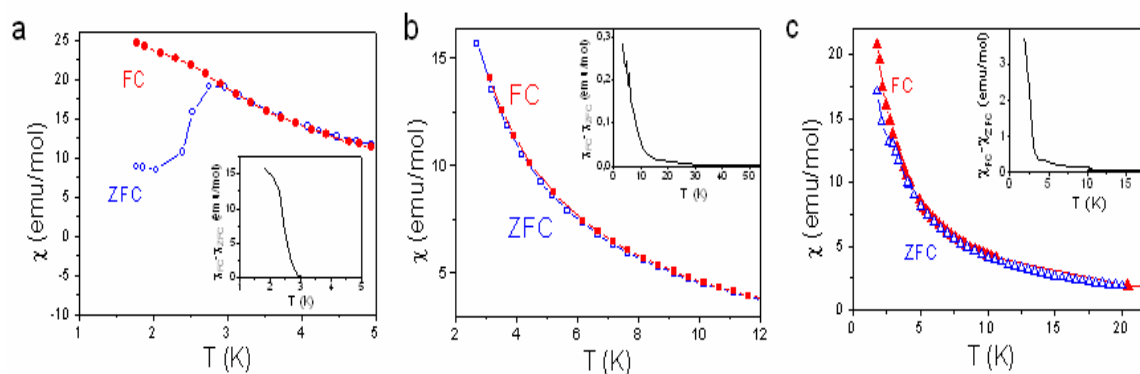
Fig. 8. The FC and ZFC magnetization curves for complex **1** (a), **2** (b), **3** (c); the insets show the corresponding residuals between FC and ZFC curves.

ZFC curves for complexes **2** and **3** are abnormally shaped and stay split well above what is usual for Mn_{12} $T_B \sim 3.5$ K, indicating that the magnetic anisotropy of these samples significantly differs from previously studied Mn_{12}-based SMMs. The insets show the corresponding residuals between FC and ZFC curves. It is clearly observed that there is a measurable difference between the curves at least at 25 K for complex **2** and 15 K for complex **3**. In the latter case, there is a peculiarity around 3 K, and the shape of the curve suggests a large number of fast-relaxing species.
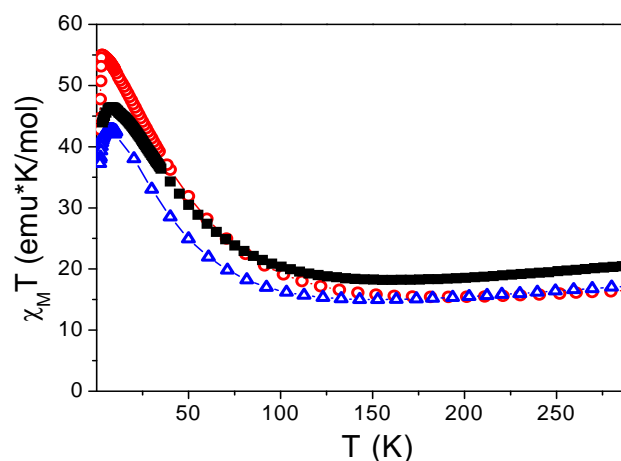

Fig. 9. Temperature dependences of $\chi_M T$ for complexes **1** (circles), **2** (squares), and **3** (triangles).

A similar sudden sharp increase in T_B for Mn_{12}-acetate was discovered earlier in [40] and was tentatively assigned to the molecular electronic shell modification due to the specific treatment, as Mn_{12} molecules are known to be highly sensitive to the environment [140].

The dc magnetic susceptibility data of all complexes measured in a 0.1 T field and 1.75 – 300 K temperature range are shown on **Fig. 9.** The curves of complexes **2** and **3** are very similar: on decreasing temperature curves go through broad minima indicating ferrimagnetic ordering, and then the $\chi_M T$ values slowly increase to maxima of 46.4 (μ_{eff} = 19.3) and 42.8 (μ_{eff} = 18.5) emu·K·mol^{-1} at 8 and 9 K, respectively, and afterwards decrease at lower temperatures due to Zeeman effects from the applied field or intercluster interactions. For sample **1** the minimum is not so prominent, and the maximum corresponds to an effective moment μ_{eff} = 21, which is consistent with the theoretical spin-only value for S=10.

The hysteresis loops of all complexes with diamagnetic background removed, taken at various temperatures, are presented on **Fig. 10**. These data confirm the observation obtained from the FC-ZFC curves. The preserved nonlinearity for complexes **2** and **3** is clearly seen up to 10 K, while for complex **1** the loop disappears at 3 K. Neither of investigated complexes displays "steps" coming from quantum transitions, though the derivatives dM/dH allow to distinguish quantum transitions in complexes **2** and **3** (see insets **Fig. 10b, c**). In complex **1** quantum transitions are totally absent, and the hysteresis loop is butterfly-shaped, indicating efficient quantum tunneling.
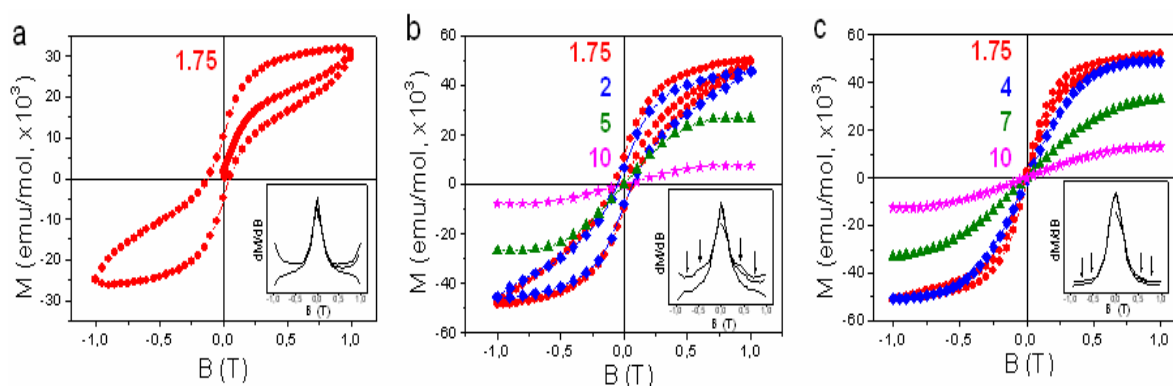

Fig. 10. Hysteresis loops of complexes **1** (a), **2** (b), and **3** (c); the insets show the corresponding derivatives.

The order of magnitude for axial zero-field splitting D can be estimated from the first derivatives of hysteresis loops: D = - $\Delta H*g/2$, where ΔH is a mean value of the "step", and g-factor is estimated from **Fig. 9** as $\mu_{eff}/(S^2 - S)^{1/2}$. Calculated values are D = -0.33 cm^{-1} for complex **2** and D = -0.38 cm^{-1} for complex **3**.

Moreover, in complex **2** the values of magnetostatic parameters such as remnant magnetization and coercive force are non-zero well above the usual blocking temperature of 3 K (**Fig. 11**).
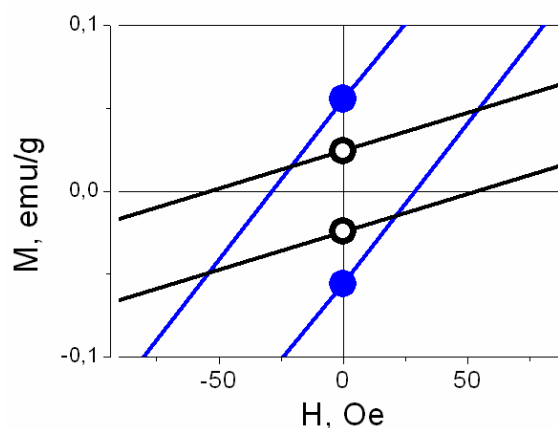

Fig. 11. Zoomed central part of the loops complex **2**, taken at 5 K (blue) and 10 K (black).

At the temperature of 10 K the loops still show an opening, and to our knowledge, the largest reported hysteresis loop opening temperature reported to date for an SMM is 7 K [34]. Thus, we observe two interrelated phenomena: suppression of the quantum transition and loop opening at temperatures sufficiently higher than the characteristic blocking temperature for M_{12}-based SMM. Recent experiments have demonstrated [141] that the dipolar interactions between molecular spins are likely to determine the quantum tunneling processes in SMMs and thus, the magnetic relaxation rate. We assume that the unusual magnetic behaviour of **2** is caused by strong dipole-dipole interactions between the clusters. To summarize, we have studied the influence of ligand substitution on magnetic properties of Mn_{12}-based SMMs and have shown that it is possible to control the magnetic behavior of a SMM by varying the structure of ligands. In the cases of benzene and 4-cyanobenzene derivatives, an increased blocking temperature is observed. The nonlinear field dependence of magnetization in these compounds is preserved up to 10 K. The most interesting of the studied clusters is **2**, which demonstrated bifurcation of temperature dependencies of magnetization taken under the zero field cooled and field cooled conditions, as well as nonzero remnant magnetization and coercive force up to 10 K. Unlike the known Mn_{12} oxocarboxylate clusters, the complex **2** is not dissolved in organic solvents providing an indication for strong intermolecular interactions, which can lead to strong dipole-dipole interactions between clusters.

4.2.2. Mn$_{12}$-based single molecular magnet with 4-cyanobenzene carboxylate ligands and its derivatives

One-electron and two-electron reduced derivatives were prepared for sample **2**, as its tetraphenylphosphonium salts: (PPh$_4$)[Mn$_{12}$O$_{12}$(O$_2$CC$_6$H$_4$-*p*-CN)$_{16}$(H$_2$O)$_4$] (sample **2'**) and (PPh$_4$)$_2$[Mn$_{12}$O$_{12}$(O$_2$CC$_6$H$_4$-*p*-CN)$_{16}$(H$_2$O)$_4$] (sample **2''**). The obtained complexes were characterized by elemental analysis, Raman and IR spectroscopy. The Raman spectra are presented on **Fig. 12**.
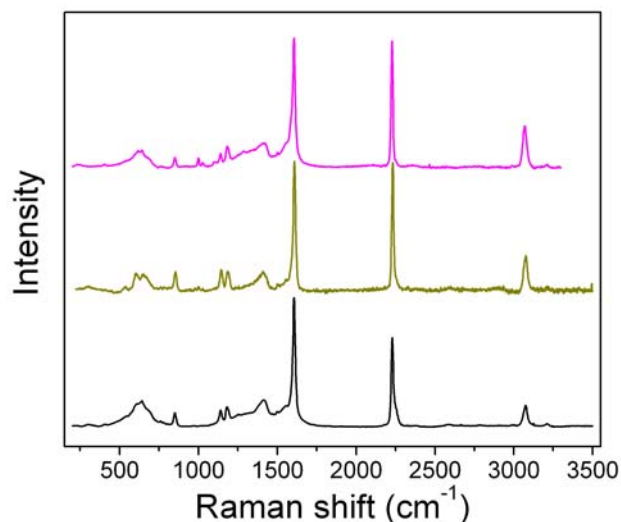

Fig. 12. The Raman spectra of complexes **2** (black), **2'** (yellow), and **2''** (pink).

The broad band composed of several peaks (542, 607, 643 cm^{-1}) that is observed in the lower frequency region is assigned to Mn-O vibrations. The bands around 1606 cm^{-1}, 2228 cm^{-1} and 3075 cm^{-1} are assigned to the vibrations of carboxylate (COO), C≡N and OH (coordinated H$_2$O) groups, respectively. The strong band of the C≡N stretching vibration at 2245 cm^{-1} is observed in IR spectra.

We conducted a comparative study of magnetic properties of the initial magnet described above (**2**) and its singly (**2'**) and doubly (**2''**) reduced derivatives. In **Fig. 13**, dc susceptibility data are plotted as a function of the temperature for these three studied complexes.
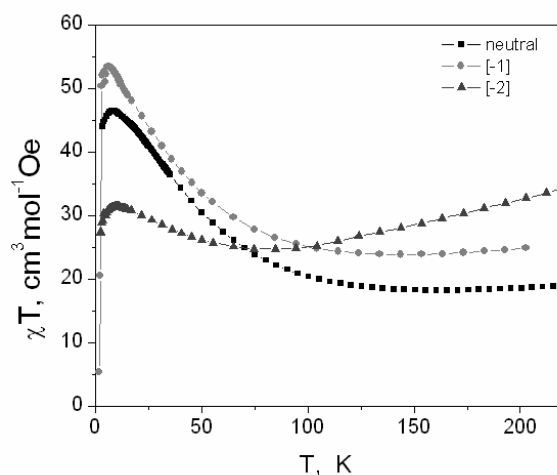
Fig. 13. The comparison of $\chi_M T$ versus temperature plots of complexes **2**, **2'** and **2''**.

The data for the one-electron reduced complex **2'** show a similar temperature dependence as for the neutral one; the measured effective magnetic moment is higher in the one-electron reduced complex which is, presumably, caused by a stronger anisotropy constant. The maximum of $\chi_M T$ curve for the one-electron reduced complex is equal to 53.5 cm³mol⁻¹K, which is consistent with S = 19/2 if the g-factor equals 2.07. For the two-electron reduced version, the value of the maximum $\chi_M T$ corresponds to an effective moment μ_{eff} = 15.3 μ_B, a spin ground state S = 8 and g = 1.81. The data for the neutral and one-electron reduced complexes **2** and **2'** show similar temperature dependences, while sample **2''** demonstrates a prominent minimum at around 70 K, indicating strong antiferromagnetic interaction. A similar dependence for two-electron reduced Mn₁₂ SMM was observed earlier in [142]. The bifurcation point for both **2'** and **2''** complexes is ~3K.

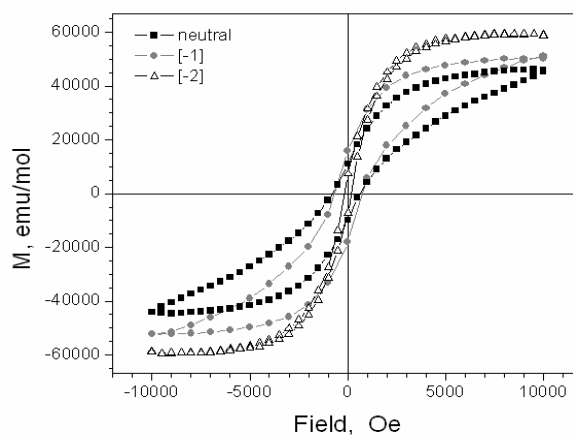**Fig. 14.** The hysteresis loops of complexes 2, 2', and 2", measured at 1.75 K.

Fig. 14 shows a comparison of the hysteresis loops for complexes **2**, **2'**, and **2''**. The magnetostatic parameters (Table 3) are very similar for the neutral and one-electron reduced complexes, although the remnant magnetization is higher in **2'**, and the form of the loop suggests that saturation is reached at lower magnetic fields for electron reduced complexes. The saturation value of the magnetization progressively increases with each reduction step while the loop itself becomes "thinner".

Table 3. Magnetostatic parameters for Mn_{12}-based SMMs **2**, **2'**, and **2''**.

Complex / Parameter	Neutral (**2**)	Electron-reduced (**2'**)	Two electron-reduced (**2'**)
Coercive force, H_c	712	713	175
$M_{remnant}/M_{saturation}$	0.25	0.32	0.12

From the first derivatives of the hysteresis loops we estimated the order of magnitude for the axial zero-field splitting D. The spacing between the "steps" on hysteresis loops is given by $\Delta H = -D/\mu_B g$, where the average value of the "step" for one-electron reduced complex **2'** is 0.4 T, and the g-factor values are estimated from dc magnetization plots. The calculated value of D for complex **2'** is -0.42 cm^{-1}. The latter value is surprisingly high – in the neutral complex D = -0.33. In the reduced complex, we would expect decreasing of D by ~25% for each reduction step for Mn_{12}-acetate analogues [143]. The upper limit for the anisotropy energy barrier height scales as $(S^2- ¼)|D|$ for half-integer spins, which gives 53.7 K for complex **2** which is typical for one-electron reduced Mn_{12} complexes [144-145].

To conclude, one-electron and two-electron reduced clusters (**2'**, **2''**) of sample **2** are dissolved in organic solvents providing an indication for weaker intermolecular interactions, which can lead to weaker dipole-dipole interactions between clusters. They show magnetic properties characteristic for anion Mn_{12} clusters. The difference in magnetic behaviour between the **2**, on one hand, and **2'** and **2''**, on another hand, can be accounted for by taking into consideration the different strengths of dipolar interactions in the crystal lattices.

4.2.3. Fullerene-diluted single molecular magnets

Complexes **1** and **3** were chosen for further investigation, and fullerene-containing species **1a** and **3a** were obtained for them. The $Mn_{12}:C_{60}$ ratio for samples **1a** and **3a** is approx. 1:1.

The cocrystallized Mn_{12}:C_{60} compounds were characterized by elemental analysis, X-ray diffraction, and Raman spectroscopy.

In **Fig. 16** spectra of the **1a** and **3a** samples are shown in comparison with their non fullerene-containing species. In both non-fullerene spectra modes at 530 cm^{-1}, 597 cm^{-1}, 650 cm^{-1}, and 692 cm^{-1} assigned to Mn-O are well resolved. The peaks at 1402 cm^{-1} are due to the extensional mode of the carboxilate (COO) ligand. In fullerene-containing species the modes of Mn are inhibited. In fact, we observe clean fullerene spectra in both cases. In **1a** spectrum fullerene modes are shifted -11–-24 cm^{-1} to the range of low frequencies, indicating a strong charge transfer between clusters of Mn_{12} and C_{60}.
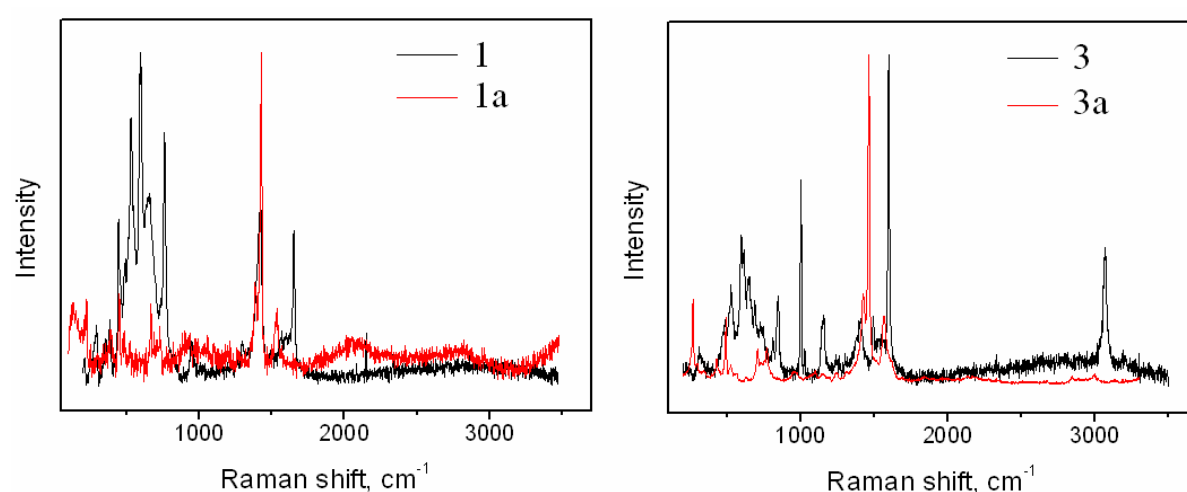

Fig. 16. The Raman spectra of complexes **1**, **1a**, **3** and **3a**.

The degree of crystalline order in the samples was studied by x-ray diffraction. The diffraction patterns show that characteristic peaks of samples **1a** and **3a** (black arrows in **Fig. 18**) coincide with those for the triclinic crystalline phase of this compound [146]. By contrast, diffraction peaks at 2Θ = 10.83; 17.77; 20.91 corresponding to the (111), (220) and (311) reflections from pristine C_{60} are absent (green arrows in **Fig. 18**) demonstrating that fullerene does not form its own crystal lattice being mixed with the Mn_{12} at the molecular level. For both complexes **1a** and **3a**, in the range between 15 and 30 degrees a strong halo appears which is characteristic of isotropic and uncorrelated orientations of the C_{60} molecules.
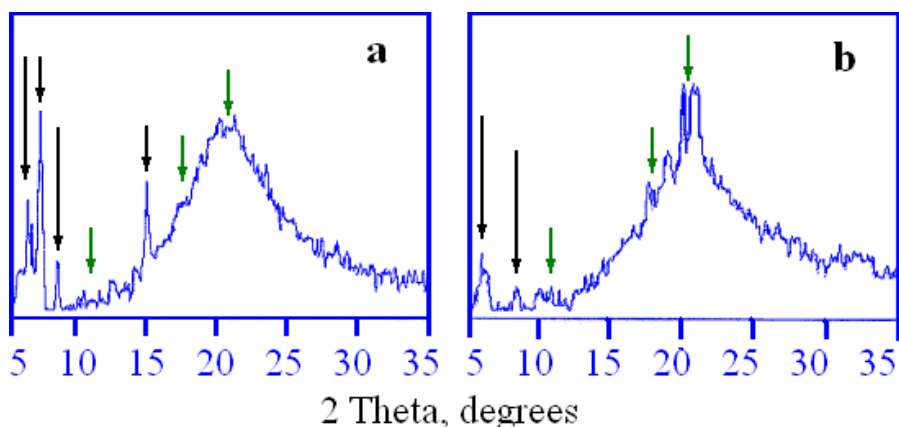
Fig. 18. The XRD patterns of complexes **3a** (a) and **1a** (b). The positions of reflections coming from Mn_{12} are shown by black arrows, from pristine fullerene – by green arrows

Complexes **1a** and **3a** exhibited an unusual behavior in the magnetic field. **Fig. 19** shows dc magnetic susceptibility data for all complexes measured in a 0.1 T field and in the 1.75 - 300K temperature range. For non-fullerene species **1a** and **3a** $\chi_M T$ values increase to maxima of 42.8 and 55 emu*mol^{-1}*K at 9 and 3 K, respectively, and afterwards decrease at lower temperatures due to Zeeman effects from the applied field or intercluster interactions. For sample **3** the maximum is broader suggesting a broad distribution of energy barriers. In C_{60}-diluted compounds $\chi_M T$ maxima lie at 7.5 K and are equal to 13 and 8.7 emu^3*mol^{-1}*K for complexes **1a** and **3a**, respectively, indicating that the spin concentration decreased 5-8 times.
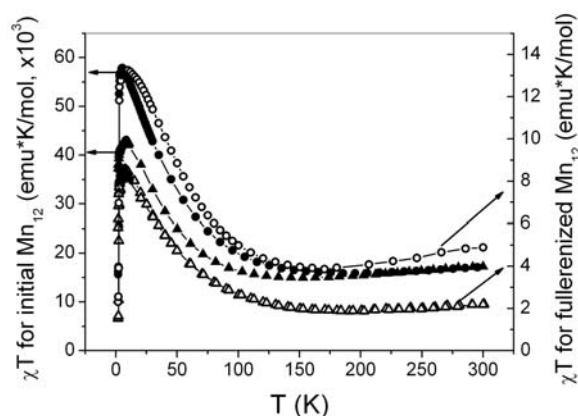

Fig. 19. Temperature dependences of $\chi_M T$ for complexes **1** (solid circles), **3** (solid triangles), **1a** (open circles), and **3a** (open triangles)

A comparison of magnetization values plotted vs magnetic field for all samples is presented in **Fig. 20, a-b**. To clarify the positions of quantum transitions, plots of dM/dH vs. H are shown in **Fig. 21**.
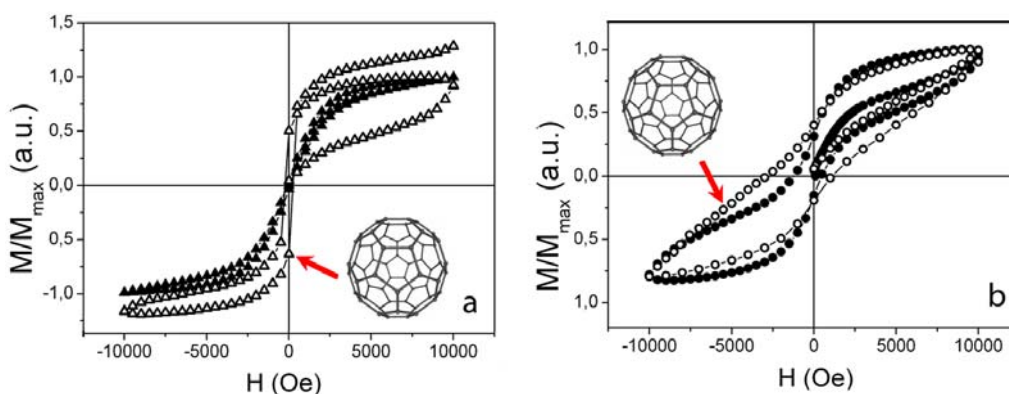
Fig. 20. Normalized hysteresis loops for complexes **1** (solid circles), **3** (solid triangles), **1a** (open circles), and **3a** (open triangles) taken at 1.75 K.

As was discussed above, quantum transitions in non fullerene-containing species are suppressed. Adding fullerenes reduces spin concentration, and at the same time restores both quantum transitions around 0.4 T and 0.8 T, typical for Mn_{12}–based complexes. Magnetization values at 1 T correspond to 6 μ_B /molecule for **1** and 10 μ_B /molecule for **3.** Complexation with fullerenes reduces these values to 1.2 μ_B /molecule for both complexes. Moreover, in both fullerene-containing complexes the magnetostatic parameters (coercive force and squareness of hysteresis) increased ca. 3 times, proving that the behavior of the exchange parameters has changed.
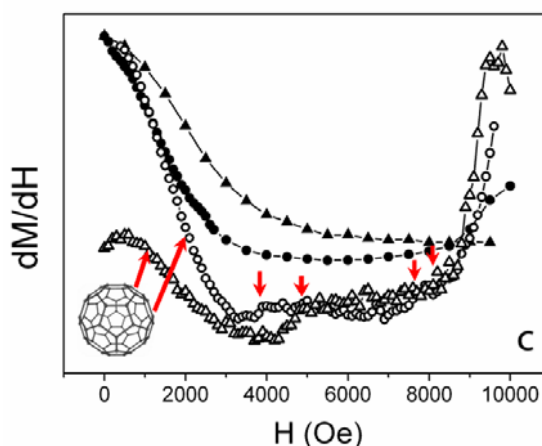

Fig. 21. Normalized derivatives of the virgin curves for complexes **1** (solid circles), **3** (solid triangles), **1a** (open circles), and **3a** (open triangles) Arrows show the quantum transitions. T = 1.75 K.

Dilution of Mn_{12} SMMs with fullerenes significantly influenced the magnetization process. As shown on **Fig. 22a**, for complex **3a** the hysteresis curve does not reach saturation in a field of 1T and progressively increases its amplitude with every 1T – -1T – 1T iteration. This process is better seen on the time dependence of magnetization (**Fig. 22b**). The

absolute values of both maxima and minima on the M (t) curves notably increase in time. Differentiation of this curve reveals another peculiarity of the process: sharp spikes related to the quantum transitions (marked by arrows in **Fig. 22c**) become lower. This indicated that the quantum transitions become more suppressed with each cycle. Were the effect due to an unusually slow relaxation of the magnetization in fullerene-SMM complexes, one would expect that keeping in a high magnetic field will lead to an increase of magnetostatic parameters.

To check this hypothesis, we kept the sample **3a** in the positive magnetic field without cycling. After the sample had been stored in a magnetic field 1 T for 8 hours the curve finally saturated, and further keeping in a magnetic field did not increase the magnetization. In the next cycle, one would expect to reach the same saturated value in the negative magnetic field. The whole curve becomes asymmetrically shifted on the y-axis. The repeated measurements cause another type of relaxation: the curve "remembers" the amplitude and gradually regains symmetry (see **Fig. 23**, lower curve).
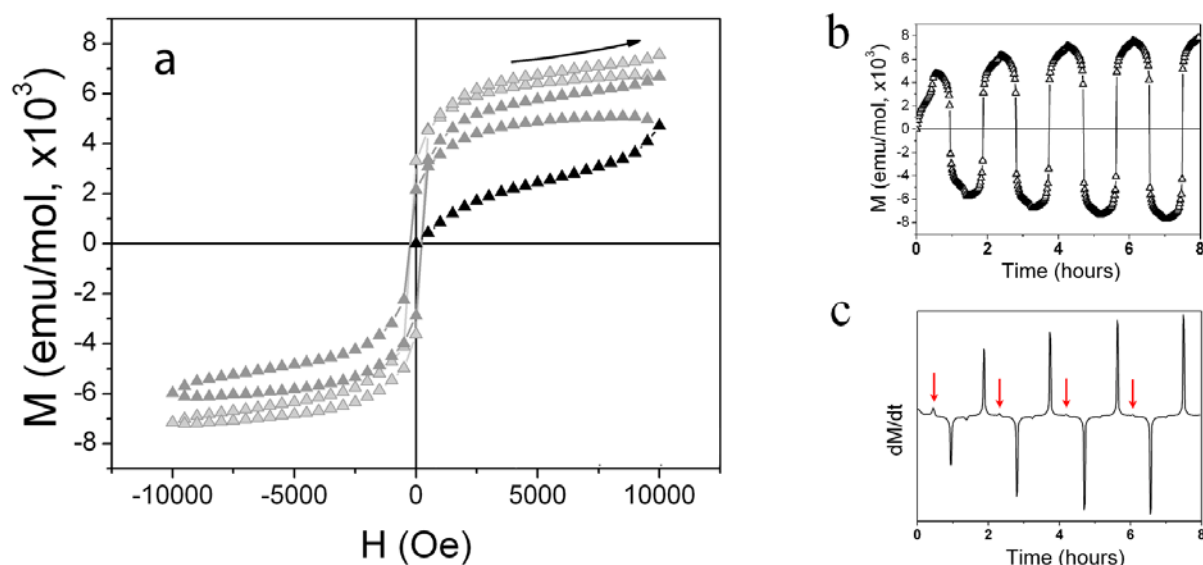

Fig. 22. The successive hysteresis curves for complex **3a** (a); time dependence of magnetization – "magnetization training" effect (b); derivative of time dependence with marked quantum transitions (c).

The molecule exhibits such strong residual magnetization that the value of magnetization in negative fields to just over half that in positive fields.
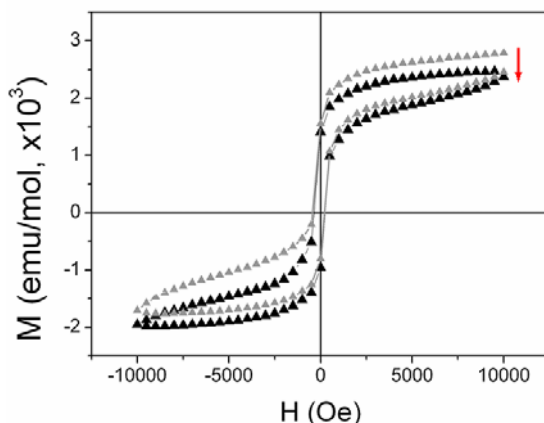
50

Fig. 23. Shifted hysteresis curve of complex **3a** after 8-hour storage in magnetic field and its relaxation to the symmetrical state.

This effect has been observed for both fullerene-containing species (**Fig. 24**) but was absent in the samples without fullerenes. The effect is absolutely reproducible and is preserved up to 3 K, which is the blocking temperature for Mn_{12}-based SMMs.
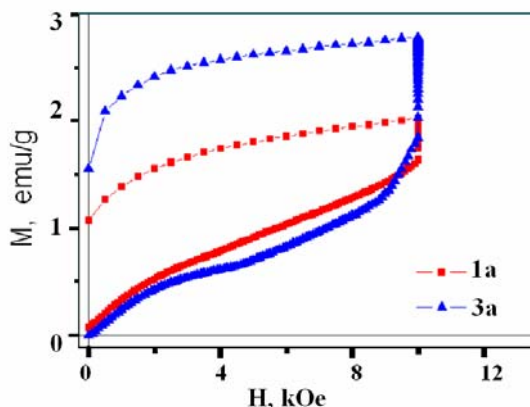

Fig. 24. The "magnetization training" effect for complexes **1a** and **3a**. Complex **1a** had been stored in 1 T field for 2 hours.

As the slow relaxation of the magnetization is not the reason, or at least not the only reason for the observed training of magnetization, we suppose that the formation of $Mn_{12}:C_{60}$ complexes leads to orientational control of magnetism, as fullerenes are known to have a coupling between spin and molecular orientational order/disorder: since the overlapping of molecular orbitals define the intermolecular exchange interaction and the orbitals are attached to molecular frames, space ordering of the molecules will result in ordering of spins. A similar mechanism has been observed and theoretically justified for other fullerene-containing molecular solids [12-13, 147-148]. As shown by the authors of [149], at low temperatures such a system is capable to "remember" its magnetization.

We believe that fullerene molecules form a subsystem and push the molecules of Mn_{12} apart, thus reducing spin concentration. Apparently, under the influence of applied cyclic magnetic field the system is self-organizing, and the fullerene molecules rotate relative to each other, coming to an optimal configuration, which is accompanied by a gradual increase in the magnetic moment.

To conclude, we have studied the magnetic properties of new Mn_{12}-based SMMs complexated with fullerenes. The addition of fullerene molecules to well-known compounds caused impressive changes in magnetization dynamics: the "magnetization training" effect and the consequent shift of asymmetrical hysteresis loop along the magnetization axis while the properties of SMM are preserved. These effects are explained by an orientational dependence of magnetism in C_{60}-doped organic substances.

4.3. Oxygen-eroded nanoporous graphite

Nanoporous boron-doped graphite was produced by A. Mombru group, as described in [14]. The investigated samples, parameters of synthesis and impurity analysis data are presented in Table 4.

Table 4. Studied NPC samples

Sample	Oxidizing agent	Chamber type	B, w.ppm	Fe, w.ppm	
NPC1	CuO	Semi-sealed	260	245	
NPC-31-2	CuO	Sealed	570	255	
NPC-32-2	CuO	Semi-sealed	-	23	
NPC-10-8	CuO	Sealed	3300	81	
NPC-56	Al_2O_3	Semi-sealed	1230	1490	
NPC-57	Al_2O_3	Semi-sealed	43000	86.8	
NPC-58	Al_2O_3, Cu	Semi-sealed	-	5640	

100 nm
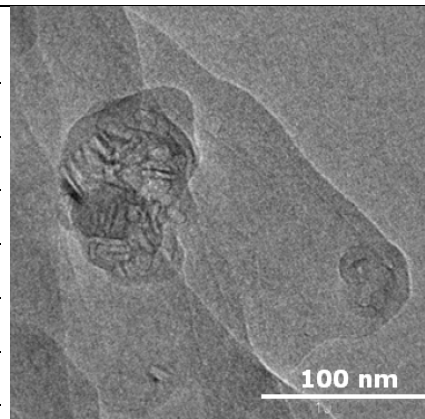
The samples were characterized by Raman spectroscopy. **Fig. 25** presents the Raman spectra for samples with boron content 0–4.30 wt %. Carbon nanofoams can be described as highly aligned graphitic structures around pores of various sizes, i. e. a mixture of highly aligned and poorly aligned structures, which correspond to ideal and turbostratic graphite.

The nanoporous sample, which was synthesized without boron, has a typical spectrum of a disordered graphitic structure with noticeable defect-induced D and D' modes at around 1353 cm^{-1} and 1620 cm^{-1}, respectively.

If boron is added to the starting material, the resulting boron-doped samples demonstrate a gradually increasing crystallinity up to a certain level of doping. At high boron concentrations this trend reverses, and the NPC collapses back to a highly-defective structure. The ratio I(D)/I(G) is quickly decreasing from 19.6 to 2.18, as the boron content increases, which means that the in-plane crystallite size (and degree of order) increases [122], while for the sample with the highest boron content there is a significant decrease in crystallite size.
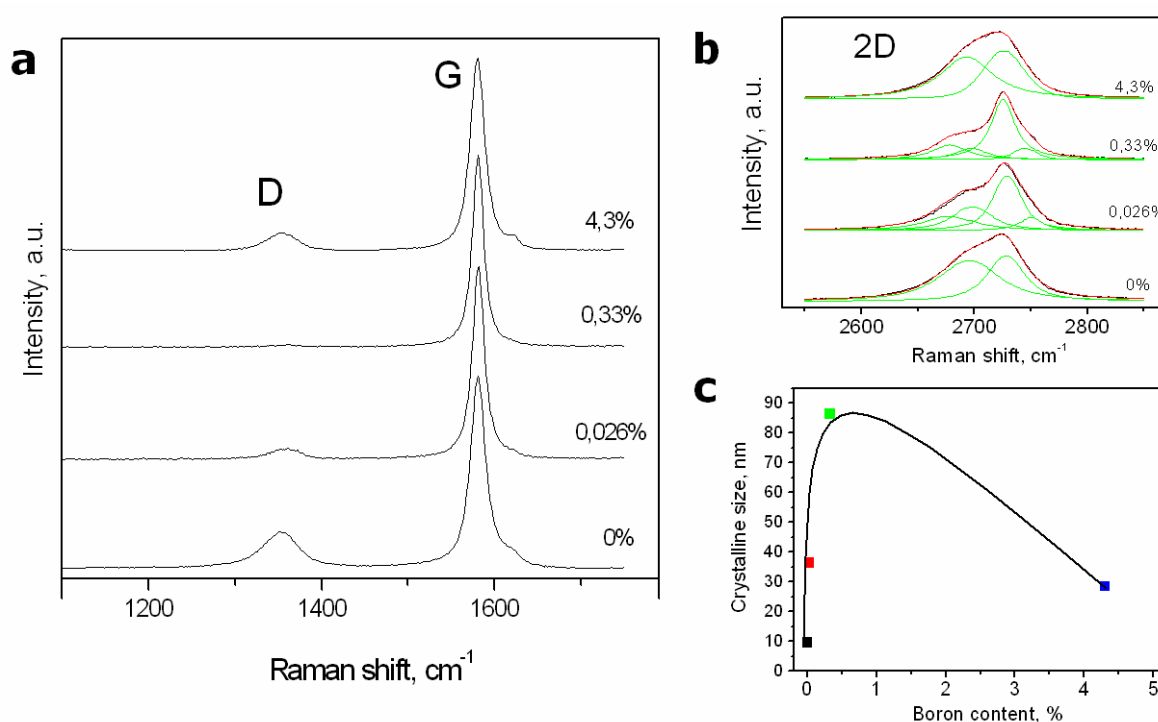

Fig. 25. The first order Raman spectra of samples with 0 – 4.3 wt % boron content (a); zoom of 2D Raman mode of samples with 0 – 4.3 wt % boron content (b); the dependence of crystalline size on boron content (c).

The crystallite size of nanographites was determined using both the D/G ratio and the G FWHM which gave similar results. The crystallite size in our NPCs varies in the 10-90 nm range, and the estimated values for the studied samples are shown at the corresponding spectra in **Fig. 25c**.

In the second-order Raman spectra of the samples with no boron and with the highest boron content, the 2D peak is double (**Fig. 25b**). In other studied boron-doped samples it is triple, formed by the contributions of highly aligned (around 2678 cm^{-1} and 2725 cm^{-1}) and poorly

aligned (2697 cm^{-1}) areas. The I_{turbo}/I_{ideal} ratio decreases from 40% in the sample with B=0.12 wt % to 18% in the sample with B=0.33 wt %.

An additional band at around 2745 cm^{-1} observed in the samples with an intermediate level of boron doping indicates the presence of multi-shell graphitic nanoparticles.

DC magnetic measurements confirmed that for samples with contamination of transition metal impurities, boron plays a crucial part in NPC magnetism.

The total magnetic moment of the studied NPC samples can be viewed as the sum of several components: atomic core diamagnetism, orbital diamagnetism coming from itinerant π-electrons in the band structure of a semimetal, van Vleck paramagnetism originating from virtual magnetic dipole transitions between the valence and conduction bands, a ferromagnetic term from magnetic impurities, Landau diamagnetic and Pauli paramagnetic contributions from conduction electrons, and a temperature-dependent Curie–Weiss term $C/(T-\Theta)$, where C and Θ stand for the Curie constant and the Weiss temperature, respectively:

$$\chi_{total} = \chi_{core} + \chi_{orb} + \chi_{VV} + \chi_{ferro} + \chi_{Land} + \chi_{Pauli} + \chi_{CW} \quad (1)$$
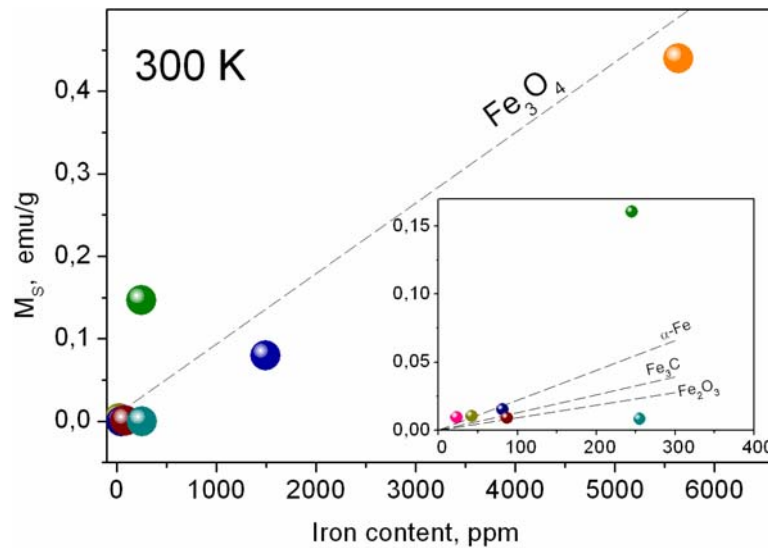
Fig. 26. The dependence of room-temperature magnetization values on iron impurity content. Dashed lines correspond to the expected magnetization values for Fe-containing samples.

As shown on **Fig. 26**, transition metal impurities start to determine the magnetic behaviour of the samples by their contribution to χ_{ferro}, only when their concentration is high enough. Iron clusters and NPC co-exist in the sense that iron does not affect the electronic system of the host structure.

In contrast, boron, which embeds in the lattice of graphite, modifies its electronic structure, and thus, the magnetic properties. Our measurements revealed that boron affects the magnetic behaviour of host NPC structure in three different ways: (1) changes the paramagnetic CW term, (2) changes the absolute value of diamagnetism, (3) changes the slope of the temperature dependence of the magnetic susceptibility.
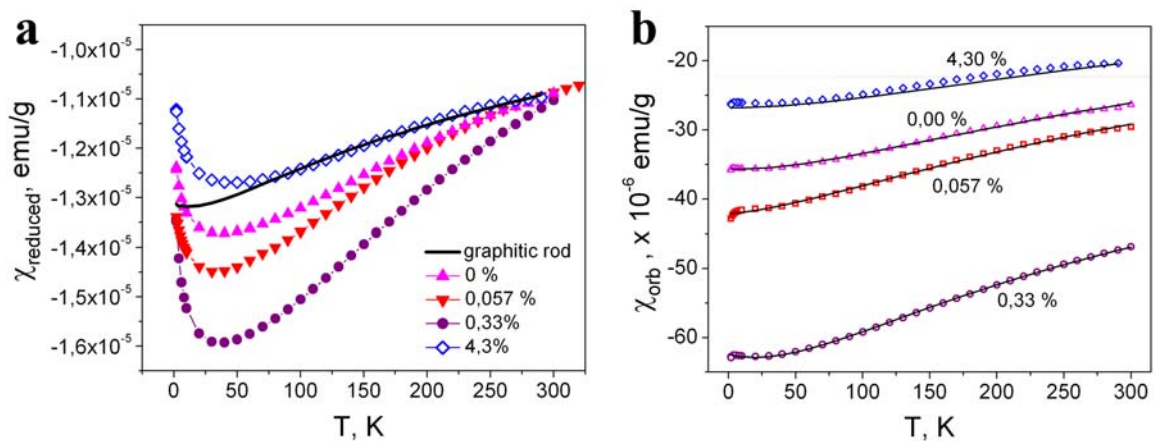

Fig. 27. Reduced magnetic susceptibility data for samples with different boron content (a); orbital susceptibility data for these samples fitted with Kotosonov equation (b).

In **Fig. 27a**, reduced magnetic susceptibilities for samples doped with boron are shown in comparison with the data for graphitic rod. Small constant ferromagnetic contributions were subtracted from all the susceptibility curves for all samples.

The magnetization exhibits the ordinary CW type temperature dependence in the low-temperature (< 30 K) region. Although there is no sign of high-temperature magnetism, nonlinear magnetization is observed at 1.9 K, indicating that samples with low content of magnetic impurities have correlated spins. To find the number of spins, the hysteresis curves were fitted with Langevin formula:

$$M = M_S \cdot \left[\coth \frac{\mu H}{k_B T} - \frac{k_B T}{\mu H} \right], \qquad (2)$$

and it was found that there were 10-20 interacting spins per cluster.

Doping with boron gradually increases the paramagnetic CW contribution. The localized spin density increases, correspondingly, approx. 5 times with a rise in boron content from 0.057 wt % to 0.33 wt %. However, an increase in spin concentration was observed only up to a certain limit. Further doping to 4.3 wt % of boron leads to degradation of the structure to bulk graphite-like behaviour and a decrease of magnetism. While there's still a

prominent paramagnetic CW tail, the concentration of localized spins is reduced by 1.4 times.

Doping with boron also influences absolute values of susceptibility and the temperature slope of the curves, causing a significant increase of the slope of $\chi(T)$ curves due to a strong temperature dependence of the orbital diamagnetism described by Kotosonov theory for disordered carbon materials [150-151]. Having subtracted other terms from the observed value of magnetic susceptibility $\chi_{exp} = \chi_{total}$ (Equation 1), we fitted the resulting curves with the equation

$$\chi_{orb}[emu/g] = -1.3625 \times 10^{-3} \gamma_0^2 \frac{\sec h^2(E_F/2k_B(T+\Delta T))}{(T+\Delta T)}, \quad (3)$$

where E_F – Fermi energy, and $\Delta T = \hbar/\pi k_B \tau$ – Dingle temperature as fitting parameters. Fitting results are presented on **Fig. 27b**. The orbital diamagnetism of NPC is defect-dependent [36] and is enhanced by small amounts of boron, in accordance with the Raman spectroscopy data. Again, there is a critical concentration of boron around 0.33 wt %, and further doping leads to degrading of the structure to bulk graphite-like behaviour and a decrease of magnetism. The orbital diamagnetic susceptibility of the highly-doped structure at RT (-20.3·10^{-6} emu/g) matches that of bulk graphite (-22.6·10^{-6} emu/g).

Fig. 28a shows magnetization data for the studied samples of NPC, with the diamagnetic background subtracted. While all samples demonstrate close values of saturation magnetization, their magnetic behaviour follows the trend in agreement with their structural properties. In freshly prepared samples, boron atoms below critical concentration enhance the magnetic response from the system, and further doping leads to degradation. The total magnetization in graphite generally decreases with the decrease of the separation distance between the defects. Boron atoms can migrate into the places in the graphitic structure that have dangling carbon bonds, and terminate them. At low concentrations of dopant, this process leads to increased distance between the defects and enhanced magnetization, while at high concentrations further saturation of dangling bonds destroys magnetism.

During storage, most dangling bonds in graphite become terminated by oxygen, and that is where the position of boron atoms in the structure might also influence the magnetic properties. With gradual increase in concentration, boron atoms saturate dangling bonds and penetrate into the bulk NPC, far from the defects.
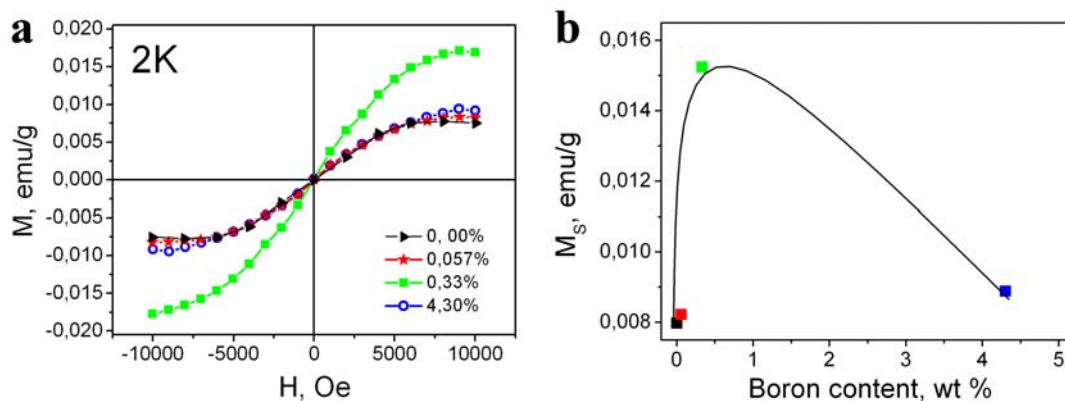
Fig. 28. The field dependences of magnetization for samples with boron taken at 2 K, with diamagnetic background subtracted (a); the dependence of the saturation magnetization on boron content samples (b).

The authors of [86] have shown that a boron atom, which occupies a position far away from the vacancy defect in graphene, slightly enhances the magnetic response from the system. Apparently, this effect fades down, when the concentration of dopant becomes too high. The stronger magnetism observed in a sample with 0.33 wt % content of boron, presumably, corresponds to the borderline case. Note that boron does not induce high-temperature magnetic ordering - room-temperature values of magnetization remain negligible for all samples.

We conclude that doping with boron (unlike transition metal impurities) changes the electronic structure of NPC, which leads to modification of both orbital diamagnetic and Curie-Weiss paramagnetic terms.

4.4. C_2F_x intercalation compounds

The samples of intercalation compounds of graphite fluorides C_2F_x ($x \leq 1$) with embedded guest organic compounds (dichloromethane, dichloroethane, n-hexane, acetone) were synthesized by the group of A. Okotrub as part of a collaboration project (see [152-153] for synthesis details).
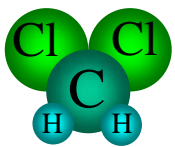
The reaction scheme was as following:
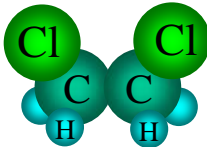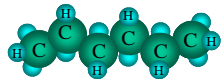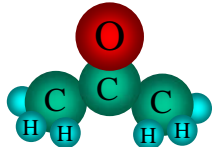
1) Natural graphite + $Br_2 \rightarrow (CBr)_n$ - the second-stage graphite intercalation complex

2) $(CBr)_n + HalF_3 \rightarrow (C_2F_x)_n \bullet aHalF$

3) $(C_2F_x)_n \bullet aHalF \rightarrow (C_2F_x)_n \bullet bGuest + HalF$

The investigated fluorinated graphite compounds are listed in Table 5.

The samples were characterized with XRD and vibrational spectroscopy.

Table 5. Intercalation compounds of graphite fluorides.

Sample	Guest molecule			
	dichloromethane CH_2Cl_2	dichloroethane $C_2H_4Cl_2$	n-hexane $n\text{-}C_6H_{14}$	acetone $(CH_3)_2CO$
1	$C_2F_{0.92}*CH_2Cl_2$	$C_2F_{0.92}*C_2H_4Cl_2$	$C_2F_{0.92}*n\text{-}C_6H_{14}$	$C_2F_{0.92}*(CH_3)_2CO$
2	$C_2F_{0.87}*CH_2Cl_2$	$C_2F_{0.87}*C_2H_4Cl_2$	$C_2F_{0.87}*n\text{-}C_6H_{14}$	$C_2F_{0.87}*(CH_3)_2CO$
3	$C_2F_{0.69}*CH_2Cl_2$	$C_2F_{0.69}*C_2H_4Cl_2$	$C_2F_{0.69}*n\text{-}C_6H_{14}$	$C_2F_{0.69}*(CH_3)_2CO$
4	$C_2F_{0.49}*CH_2Cl_2$	$C_2F_{0.49}*C_2H_4Cl_2$	$C_2F_{0.49}*n\text{-}C_6H_{14}$	$C_2F_{0.49}*(CH_3)_2CO$

The XRD data for samples with dichloromethane and n-hexane guest molecules are shown and compared in **Fig. 29**. All samples show similar trends. Three main interplanar distances monotonically increase with degree of fluorination, their values depending on the size of the incorporated guest molecules.
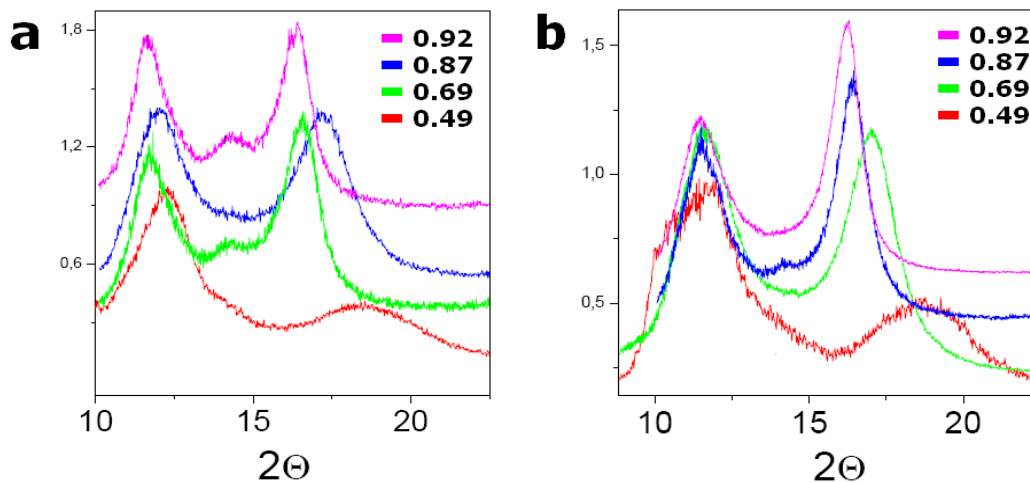

Fig. 29. The XRD spectra for C_2F_x complexes with dichloromethane (a) and n-hexane (b).

The Raman spectra of $C_2F_{0.49}$ compounds are shown on **Fig. 30**. Both first and second order spectra contain characteristic lines for disordered graphite. The G peak is shifted to 1600 cm^{-1}, which is the sign of nanographite, and I_D/I_G ration gives crystallite sizes in the range 4-7 nm.
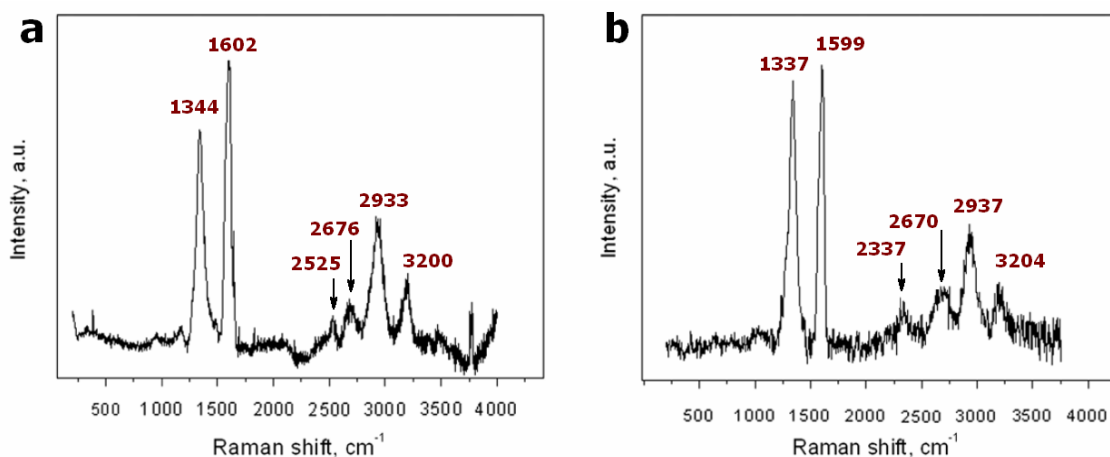
Fig. 30. The Raman spectra for C_2F_x compounds with dichloromethane (a), n-hexane (b).

For higher fluorination degrees, all major lines are preserved but the spectra are masked by a strong luminescence background.

The temperature dependences of the susceptibility of fluorinated graphite samples in the temperature range from 1.75 to 300 K follow the CW temperature dependence.
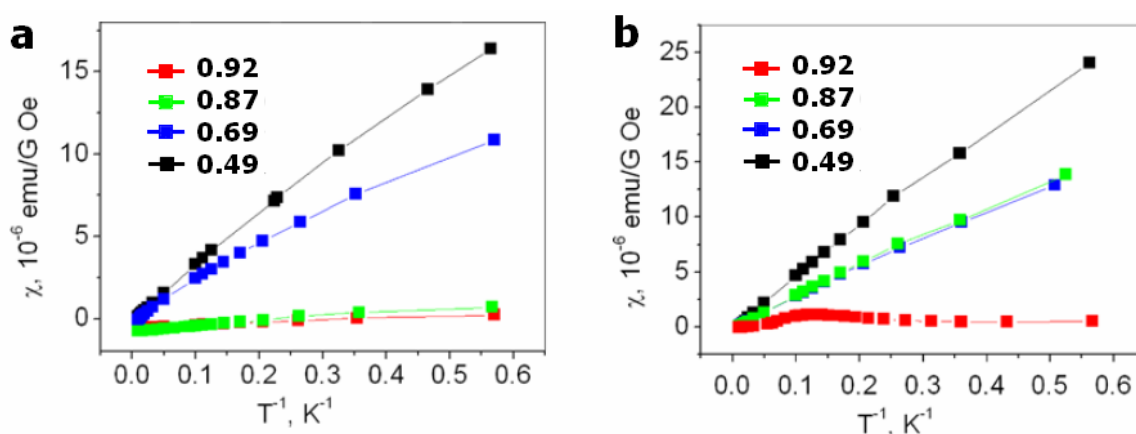
Fig. 31. The dependence of susceptibility vs 1/T for C_2F_x with n-hexane (a) and dichloromethane (b).

Plotted versus reciprocal temperature (**Fig. 31**), the susceptibility curves demonstrate deviations from linearity at low temperatures, which is the sign of antiferromagnetic ordering. Analysis of the curves has shown the Weiss constant to be negative for all samples except $C_2F_{0.92}$, diluted with dichloromethane, and lie in the range of 0.5–6 K. The temperature dependences of the magnetic susceptibility indicate that fluorination leads to a strong increase in the concentration of unpaired spins.
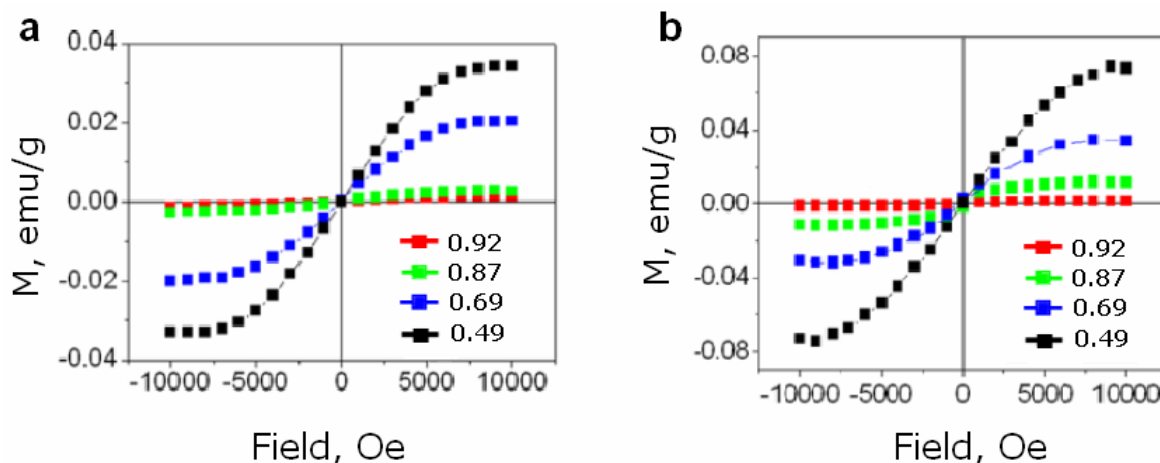
Fig. 32. The hysteresis loops for C_2F_x compounds with n-hexane (a) and dichloromethane (b) guest molecules, taken at 2 K.

Hysteresis loops for C_2Fx samples with n-hexane and dichloromethane guest molecules are shown on **Fig. 32**. Even in the fields below 1 T, at the temperatures 1.75–10 K nonlinear magnetization is observed, indicating that fluorinated samples have groups of correlated spins. The curves were fitted by the Langevin function, and it has been found that there are 10-25 interacting spins per cluster.
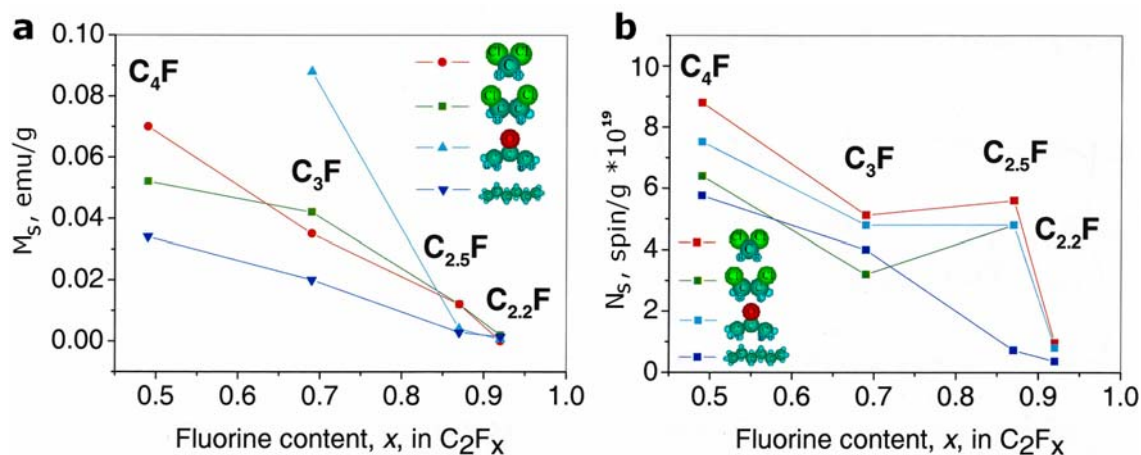
Fig. 33. The dependences of the saturation magnetization values (a) and the localized spin concentrations (b) on fluorine content in C_2F_x compounds.

The Particle Induced X-ray Emission (P.I.X.E.) impurity analysis performed for our samples proved that the observed nonlinear magnetization is of intrinsic character and can be ascribed to the interacting carbon atoms. An estimate of the average magnetic moment μ in the samples gives μ of about 12–15 μ_B for n-hexane intercalated samples and about 25 μ_B for dichloromethane intercalated graphite fluoride.

Impurity Sample	Cr, ppm	Mn, ppm	Fe, ppm	Co, ppm	Ni, ppm	Cu, ppm	Zn, ppm
$C_2F_{0.92}*CH_2Cl_2$	< 0.6	< 0.5	< 0.4	< 0.4	< 0.5	4.5	< 0.5

The concentration of paramagnetic centers depends on the degree of fluorination and decreases with the increase in the number of covalent bonds. A decrease of the high-spin clusters in the graphite fluoride (**Fig. 33a**) results from a decrease in spin concentration (**Fig. 33b**). The $C_2F_{0.92}$ samples have a spin density of $\sim 1 \times 10^{18}$ spin/g, whereas in the $C_2F_{0.49}$ samples this parameter reaches 1×10^{20} spin/g. However, the number of spins in the clusters does not depend on fluorination degree but is close to a certain constant for every inclusion compound.

To conclude, we have investigated the structural and magnetic properties of C_2F_x samples with varying fluorine content and guest molecules, and have shown that such intercalated graphite systems possess intrinsic magnetism, which can be tuned by the degree of intercalation.

5. Concluding remarks and future plans

In the past decade, carbon materials have been intensively investigated, purportedly, to find the base for a new generation of electronics and computing.

The results presented in this thesis complement previous works on carbon-related magnetism, provide more insight into mechanisms of magnetic ordering in carbon-based nanostructures, and make a bridge between carbon-based and low-dimensional organic magnets.

We have investigated the magnetic properties of 0D – 3D systems of magnetic carbon nanostructures, namely, carbon nanotubes weakly doped with iron, fullerene C_{60} complexes with oxocarboxylate clusters of the Mn_{12} SMM family, underfluorinated intercalation compounds of graphite, and nanoporous carbon.

We have shown that the magnetic properties of such structures are dominated by finite-size effects. Thus, quantum effects change the magnetic thermal behaviour of weakly doped carbon nanotubes. The choice of ligands influences the properties of Mn_{12} molecular magnets, and functionalization with fullerenes leads to orientation-controlled magnetism: the network of fullerene molecules safely "freezes" the magnetic moment, while the properties of the system as a single molecular magnet are preserved. Magnetism of "pure carbon" systems, such as graphite fluorides and nanoporous carbon, is defined by type, concentration and relative positions of "imperfections" of the carbon lattice, but further investigations are required to reveal an accurate model.

Our nearest goal is to continue studies of quasi-two-dimensional carbon magnetic systems, based on underfluorinated C2Fx compounds, which seem, at different stages to demonstrate a wide range of types of magnetic behaviour, i.e. in addition to diamagnetic and paramagnetic contributions, the presence of competing exchange interactions is evident.

6. Conferences, summer schools, and other activities

Crossing perspectives on Gender and Physics (the 4th annual meeting of Nordic Network of Women in Physics)
September 17 – 19, 2008, Uppsala, Sweden.
Poster: *THz emission under impurity breakdown in n-GaAs/AlGaAs quantum wells.*

International Conference "New in Magnetism and Magnetic Materials"
(NMMM'2009)
June 28 – July 2, 2009, Moscow, Russia.
Oral presentation: *Fullerene-containing molecular magnets of Mn_{12} family.*

9th Biennial International Workshop "Fullerenes and Atomic Clusters"
(IWFAC'2009),
July 6 – 10, 2009, St. Petersburg, Russia.
Poster: *Magnetic properties of carbon nanotubes with low content of Fe.*
Poster: *Magnetization training effect in fullerene-containing single molecular magnet.*

International Winterschool on Electronic Properties of Novel Materials
(IWEPNM'2010),
March 6 – 13, 2010, Kirchberg, Austria.
Poster: *Fullerene-induced magnetization training effect in single molecular magnet.*

International Conference with Summer School on Superconductivity and Magnetism
(ICSM'2010) (attended thanks to HT2009 SJCKMS scholarship)
April 25 – 30, 2010, Antalya, Turkey.
Poster: *Synthesis and magnetic properties of Mn_{12} single-molecule magnet $Mn_{12}O_{12}(O_2CC_6H_4CN(-p))_{16}(H_2O)_4$ with enhanced magnetic anisotropy.*

International Conference on Nanoscale Magnetism (ICNM'2010) (not attended in person)
September 28 – October 2, 2010, Istanbul, Turkey.
Poster: *Microstructural Evolution and Magnetic Properties of Underfluorinated Graphite.*

Joint International Conference "Advanced Carbon Nanostructures" (ACN'2011) with School for Young Scientists

July 4 – 8, 2011, St. Petersburg, Russia.

Poster: *Transient charging phenomena in graphite.*

11th International Conference on Atomically Controlled Surfaces, Interfaces and Nanostructures (ACSIN'2011)

October 3 - 7, 2011, St. Petersburg, Russia.

Poster: *The magnetic properties of B-doped oxygen-eroded graphite.*

3rd European Conference on Molecular Magnetism (ECMM'2011) (attended thanks to ÅForsk foundation stipend)

November 22 - 25, 2011, Paris, France.

Poster: *Low-dimensional magnetism in semi-fluorinated graphite.*

"Towards Reality in Nanoscale Materials V" Workshop (TRNM'2012)

February 20 – 22, 2012, Levi, Finland.

Poster: *Influence of boron doping on the defect-induced magnetism of oxygen-eroded graphite.*

Acknowledgements

References

[1] J. Svensson, Yu. Tarakanov, D. S. Lee, J. M. Kinaret, Y. W. Park, and E. E. B. Campbell. A carbon nanotube gated carbon nanotube transistor with 5 ps gate delay. *Nanotechnol.* **19** (2008), p. 325201.

[2] W. J. Yu, B. R. Kang, I. H. Lee, Y. S. Min, and Y. H. Lee. Majority carrier type conversion with floating gates in carbon nanotube transistors. *Adv. Mater.* **21** (2009), pp. 4821–4824.

[3] S.-C. J. Huang, A. B. Artyukhin., N. Misra, J. A. Martinez, P. A. Stroeve, C. P. Grigoropoulos, J.-W. W. Ju, and A. Noy. Carbon Nanotube Transistor Controlled by a Biological Ion Pump Gate. *Nano Lett.* **10** (2010), pp. 1812–1816.

[4] A. T. Costa, E. Borowiak-Palen, A. Bachmatiuk, M. H. Rummeli, T. Gemming, and R. J. Kalenczuk. Filling of carbon nanotubes for bio-applications. *Phys. Stat. Sol. (b)* **244** (2007), pp. 4315– 4318.

[5] L. Mönch, A. Meye, A. Leonhardt, K. Krämer, R. Kozhuharova, and T. Gemming. Ferromagnetic filled carbon nanotubes and nanoparticles: synthesis and lipid-mediated delivery into human tumor cells. *J. Magn. Magn. Mater.* **290** (2005), pp. 276–278.

[6] F. Wolny, T. Muhl, U. Weissker, K. Lipert, J. Schumann, A. Leonhardt, and B. Buchner. Iron filled carbon nanotubes as novel monopole-like sensors for quantitative magnetic force microscopy. *Nanotechnology* **21** (2010), p. 435501.

[7] C. Wang, R. Lv, F. Kang, J. Gua, X. Guib, and D. Wub. Synthesis and application of iron-filled carbon nanotubes coated with FeCo alloy nanoparticles. *J. Magn. Magn. Mater.* **321** (2009), pp. 1924–1927.

[8] M. N. Leuenberger and D. Loss. Quantum computing in molecular magnets. *Nature* **410** (2001), pp. 789–793.

[9] J. Tejada, E. M. Chudnovsky, E. del Barco, J. M. Hernandez, and T. P. Spiller. Magnetic qubits as hardware for quantum computers. *Nanotechnol.* **12** (2001), pp. 181–186.

[10] S. Hill, R. S. Edwards, N. Aliaga-Alcalde, and G. Christou. Quantum coherence in an exchange-coupled dimer of single-molecule magnets. *Science* **302** (2003), pp. 1015–1018.

[11] M. Affronte. Molecular nanomagnets for information technologies. *J. Mater. Chem.* **19** (2009), pp. 1731–1737.

[12] Y. Takabayashi, A. Yu. Ganin, M. J. Rosseinsky, and K. Prassides. Direct observation of magnetic ordering in the $(CH_3NH_2)K_3C_{60}$ fulleride. *Chem. Commun.* (2007), pp. 870–872.

[13] J. Arvanitidis, K. Papagelis, Y. Takabayashi, T. Takenobu, Y. Iwasa, M. J. Rosseinsky, and K. Prassides. Magnetic ordering in the ammoniated alkali fullerides $(NH_3)K_{3-x}Rb_xC_{60}$ (x = 2, 3). *J. Phys.: Condens. Matter* **19** (2007), p. 386235.

[14] H. Pardo, R. Faccio, F.M. Araujo-Moreira, O.F. de Lima, and A.W. Mombru. Synthesis and characterization of stable room temperature bulk ferromagnetic graphite. *Carbon* **44** (2006), pp. 565–569.

[15] R. L. Vander Wal, G. M. Berger and T. M. Ticich. Carbon nanotube synthesis in a flame using laser ablation for in situ catalyst generation. *Appl. Phys. A* **77** (2003), pp. 885-889.

[16] B. Wang, Y. Ma, Y. Wu, N. Li, Y. Huang, Y. Chen. Direct and large scale electric arc discharge synthesis of boron and nitrogen doped single-walled carbon nanotubes and their electronic properties. *Carbon* **47** (2009), pp. 2112–2142.

[17] T. Watanabe, T. Notoya, T. Ishigaki, H. Kuwano, H. Tanaka, and Y. Moriyoshi. Growth mechanism for carbon nanotubes in a plasma evaporation process. *Thin Solid Films* **506– 507** (2006), pp. 263 – 267.

[18] J. Sengupta and C. Jacob. Pre-Heating Effect on the Catalytic Growth of Partially Filled Carbon Nanotubes by Chemical Vapor Deposition. *J. Nanosci. Nanotechnol.* **10** (2010), pp. 3064–3071.

[19] R. Philippe, B. Caussat, A. Falqui, Y. Kihn, P. Kalck, S. Bordère, D. Plee, P. Gaillard, D. Bernard, and P. Serp. An original growth mode of MWCNTs on alumina supported iron catalysts. *J. Catal.* **263** (2009), pp. 345–358.

[20] S. Maruyama, http://www.photon.t.u-tokyo.ac.jp.

[21] U. Weissker, S. Hampel, A. Leonhardt, and B. Büchner. Carbon nanotubes filled with ferromagnetic materials. *Materials* **3** (2010), pp. 4387–4427.

[22] S. Hampel, A. Leonhardt, D. Selbmann, K. Biedermann, D. Elefant, Ch. Müller, T. Gemming, and B. Büchner. Growth and characterization of filled carbon nanotubes with ferromagnetic properties. *Carbon* **44** (2006), pp. 2316–2322.

[23] R. S. Iskhakov, S. V. Komogortsev, A. D. Balaev, L. A. Chekanova. Dimensionality of a system of exchange-coupled grains and magnetic properties of nanocrystalline and amorphous ferromagnets. *JETP Lett.* **72** (2000), pp. 304–307.

[24] T. Fujita, M. Chen, X. Wang, B. Xu, K. Inoke, K. Yamamoto. Electron holography of single-crystal iron nanorods encapsulated in carbon nanotubes. *J. Appl. Phys.* **101** (2007), pp. 014323–014327.

[25] P. Banerjee, F. Wolny, D. V. Pelekhov, M. R. Herman, K. C. Fong, U. Weissker, T. Muhl, Y. Obukhov, A. Leonhardt, B. Buchner, P. C. Hammel. Magnetization Reversal in an Individual 25 nm Iron-Filled Carbon Nanotube. *Appl. Phys. Lett.* **96** (2010), pp. 252505–252507.

[26] I. S. Lyubutin, K. V. Frolov, O. A. Anosova, V. S. Pokatilov, A. V. Okotrub, A. G. Kudashov, Y. V. Shubin, L. G. Bulusheva. Phase states and magnetic properties of iron nanoparticles in carbon nanotube channels. *J. Exp. Theor. Phys.* **109** (2009), pp. 254–261.

[27] J. Jorge, E. Flahaut, F. Gonzalez-Jimenez, G. Gonzalez, J. Gonzalez, E. Belandria, J. M. Broto, and B. Raquet. Preparation and characterization of α-Fe nanowires located inside double wall carbon nanotubes. *Chem. Phys. Lett.* **457** (2008), pp. 347–351.

[28] Y.-R. Jang and J. I. Lee. Magnetism of linear Fe, Co, and Ni nanowires encapsulated in zigzag (n,0) carbon nanotubes (CNT) with n = 5 to 9: A first-principles study. *Phys. Stat. Sol. (b)* **244** (2007), pp. 4407–4410.

[29] A. Winkler, T. Muhl, S. Menzel, R. Kozhuharova-Koseva, S. Hampel, A. Leonhardt, B. Buchner. Magnetic force microscopy sensors using iron-filled carbon nanotubes. *J. Appl. Phys.* **99** (2006), pp. 104905–104909.

[30] T. Fujita, M. Chen, X. Wang, B. Xu, K. Inoke, K. Yamamoto. Electron holography of single-crystal iron nanorods encapsulated in carbon nanotubes. *J. Appl. Phys.* **101** (2007), pp. 014323–014327.

[31] S. Voss, M. Fonin, L. Burova, M. Burgert, Y. S. Dedkov, A. B. Preobrajenski, E. Goering, U. Groth, A. R. Kaul, and U. Ruediger. Investigation of the stability of Mn_{12} single molecule magnets. *Appl. Phys. A* **94** (2009), pp. 491–495.

[32] J. Camarero and E. Coronado. Molecular vs. inorganic spintronics: the role of molecular materials and single molecules. *J. Mater. Chem.* **19** (2009), pp. 1678–1684.

[33] E Ruiz, J. Cirera, J. Cano, S. Alvarez, C. Loose, and J. Kortus. Can large magnetic anisotropy and high spin really coexist? *Chem. Commun.* **1** (2008), pp. 52–54.

[34] P.-H. Lin, T. J. Burchell, L. Ungur, L. F. Chibotaru, W. Wernsdorfer, and M. Murugesu. A polynuclear lanthanide single-molecule magnet with a record anisotropic barrier. *Angew. Chem. Int. Ed.* **48** (2009), pp. 9489–9492.

[35] Y. Ma, G.-F. Xu, X. Yang, L.-C. Li, J. Tang, S.-P. Yan, P. Cheng, and D.-Z. Liao. Pyrazine-bridged Dy_2 single-molecule magnet with a large anisotropic barrier. *Chem. Commun.* **46** (2010), pp. 8264–8266.

[36] V. M. Mereacre, A. M. Ako, R. Clérac, W. Wernsdorfer, G. Filoti, J. Bartolomé, C. E. Anson, and A. K. Powell. A Bell-Shaped $Mn_{11}Gd_2$ Single-Molecule Magnet. *J. Am. Chem. Soc.* **129** (2007), pp. 9248–9249.

[37] V. Mereacre, Y. Lan, R. Clérac, A. M. Ako, W. Wernsdorfer, G. Buth, C. E. Anson, and A. K. Powell. Contribution of Spin and Anisotropy to Single Molecule Magnet Behavior in a Family of Bell-Shaped Mn11Ln2 Coordination Clusters. *Inorg. Chem.* **50** (2011), pp. 12001–12009.

[38] T. Lis. Preparation, structure, and magnetic properties of a dodecanuclear mixed-valence manganese carboxylate. *Acta Crystallogr. B* (1980) **36** 2042–2046.

[39] C. J. Milios, A. Vinslava, W. Wernsdorfer, S. Moggach, S. Parsons, S. P. Perlepes, G. Christou, and E. K. Brechin. A Record Anisotropy Barrier for a Single-Molecule Magnet. *J. Am. Chem. Soc.* **129** (2007), pp. 2754–2755.

[40] D. M. Seo, V. Meenakshi, W. Teizer, H. Zhao, and K. R. Dunbar. Enhanced magnetic anisotropy of Mn_{12}-acetate. *J. Mag. Magn. Mater.* **301** (2006), pp. 31–36.

[41] D. P. Goldberg, A. Caneschi, S. J. Lippard. A decanuclear mixed-valent manganese complex with a high spin multiplicity in the ground state. *J. Am. Chem. Soc.* **115** (1993), pp. 9299–9300.

[42] M. Murugesu, S. Takahashi, A. Wilson, K. A. Abboud, W. Wernsdorfer, S. Hill, and G. Christou. Large Mn_{25} single-molecule magnet with spin S = 51/2: magnetic and high-frequency electron paramagnetic resonance spectroscopic characterization of a giant spin state. *Inorg. Chem.* **47** (2008), pp. 9459–9470.

[43] A. M. Ako, I. J. Hewitt, V. Mereacre, R. Clerac, W. Wernsdorfer, C. E. Anson, and A. K. Powell. A ferromagnetically coupled Mn_{19} aggregate with a record S=83/2 ground spin state. *Angew. Chem. Int. Ed*. **45** (2006), pp. 4926–4929.

[44] A. J. Tasiopoulos, A. Vinslava, W. Wernsdorfer, K. A. Abboud, and G. Christou. Giant single-molecule magnets: a {Mn_{84}} torus and its supramolecular nanotubes. *Angew. Chem. Int. Ed*. **43** (2004) pp. 2117–2121.

[45] S. M. J. Aubin, N. R. Dilley, L. Pardi, J. Krzystek, M. W. Wemple, L.-C. Brunel, M. B. Maple, G. Christou, and D. N. Hendrickson. Resonant magnetization tunneling in the trigonal pyramidal $MnIVMnIII_3$ complex [$Mn_4O_3Cl(O_2CCH_3)_3(dbm)_3$] *J. Am. Chem. Soc.* **120** (1998) pp. 4991–5004.

[46] A. Naitabdi, J.-P. Bucher, Ph. Gerbier, P. Rabu, M. Drillon. Self-assembly and magnetism of Mn-12 nanomagnets on native and functionalized gold surfaces. *Adv. Mater.* **17** (2005) pp. 1612–1616.

[47] M. Soler, W. Wernsdorfer, K. Folting, M. Pink, G. Christou. Single-Molecule Magnets: a large Mn_{30} molecular nanomagnet exhibiting quantum tunneling of magnetization. *J. Am. Chem. Soc.* **126** (2004) pp. 2156–2165.

[48] J. Yoo, E. K. Brechin, A. Yamaguchi, M. Nakano, J. C. Huffman, A. L. Maniero, L. C. Brunel, K. Awaga, H. Ishimoto, G. Christou, D. N. Hendrickson. Single-Molecule Magnets: a new class of tetranuclear manganese magnets. *Inorg. Chem.* **39** (2000), pp. 3615–3623.

[49] D. Gatteschi and R. Sessoli. Quantum Tunneling of Magnetization and Related Phenomena in Molecular Materials. *Angew. Chem. Int. Ed*. **42** (2003), pp. 268–297.

[50] A. M. Gomes, M. A. Novak, W. Wernsdorfer, R. Sessoli, L. Sorace, D. Gatteschi. Quantum tunneling of magnetization in $Mn_{12}Bz$ clusters: Evidences of spin parity effect. *J. Appl. Phys.* **87** (2000), pp. 6004–6006.

[51] W. Wernsdorfer. Quantum dynamics in molecular nanomagnets. *C. R. Chimie* **11** (2008), pp. 1086–1109.

[52] K. Takeda and K. Awaga. Single molecular magnets, in Chemistry of nanomolecular systems (Eds: T. Nakamura, T. Matsumoto, H. Tada, and K.-I. Sugiura). Published by Springer-Verlag, New-York (2003), p. 41.

[53] J. Villain, F. Hartman-Boutron, R. Sessoli, and A. Rettori. Magnetic relaxation in big magnetic molecules. *Europhys. Lett.* **27** (1994), pp. 159–164.

[54] S. M. J. Aubin, D. Ruiz, E. Rumberger, Z. Sun, B. Albela, M. W. Wemple, N. R. Dilley, J. Ribas, M. B. Maple, G. Christou, and D. N. Hendrickson. Resonant Magnetization Tunneling in Single-Molecule Magnets. *Mol. Cryst. and Liq. Cryst.* **335** (1999), pp. 371–389.

[55] J. M. Carlsson. Simulations of the Structural and Chemical Properties of Nanoporous Carbon, in Computer-Based Modeling of Novel Carbon Systems and Their Properties: Beyond Nanotubes (Eds: L. Colombo and A. Fasolino). Published by Springer, Dordrecht-New York-Heidelberg-London (2010), p. 79.

[56] G. Mestl, N. I. Maksimova, N. Keller, V. V. Roddatis, and R. Schlogl. Carbon nanofilaments in heterogeneous catalysis: An industrial application for new carbon materials? *Angew. Chem. Int. Ed.* **40** (2001), p. 2066–2068.

[57] M. Anbia and Z. Parvin. Desulfurization of fuels by means of a nanoporous carbon adsorbent. *Chem. eng. res. des.* **89** (2011), pp. 641–647.

[58] C. J. Anderson, W. Tao, C. A. Scholes, G. W. Stevens, and S. E. Kentish. The performance of carbon membranes in the presence of condensable and non-condensable impurities. *J. Mem. Sci.* **378** (2011), pp. 117–127.

[59] C. Vix-Guterl, E. Frackowiak, K. Jurewicz, M. Friebe, J. Parmentierc, and F. Béguin. Electrochemical energy storage in ordered porous carbon materials. *Carbon* **43** (2005), pp. 1293–1302.

[60] D. Giasafaki, A. Bourlinos, G. Charalambopoulou, A. Stubos, and T. Steriotis. Nanoporous carbon – metal composites for hydrogen storage. *Cent. Eur. J. Chem.* **9** (2011), pp. 948–952.

[61] E. Kockrick, C. Schrage, L. Borchardt, N. Klein, M. Rose, I. Senkovska, and S. Kaskel. Ordered mesoporous carbide derived carbons for high pressure gas storage. *Carbon* **48** (2010), pp. 1707–1717.

[62] P. Simon and Y. Gogotsi. Materials for electrochemical capacitors. *Nat. Mater.* **7** (2008), pp. 845–854.

[63] G. Sun, W. Song, X. Liu, W. Qiao, D. Long, and L. Ling. New concept of in situ carbide-derived carbon/xerogel nanocomposite materials for electrochemical capacitor. *Mater. Lett.* **65** (2011), pp. 1392–1395.

[64] J. Torop, V. Palmre, M. Arulepp, T. Sugino, K. Asaka, and A. Aabloo. Flexible supercapacitor-like actuator with carbide-derived carbon electrodes. *Carbon* **49** (2011), pp. 3113–3119.

[65] K. Kraiwattanawong, N. Sano, and H. Tamon. Low-cost production of mesoporous carbon/carbon composite cryogels. *Carbon* **49** (2011), pp. 3404–3411.

[66] W. Xing, S. P. Zhuo, X. L. Gao. Alpha-Fe-incorporated nanoporous carbon with magnetic properties. *Mater. Lett.* **63** (2009), pp. 1177–1179.

[67] C. L. Burket, R. Rajagopalan, and H. C. Foley. Synthesis of nanoporous carbon with pre-graphitic domains, *Carbon* **45** (2007), pp. 2307–2320.

[68] D. C. Wu, H. C. Dong, J. Pietrasik, E. K. Kim, C. M. Hui, M. J. Zhong, M. Jaroniec, T. Kowalewski, and K. Matyjaszewski. Novel Nanoporous Carbons from Well-Defined Poly(styrene-co-acrylonitrile)-Grafted Silica Nanoparticles. *Chem. Mater.* **23** (2011), pp. 2024–2026.

[69] V. Presser, M. Heon, Y. Gogotsi, Carbide-Derived Carbons - From Porous Networks to Nanotubes and Graphene. *Adv. Funct. Mater.* **21** (2011), pp. 810–833.

[70] S. Osswald, C. Portet, Y. Gogotsi, G. Laudisio, J. P. Singer, J. E. Fischer, V. V. Sokolov, J. A. Kukushkina, and A. E. Kravchik. Porosity control in nanoporous carbide-derived carbon by oxidation in air and carbon dioxide, *J. Sol. St. Chem.* **182** (2009), pp. 1733–1741.

[71] R. P. Pant, M. Arora, C. Lal, A. Veer, S. Singh, and R. B. Mathur. Synthesis and characterization of cluster-assembled carbon thin films. *Ind. J. Eng. Mater. Sci.* **17** (2010), pp. 363–366.

[72] A. V. Rode, E. G. Gamaly, and B. Luther-Davies. Formation of cluster-assembled carbon nano-foam by high-repetition-rate laser ablation. *Appl. Phys. A* **70** (2000), pp. 135–144.

[73] P. Milani, M. Ferretti, P. Piseri, C. E. Bottani, A. Ferrari, A. L. Bassi, G. Guizetti, and M. Patrini. Synthesis and characterization of cluster-assembled carbon thin films. *J. Appl. Phys.* **82** (1997), pp. 5793–5798.

[74] Q. Y. Hu, J. B. Pang, Z. W. Wu, Y. and F. Lu. Tuning pore size of mesoporous carbon via confined activation process. *Carbon* **44** (2006), pp. 1349–1352.

[75] N. M. Mikova, N. V. Chesnokov, and B. N. Kuznetsov. Study of High Porous Carbons Prepared by the Alkaline Activation of Anthracites. *J. Sib. Fed. Univ. Chem.* **1** (2009), pp. 3–10.

[76] N. V. Sych, N. T. Kartel', A. D. Nikolaichuk, V. V. Strelko, N. N. Tsyba, and V. A. Denisovich. Integrated Processing of Anthracite into Sorption Materials. *Rus. J. Appl. Chem.* **79** (2006), pp. 722–726.

[77] P. M. Barata-Rodrigues, T. J. Mays, and G. D. Moggridge. Structured carbon adsorbents from clay, zeolite and mesoporous aluminosilicate templates. *Carbon* **41** (2003), pp. 2231–2246.

[78] R. R. Nair, M. Sepioni, I.-L. Tsai, O. Lehtinen, J. Keinonen, A. V. Krasheninnikov, T. Thomson, A. K. Geim, and I. V. Grigorieva. Spin-half paramagnetism in graphene induced by point defects. *Nat. Phys.* (2012) doi: 10.1038/NPHYS2183.

[79] F. J. Owens, Z. Iqbal, L. Belova, and K. V. Rao. Evidence for high-temperature ferromagnetism in photolyzed C(60). *Phys. Rev. B* **69** (2004), p. 033403.

[80] P. Esquinazi, A. Setzer, R. Höhne, C. Semmelhack, Y. Kopelevich, D. Spemann, T. Butz, B. Kohlstrunk, and M. Losche. Ferromagnetism in oriented graphite samples, *Phys. Rev. B* **66** (2002), p. 024429.

[81] S. Li, G. Ji, and L. Lü. Magnetic carbon nanofoams. *J. Nanosci. Nanotech.* **9** (2009), pp. 1133–1136.

[82] T. Enoki and K. Takai. The edge state of nanographene and the magnetism of the edge-state spins. *Sol. State Commun.* **149** (2009), pp. 1144–1150.

[83] M. Kiguchi, K. Takai, V. L. J. Joly, T. Enoki, R. Sumii, and K. Amemiya. Magnetic edge state and dangling bond state of nanographene in activated carbon fibers. *Phys. Rev. B* **84** (2011), p. 045421.

[84] A. V. Rode, E. G. Gamaly, A. G. Christy, J. G. F. Gerald, S. T. Hyde, R. G. Elliman, B. Luther-Davies, A. I. Veinger, J. Androulakis, and J. Giapintzakis. Unconventional magnetism in all-carbon nanofoam. *Phys. Rev. B* **70** (2004), p. 054407.

[85] O. V. Yazyev and L. Helm. Defect-induced magnetism in graphene. *Phys. Rev. B* **75** (2007), p. 125408.

[86] Y. Zhang, S. Talapatra, S. Kar, R. Vajtai, S. K. Nayak, and P. M. Ajayan. First-Principles Study of Defect-Induced Magnetism in Carbon. *Phys. Rev. Lett.* **99** (2007), p. 107201.

[87] R. Faccio, L. Fernandez-Werner, H. Pardo, C. Goyenola, O. N. Ventura, and A. W. Mombru. Electronic and Structural Distortions in Graphene Induced by Carbon Vacancies and Boron Doping. *J. Phys. Chem. C* **114** (2010), pp. 18961–18971.

[88] J. Fernandez-Rossier and J. J. Palacios. Magnetism in graphene nanoislands. *Phys. Rev. Lett.* **99** (2007), p. 177204.

[89] C. Tao, L. Jiao, O. V. Yazyev, Y.-C. Chen, J. Feng, X. Zhang, R. B. Capaz, J. M. Tour,A. Zettl, S. G. Louie, H. Dai, and M. F. Crommie. Spatially resolving edge states of chiral graphene nanoribbons. *Nat. Phys.* **7** (2011), pp. 616–620.

[90] W. Sheng, Z. Y. Ning, Z. Q. Yang, and H. Guo. Magnetism and perfect spin filtering effect in graphene nanoflakes. *Nanotechnol.* **21** (2010), p. 385201.

[91] O. V. Yazyev, W. L. Wang, S. Meng, and E. Kaxiras. Comment on graphene nanoflakes with large spin: Broken-symmetry states. *Nano Lett.* **9** (2008), p. 766.

[92] H. Kumazaki and D. S. Hirashima. Local magnetic moment formation on edges of graphene. *J. Phys. Soc. Jpn*, **77** (2008), p. 044705.

[93] S. Bhowmick and V. B. Shenoy. Edge state magnetism of single layer graphene nanostructures. *J. Chem. Phys.* **128** (2008), p. 244717.

[94] J. Červenka, M. I. Katsnelson, and C. F. J. Flipse. Room-temperature ferromagnetism in graphite driven by two-dimensional networks of point defects. *Nat. Phys.* **5** (2009), pp. 840–844.

[95] P. Esquinazi, D. Spemann, R. Höhne, A. Setzer, K. H. Han, and T. Butz. Induced magnetic ordering by proton irradiation in graphite. *Phys. Rev. Lett.* **91** (2003), p. 227201.

[96] T. L. Makarova, A. L. Shelankov, I. T. Serenkov, V. I. Sakharov, and D. W. Boukhvalov. Anisotropic magnetism of graphite irradiated with medium-energy hydrogen and helium ions. *Phys. Rev. B* **83** (2011), p. 085417.

[97] H. Lee, Y. Miyamoto, and J. Yu. Possible origins of defect-induced magnetic ordering in carbon-irradiated graphite. *Phys. Rev. B* **79** (2009), p. 121404.

[98] M. Acharya, M. S. Strano, J. P. Mathews, S. J. L. Billinge, V. Petkov, S. Subramoney, and H. C. Foley. Simulation of nanoporous carbons: a chemically constrained structure. *Phil. Mag. B* 79 (1999), pp. 1499–1518.

[99] S. J. Townsend, T. J. Lenosky, D. A. Muller, C. S. Nichols, and V. Elser. Negatively curved graphitic sheet model of amorphous carbon. *Phys. Rev. Lett.* **69** (1992), pp. 921–924.

[100] A. W. Mombrú, H. Pardo, R. Faccio, O. F. de Lima, E. R. Leite, G. Zanelatto, A. J. C. Lanfredi, C. A. Cardoso, and F. M. Araujo-Morejra. Multilevel ferromagnetic behavior of room-temperature bulk magnetic graphite. *Phys. Rev. B* **71** (2005), p. 100404.

[101] D. Arčon, Z. Jagličič, A. Zorko, A. V. Rode, A. G. Christy, N. R. Madsen, E. G. Gamaly, and B. Luther-Davies. Origin of magnetic moments in carbon nanofoam. *Phys. Rev. B* **74** (2006), p. 014438.

[102] K. Takai, T. Suzuki, T. Enoki, H. Nishihara, and T. Kyotani. Fabrication and characterization of magnetic nanoporous zeolite-templated carbon. *J. Phys. Chem. Sol.* **71** (2010), pp. 565–568.

[103] Y. Kopelevich, R. R. da Silva, J. H. S. Torres, A. Penicaud, and T. Kyotani. Local ferromagnetism in microporous carbon with the structural regularity of zeolite Y. *Phys. Rev. B* **68** (2003), p. 092408.

[104] N. Watanabe, T. Nakajima, and H. Touhara. Graphite fluorides. Published by Elsevier, Amsterdam-Oxford-New York-Tokio (1988), p. 41.

[105] R. L. Fusaro. Graphite fluoride lubrication: the effect of fluorine content, atmosphere, and burnishing technique. *ASLE Trans.* **20** (1977), pp. 15–24.

[106] J. V. Rani, S. B. Rushi, V. Kanakaiah, and S. Palaniappan. Green Fluorination of Natural Graphite and its Application in Rechargeable Magnesium Ion Transfer Battery. *J. Electrochem. Soc.* **158** (2011), pp. A1031–A1035.

[107] K. Takai, H. Sato, T. Enoki, N. Yoshida, F. Okida, H. Touhara, and M. Endo. Effect of fluorination on nano-sized π-electron systems. *J. Phys. Soc. Jpn.* **70** (2001), pp. 175–185.

[108] A. M. Panich, A. I. Shames, and T. Nakajima. On paramagnetism in fluorinated graphite: EPR and solid state NMR study. *J. Phys. Chem. Sol.* **62** (2001), pp. 959–964.

[109] M. Maruyama, K. Kusakabe, S. Tsuneyuki, K. Akagi, Y. Yoshimoto, J. Yamauchi. Magnetic properties of nanographite with modified zigzag edges. *J. Phys. Chem. Sol.* **65** (2004), pp. 119–122.

[110] M. S. Dresselhaus and G. Dresselhaus. Intercalation compounds of graphite. *Adv. Phys.* **51** (2002), pp. 1–186.

[111] R. J. Lagow, R. B. Badachhape, J. L. Wood, and J. L. Margrave. Synthesis of superstoichiometric poly(carbon monofluoride). *J. Am. Chem. Soc.* **96** (1974), pp. 2628–2629.

[112] N. F. Yudanov. Synthesis, properties and structure of intercalated compounds of graphite fluoride C2F: Ph. D thesis. Nikolaev Institute of Inorganic Chemistry SB RAS, Novosibirsk (1995).

[113] A. V. Okotrub, I. P. Asanov, N. F. Yudanov, K. S Babin, A. V. Guselnikov, T. I. Nedoseikina, P. N. Gevko, L. G. Bulusheva, Z. Osvath, and L. P. Biro. Development of graphene layers by reduction of graphite fluoride C2F surface. *Phys. Stat. Sol. B* **246** (2009), pp. 2545–2548.

[114] H. Sahin, C. Ataca, and S. Ciraci. Magnetization of graphane by dehydrogenation. Appl. Phys. Lett. 95 (2009), p. 222510.

[115] J. Zhou, Q. Wang, Q. Sun, X. Chen, Y. Kawazoe, P. Jena, Ferromagnetism in semihydrogenated graphene sheet. *Nano Lett.* **9** (2009), pp. 3867–3870.

[116] O. V. Yazyev and L. Helm. Defect-induced magnetism in graphene. *Phys. Rev. B* **75** (2007), p. 125408.

[117] L. Z. Li, R. Qin, H. Li, L. L. Yu, Q. H. Liu, G. F. Luo, Z. X. Gao, and J. Lu. Functionalized Graphene for High-Performance Two-Dimensional Spintronics Devices *ACS Nano* **5** (2011), pp. 2601–2610.

[118] S. Tang and S. Zhang. Structural and electronic properties of hybrid fluorographene-graphene nanoribbons: insight from first-principles calculations. *J. Phys. Chem. C* **115** (2011), pp. 16644–16651.

[119] H. Sahin, M. Topsakal, and S. Ciraci. Structures of fluorinated graphene and their signatures. *Phys. Rev. B* **83** (2011), p. 115432.

[120] P. Thomas, D. Himmel, J. L. Mansot, M. Dubois, K. Guérin, W. Zhang, and A. Hamwi. Tribological Properties of Fluorinated Carbon Nanofibres. *Tribology Lett.* **34** (2009), pp. 49–59.

[121] S. Reich and C. Thomsen. Raman Spectroscopy of Graphite. *Philos. Trans. R. Soc. Lond. A* **362** (2004), pp. 2271–2288.

[122] F. Tuinstra and J. L. Koenig, Raman Spectrum of Graphite, *J. Chem. Phys.* **53** (1970), pp. 1126–1130.

[123] L. G. Cançado, K. Takai, T. Enoki, Y. A. Kim, H. Mizusaki, N. L. Speziali, A. Jorio, and M. A. Pimenta. Measuring the degree of stacking in graphite by Raman spectroscopy. *Carbon* **46** (2008), pp. 272-276.

[124] A. C. Ferrari, J. C. Meyer, V. Scardaci, et al. Raman spectrum of graphene and graphene layers. *Phys. Rev. Lett.* **97** (2006), p. 187401.

[125] H. Kuzmany, R. Pfeiffer, M. Hulman, and C. Kramberger. Raman spectroscopy of fullerenes and fullerene-nanotube composites. *Phil. Trans. A: Math. Phys. Eng. Sci.* **362** (2004), pp. 2375–2406.

[126] S. Costa, E. Borowiak-Palen, M. Kruszynska, A. Bachmatiuk, and R. J. Kalenczuk. Characterization of carbon nanotubes by Raman spectroscopy. *Mater. Sci.-Poland* **26** (2008), pp. 433–441.

[127] S. Costa, E. Borowiak-Palen, A. Bachmatiuk, M. H. Rummeli, T. Gemming, and R. J. Kalenczuk. Iron filled carbon nanostructures from different precursors. *Energy Conv. Man.* **49** (2008), pp. 2483–2486.

[128] C. Suryanarayana and M. G. Norton. X-ray Diffraction: A practical approach. Published by Springer-Verlag, New York, LLC (1998), p. 5.

[129] G. S. Rohrer. Structure and Bonding in Crystalline Materials. Published by Cambridge University Press (2001), pp. 205–206.

[130] M. A. Omar. Elementary Solid State Physics. Published by Addison Wesley (Revised printing) (1993), pp. 46–51.

[131] M. J. Buerger. X-ray crystallography : an introduction to the investigation of crystals by their diffraction of monochromatic X-radiation. Published by John Wiley & Sons, New York (1942), pp. 103.

[132] M. McElfresh. Fundamentals of Magnetism and Magnetic Measurements Featuring Quantum Design's Magnetic Property Measurement System. Quantum Design (1994).

[133] S. V. Komogortsev, R. S. Iskhakov, E. A. Denisova, A. D. Balaev, V. G. Myagkov, N. V. Bulina, A. G. Kudashov, and A. V. Okotrub. Magnetic anisotropy in the films of oriented carbon nanotubes filled with iron nanoparticles. *Tech. Phys. Lett.* **31** (2005), pp. 454–456.

[134] R. M. Bozorth. Ferromagnetism. Published by Wiley-IEEE Press, New York (1993).

[135] P. V. Hendriksen, S. Linderoth, and P. A. Lindgård. Finite-size modifications of the magnetic properties of clusters. *Phys. Rev. B* **48** (1993), pp. 7259–7273.

[136] S. V. Komogortsev, R. S. Iskhakov, A. D. Balaev, A. G. Kudashov, A. V. Okotrub, and S. I. Smirnov. Magnetic properties of Fe_3C ferromagnetic nanoparticles encapsulated in carbon nanotubes. *Phys. Sol. State* **49** (2007), pp. 734–738.

[137] J. M. North, R. M. Achey, and N. S. Dalal. Low-frequency Raman modes of the single-molecule magnets Mn_{12}-acetate and Fe_8Br_8 and their analogs. *Phys. Rev. B* **66** (2002), p. 174437.

[138] D. W. Mayo, F. A. Miller, and R. W. Hannah. Course notes on the interpretation of infrared and Raman spectra. Published by John Wiley and Sons, Hoboken (2004), 567 pages.

[139] S. K. Lee and D. Y. Baek. Visible vibronic emission spectrum of the jet-cooled pentafluorobenzyl radical. *Chem. Phys. Lett.* **311** (1999), pp. 36–40.

[140] M. Muntó, J. Gómez-Segura, J. Campo, M. Nakano, N. Ventosa, D. Ruiz-Molina, and J. Veciana. Controlled crystallization of Mn-12 single-molecule magnets by compressed CO_2 and its influence on the magnetization relaxation. *J. Mater. Chem.* **16** (2006), pp. 2612–2617.

[141] E. Burzurí, C. Carbonera, F. Luis, D. Ruiz-Molina, C. Lampropoulos, and G. Christou. Alignment of magnetic anisotropy axes in crystals of Mn_{12}-acetate and Mn_{12}-tBuAc molecular nanomagnets: Angle-dependent ac susceptibility study. *Phys. Rev. B* **80** (2009), p. 224428.

[142] A. J. Tasiopoulos, W. Wernsdorfer, K. A. Abboud, and G. Christou. $[Mn_{12}O_{12}(OMe)_2(O_2CPh)_{16}(H_2O)_2]^{2-}$ Single-Molecule Magnets and Other Manganese Compounds from a Reductive Aggregation Procedure. *Inorg. Chem.* **44** (2005), pp. 6324–6338.

[143] R. Basler, A. Sieber, G. Chaboussant, and H. U. Güdel. Inelastic neutron scattering study of electron reduction in Mn-12 derivatives. *Inorg. Chem.* **44** (2005), pp. 649–653.

[144] T. Kuroda-Sowa, M. Lam, A. L. Rheingold, C. Frommen, W. M. Reiff, M. Nakano, J. Yoo, A. L. Maniero, L.-C. Brunel, G. Christou, and D. N. Hendrickson. Effects of Paramagnetic Ferrocenium Cations on the Magnetic Properties of the Anionic Single-Molecule Magnet $[Mn_{12}O_{12}(O_2CC_6F_5)_{16}(H_2O)_4]^-$. *Inorg. Chem.* **40** (2001), pp. 6469–6480.

[145] N. E. Chakov, M. Soler, W. Wernsdorfer, K. A. Abboud, and G. Christou. Single-molecule magnets: Structural characterization, magnetic properties, and F-19 NMR spectroscopy of a Mn-12 family spanning three oxidation levels. *Inorg. Chem.* **44** (2005), pp. 5304–5321.

[146] C. Carbonera, F. Luis, J. Campo, J. Sanchez-Marcos, A. Camon, J. Chaboy, D. Ruiz-Molina, I. Imaz, J. van Slageren, S. Dengler, and M. Gonzalez. Effect of crystalline disorder on quantum tunneling in the single-molecule magnet Mn-12 benzoate. *Phys. Rev. B* **81** (2010), p. 014427.

[147] A. Lappas, K. Prassides, K. Vavekis, D. Arcon, R. Blinc, P. Cevc, A. Amato, R. Feyerherm, F. N. Gygax, and A. Schenck. Spontaneous magnetic ordering in the fullerene charge-transfer salt $(TDAE)C_{60}$. *Science* **267** (1995), pp. 1799–1802.

[148] K. Tanaka, Y. Asai, T. Sato, T. Kuga, T. Yamabe, and M. Tokumoto. Orientation dependent magnetic interaction in TDAE-C60, where TDAE is tetrakis(dimethylamino)ethylene. *Chem. Phys. Lett.* **259** (1996), pp. 574–578

[149] D. Mihailovic, D. Arcon, P. Venturini, R. Blinc, A. Omerzu, and P. Cevc. Orientational and Magnetic Ordering of Buckyballs in TDAE-C_{60}. *Science* **268** (1995), pp.400–402.

[150] A. S. Kotosonov. Diamagnetism of quasi-two-dimensional graphites. *JETP Lett.* **43** (1986), pp. 37–40.

[151] A. S. Kotosonov. Diamagnetism of carbon fibers. *Sov. Phys. Solid State* **33** (1991), pp. 1477–1480.

[152] D. V. Pinakov, V. A. Logvinenko, Y. V. Shubin, and G. N. Chekhova. The relationship between properties of fluorinated graphite intercalates and matrix composition - Part II. Intercalates with chloroform. *Therm. Anal. Calorim.* **90** (2007), pp. 339–405.

[153] D. V. Pinakov, V. A. Logvinenko, Y. V. Shubin, and G. N. Chekhova. The relationship between properties of fluorinated graphite intercalates and matrix composition. *Therm. Anal. Calorim.* **100** (2010), pp. 163–169.

Summary of the included papers

I. "Magnetic properties of carbon nanotubes with low content of Fe"

In Paper **I**, we explore the influence of iron filling rate on magnetic properties of carbon nanotubes at low concentrations of iron. It is shown that the magnetization process in weakly doped CNTs is different from what is observed for heavily doped CNTs. For low filling rate, we should take into account quantum effects.

My contribution: Raman spectroscopy and AFM measurements, participation in magnetic measurements and analysis of the data, writing part of the manuscript.

II. "Synthesis and magnetic properties of Mn_{12}-based single molecular magnets with benzene and pentafluorobenzene carboxylate ligands"

In Paper **II**, synthesis and magnetic properties of Mn_{12} magnetic clusters are considered from both theoretical and experimental points of view. The changes in ligand structure are shown to have a decisive effect on the magnetic properties of the compounds. The effect of ligand substitution was theoretically studied within the local density approximation taking into account on-site Coloumb repulsion. Calculation results confirm that the electronic structure and the magnetic exchange interactions between different Mn atoms strongly depend on the type of ligand.

My contribution: Raman spectroscopy measurements, participation in magnetic measurements and analysis of the data, writing part of the manuscript.

III. "Preparation and magnetic properties of Mn_{12} clusters with 4-cyanobenzenecarboxylate ligand, $[Mn_{12}O_{12}(O_2CC_6H_4\text{-}p\text{-}CN)_{16}(H_2O)_4]$ and its tetraphenylphosphonium salts"

Paper **III** is dedicated to a new Mn_{12} magnetic cluster with 4-cyanobenzene carboxylate ligand and its one-electron and two-electron reduced analogues (as salts). The synthesis, characterization and magnetic properties are described. The investigated cluster is found to have a record blocking temperature among single molecular magnets, while salts act as typical Mn_{12}-based single molecular magnets.

My contribution: Raman spectroscopy measurements, participation in magnetic measurements and analysis of the data, writing part of the manuscript.

IV. "Fullerene-induced magnetization training effect in single molecular magnet"

In Paper **IV**, we report the synthesis and characterization of the single molecular magnets $Mn_{12}O_{12}(RCOO)_{16}(H_2O)_4$, where $R = C_6H_5$; C_6F_5, and their 1:1 fullerene-diluted complexes, and compare their magnetic properties. It is demonstrated that their magnetic properties are strongly dependent on the magnetic core environment – the addition of fullerenes cause dramatic qualitative changes of the magnetization process which we call "magnetization training" effect.

My contribution: FT-IR spectroscopy measurements, participation in magnetic measurements and analysis of the data, writing part of the manuscript.

V. "The magnetic memory effect in fullerene-containing single molecular magnets"

In Paper **V**, we continue the studies of the fullerene-diluted Mn_{12}-based single molecular magnets. A strong asymmetry in the hysteresis loop along the vertical axis caused by unusually strong residual magnetization ("magnetic memory") is discovered. We suggest that this effect is determined by the magnetic ordering of fullerenes.

My contribution: Raman spectroscopy measurements, participation in magnetic measurements and analysis of the data, writing part of the manuscript.

VI. "Structural Evolution and Magnetic Properties of Underfluorinated C_2F"

In Paper **VI**, we conduct a systematic study of underfluorinated graphite intercalated compounds C_2F_x (x<1). Samples, prepared with introduction of different organic guest molecules that differ in size and symmetry, are characterized by means of x-ray diffraction and vibrational spectroscopy. We show that magnetic properties of intercalated C_2F_x compounds are strongly dependent on structure and stoichiometry.

My contribution: Participation in magnetic, XRD, FTIR and Raman spectroscopy measurements, and analysis of the data.

VII. "The influence of boron doping on magnetic properties of oxygen-eroded graphite"

In Paper **VII**, we study the influence of boron doping on defect-induced magnetism of nanoporous carbon. Introduction of boron modifies the electronic structure of the nanoporous carbon host, and thus, its structural and magnetic properties. We have

shown that boron affects the magnetic behaviour of nanoporous carbon in a complex way, changing both orbital diamagnetic and Curie-Weiss paramagnetic terms.

My contribution: Participation in magnetic and Raman spectroscopy measurements, analysis of the data, writing the manuscript.